Numerical Renormalization Group Calculations for Impurity Quantum Phase Transitions

Von der Mathematisch-Naturwissenschaftlichen Fakultät
der Universität Augsburg
zur Erlangung eines Doktorgrades der Naturwissenschaften
genehmigte Dissertation

von
Hyun Jung Lee
aus
Rep. of Korea

Erstgutachter: Priv. Doz. Dr. Ralf Bulla
Zweitgutachter: Prof. Dr. Thilo Kopp

Tag der mündlichen Prüfung: 12. Januar 2007

ACKNOWLEDGMENTS

I would like to express my gratitude to my supervisor Priv.-Doz. Dr. Ralf Bulla, who gave me the opportunity to learn many excellent physics in leading scientific circumstances. It was a great pleasure to study the fascinating subjects of quantum impurity systems and quantum phase transitions by the non-perturbative method of numerical renormalization group. Moreover, I deeply appreciate his attentive guidance in all matters of scientific life. I wish to thank for the opportunity to join his collaboration with Professor Dr. Matthias Vojta in Köln, to whom I am greatly indebted for the works that are presented in the thesis.

I would like to thank Professor Dr. Thilo Kopp for his willingness to co-report on the thesis.

To Professor Dr. Dieter Vollhardt and Professor Dr. Arno P. Kampf, I return my gratitude for their stimulating encouragement and warm hospitality.

I would like to give my sincere thanks to Dr. Sabine Tornow, Dr. Tae-Hyoung Gimm, and Professor Dr. Ning-Hua Tong for their invaluable help and collaboration.

I owe many thanks to the senior colleagues, Dr. Unjong Yu, Dr. Sanjeev Kumar, Dr. Marcus Kollar, Dr. Krzysztof Byczuk, and Dr. Jan Kunes, who were willing to give their scientific advice and many words of comfort.

To Martin Eckstein, Andreas Hackl, Robert Hager, Markus Schmid, Michael Sekania, Michael Sentef, Dr. Xinguo Ren, Dr. Ivan Leonov, Dr. Dmitry Lobaskin, and Dr. Georg Keller, I would like to thank for all kindness and cordialities that they showed.

I wish to thank Mrs. Barbara Besslich and Mrs. Anita Seidl, who gave help in organizational matters with great tenderness.

I owe particular thanks to Dr. Unjong Yu, Dr. Sanjeev Kumar, and Dr. Sabine Tornow for proofreading.

At last, I would like to thank God for his guidance.

CONTENTS

1. OVERVIEW

The thesis presents the results of the Numerical Renormalization Group (NRG) approach to three impurity models centered on the issues of impurity quantum phase transitions.

We start from introducing general concepts of quantum phase transitions and address the relevant physical questions of the impurity models (Chapter 2). Chapter 3 consists of the technical details of the NRG, where we discuss how the NRG tracks down possible fixed points that govern the universal behavior of the system at low temperature.

All the three impurity models studied show second order quantum phase transitions and quantum critical points but the levels of understanding of each case, particularly to the issues of quantum phase transitions, are quite different for historical reasons. The soft-gap Anderson model (Withoff and Fradkin 1990) is one of the most well-established cases in the contexts of impurity quantum phase transitions and various analytic and numerical methods examined the physical properties of the quantum critical phase as well as the stable phases on both sides of the transition point. Our contribution is made to the former case by analyzing the NRG many-particle spectrum of critical fixed points, with which we can see how the impurity contribution of the thermodynamic quantities have fractional degrees of freedom of charge and spin.

The quantum phase transition of the spin-boson model has a long history (Leggett, Chakravarty, Dorsey, Fisher, Garg and Zwerger 1987) but most of achievements were reached for the ohmic dissipation[1]. In the ohmic case, a delocalized and a localized phase are separated by a Kosterlitz-Thouless transition at the critical coupling $\alpha = 1$.[2] The new development of the NRG treating the bosonic degrees of freedom broadened the range of the parameter space to include the sub-ohmic case and, as a result, second order phase transitions were found for the bath exponent $0 < s < 1$ (Bulla, Tong and Vojta 2003) as we discuss in Chapter 5.

The bosonic single-impurity Anderson model (bsiAm) is a very new model and there is no precedent work on it. Nonetheless, the NRG approach to the bsiAm shows that the zero temperature phase diagrams are full of interesting physics such as the enhancement or the suppression of the Bose-Einstein condensation by the impurity and the existence of quantum critical points. The works presented

[1] The $s = 1$ case where s is the exponent of the bath spectral function.
[2] for the unbiased case of $\epsilon = 0$.

in Chapter 6 indicate the possibility that the quantum phase transition of the Bose-Hubbard model originates from the physics at the local sites so that the self-consistent treatments of the local and the global properties, for example, dynamical mean field theory, allow to solve the problem.

Appendice A and D show the details of the calculations that are abridged in the main sections. Appendix B describes the thermodynamics in the ohmic spin-boson model calculated with the NRG method, which proves the success of the NRG approach to the spin-boson model by showing a good agreement to the precedent result (Costi 1998). Appendix C is about the BEC of an ideal bosonic gas with a fixed (zero) chemical potential, which is frequently mentioned in the Chapter 6 of the bosonic single-impurity Anderson model.

2. INTRODUCTION TO QUANTUM PHASE TRANSITIONS

This chapter aims to cover the basic ideas of quantum phase transitions that are frequently used in the main body of the thesis (Chapter 4, 5, and 6).

We start to giving the definitions of the scaling limit and universality from the viewpoint of classical phase transitions with an example of the one dimensional Ising model and introduce universal functions that represent the physics in the vicinity of the critical points as a function of two large (macroscopic) lengths, L_τ (system size) and ξ (correlation length).[1]

We bring those concepts defined in the classical cases into quantum systems to develop a universal critical theory for quantum phase transitions. Again the physical properties near to the critical points are characterized by the universal scaling function, of which the argument is the dimensionless ratio of two small energy scales, T (temperature) and Δ (an energy gap between the ground state and the first excitation), instead of the classical counterparts L_τ and ξ. We take the two-point correlation,

$$C(x,t) \equiv \langle \hat{\sigma}^z(x,t)\hat{\sigma}^z(0,0)\rangle, \tag{2.1}$$

as an example to discuss the shape of the universal scaling function in the critical phase (Section 1.2).

Finally, we enter the subject of the thesis, impurity quantum phase transitions, in Section 1.3, where we mention the specific issues of impurity models, such as the impurity contribution of the physical observables and the local response functions at the impurity site. The universal critical theory for the impurity model is distinguished from the one for the lattice system in a few respects. For examples, the feature of spatial correlations, one of the important issues of the criticality of lattice systems, is absent (or disregarded) in impurity systems and the quantum critical behavior reveals not in the response to a uniform global field H but rather in that to a local field h coupled solely to the impurity. All the arguments concerning the response to the magnetic field are given for a situation where the impurity has a single SU(2) spin $\hat{\mathbf{S}}$ of size S and the conduction band is considered as a spinful bath.

[1] To be precise, L_τ and ξ are not treated independently but form a single argument as the dimensionless ratio L_τ/ξ.

2.1 The scaling limit and universality

The scaling limit of an observable is defined as its value when all corrections involving the ratio of microscopic lengths, such as the lattice spacing a, to large macroscopic ones of the correlation length ξ, the observation scale τ, and the system size

$$L_\tau \equiv Ma, \tag{2.2}$$

are neglected. To take a concrete form of the scaling limit, we discuss the manner in which the parameter K of the Ising chain H_I

$$H_I = -K \sum_{i=1}^{M} \sigma_i^z \sigma_{i+1}^z. \tag{2.3}$$

must be treated. The partition function and the two-point spin correlation are exactly evaluated from the original solution of Ising (Ising 1925) as discussed in (Sachdev 1999) and here we skip over the detail steps just to write down the results. The partition function calculated within the periodic boundary condition is given as

$$Z = \sum_{\{\sigma_i^z\}} \prod_{i=1}^{M} \exp(K \sigma_i^z \sigma_{i+1}^z) = \epsilon_1^M + \epsilon_2^M, \tag{2.4}$$

with $\epsilon_1 = 2\cosh K$ and $\epsilon_2 = 2\sinh K$. The two-point spin correlation has the exact form of

$$\begin{aligned} \langle \sigma_i^z \sigma_j^z \rangle &= \frac{1}{Z} \sum_{\{\sigma_i^z\}} \exp(-H_I) \sigma_i^z \sigma_j^z \\ &= \frac{\epsilon_1^{M-j+i} \epsilon_2^{j-i} + \epsilon_2^{M-j+i} \epsilon_1^{j-i}}{\epsilon_1^M + \epsilon_2^M}. \end{aligned} \tag{2.5}$$

Introducing the concept of correlation length, ξ, from the Eq. (2.5) in the limit of an infinite chain ($M \to \infty$) allows a simple form to the two-point spin correlation:

$$\langle \sigma_i^z \sigma_j^z \rangle = (\tanh K)^{j-i}. \tag{2.6}$$

It is useful for the following discussion to label the spins not by the site index i, but by a physical length coordinate τ. So if we imagine that the spins are placed on a lattice of spacing a, the $\sigma^z(\tau) \equiv \sigma_j^z$ where

$$\tau = ja. \tag{2.7}$$

With this notation, we can write Eq. (2.6) as

$$\langle \sigma^z(\tau) \sigma^z(0) \rangle = e^{-|\tau|/\xi}, \tag{2.8}$$

where the correlation length, ξ, is given by

$$\frac{1}{\xi} = \frac{1}{a} \ln \coth K. \tag{2.9}$$

The notion of the correlation length ξ given above helps us write a universal critical theory of the Ising chain H_I in the scaling limit, where the detail informations of the finite-size system (M, K and a) are absorbed into the macroscopic lengths ξ and L_τ with replacements of $M = L_\tau/a$ and $K = \ln \coth^{-1}(a/\xi)$ and, finally, take the limit $a \to 0$ at fixed τ, L_τ and ξ.

We first describe the results for the free energy. The quantity with the finite scaling limit should clearly be the free energy density, $\mathcal{F}$:

$$\begin{aligned} \mathcal{F} &= -\ln \mathcal{Z}/Ma \\ &= E_0 - \frac{1}{L_\tau} \ln \left[2 \cosh \frac{L_\tau}{2\xi} \right], \end{aligned} \tag{2.10}$$

where $E_0 = -K/a$ is the ground state energy per unit length of the chain.
In a similar manner, we can take the scaling limit of the correlation function in Eq. (2.5). We obtain

$$\langle \sigma^z(\tau)\sigma^z(0) \rangle = \frac{e^{-|\tau|/\xi} + e^{-(L_\tau - |\tau|)/\xi}}{1 + e^{-L_\tau/\xi}}. \tag{2.11}$$

The assertion of *universality* is that the results of the scaling limit are not sensitive to the microscopic details. This can be seen as the formal consequence of the physically reasonable requirement that correlations at the scale of large ξ should not depend upon the details of the interactions on the scale of the lattice spacing,a.
We can make the assertion more precise by introducing the concept of a *universal scaling function*. We write Eq. (2.10) in the form

$$\mathcal{F} = E_0 + \frac{1}{L_\tau} \Phi_{\mathcal{F}}(\frac{L_\tau}{\xi}), \tag{2.12}$$

where Φ_F is the universal scaling function, whose explicit value can be easily deduced by comparing with Eq. (2.10). Notice that the argument of $\Phi_{\mathcal{F}}$ is simply the dimensionless ratios that can be made out of the large(macroscopic) lengths at our disposal: L_τ and ξ. The prefactor, $1/L_\tau$, in front of $\Phi_{\mathcal{F}}$ is necessary because the free energy density has dimensions of inverse length.
In a similar manner, we can introduce a universal scaling function of the two-point correlation function. We have

$$\langle \sigma^z(\tau)\sigma^z(0) \rangle = \Phi_\sigma(\frac{\tau}{L_\tau}, \frac{L_\tau}{\xi}), \tag{2.13}$$

where Φ_σ is again a function of all the independent dimensionless combinations of large lengths and the exact form of Φ_σ is obtained by comparison with Eq. (2.11).

2.2 Quantum phase transitions and quantum critical points

Quantum phase transitions can be identified with any point of non-analyticity in the ground state energy and the types of non-analyticity divide quantum phase transitions into the first and the second order. As in the classical cases, only second order transitions show critical behaviors near to the transition points and our focus shall be on the case.

A point of non-analyticity in the ground state energy and the distance from the point in the parameter space is quantified by an energy gap Δ between the ground state and the lowest excitation vanishing at the critical point. Consider a Hamiltonian $H(g)$ that varies as a function of a dimensionless coupling g.

$$H(g) = H_0 + gH_1 \tag{2.14}$$

where H_0 and H_1 are not commutable in general. In most cases, we find that, as g approaches the critical value g_c, $\Delta(g)$ vanishes as

$$\Delta(g) \propto |g - g_c|^{z\nu}, \tag{2.15}$$

with a critical exponent $z\nu$. The value of the critical exponent $z\nu$ is universal, that is, it is independent of most of the microscopic details of $H(g)$. In the vicinity of the quantum critical point ($g \approx g_c$), the physical properties such as a free energy density $\mathcal{F} = -T \ln \mathcal{Z}$ and the dynamic two-point correlations of the order parameter $\hat{\sigma}^z$,

$$C(x,t) \equiv \langle \hat{\sigma}^z(x,t)\hat{\sigma}^z(0,0)\rangle \tag{2.16}$$

are characterized by the universal scaling function of the dimensionless ratio of the small energy scales Δ and T.[2]

As an example, we discuss the second order quantum phase transition of the Ising chain in a transverse field,

$$H_I(g) = -J\sum_i (g\hat{\sigma}_i^x + \hat{\sigma}_i^z\hat{\sigma}_i^z). \tag{2.18}$$

following the calculations in (Sachdev 1999). The exact single-particle spectrum is given as

$$\varepsilon_k(g) = 2J(1 + g^2 - 2g\cos k)^{1/2}, \tag{2.19}$$

[2] This is the analog of the large length scales of the classical problem, while the universal behavior at large length scales (ξ and L_τ) in the classical system maps onto the physics at small energy scales (Δ and T) in the quantum system.

$$\Delta = \frac{1}{\xi},\ T = \frac{1}{L_\tau}. \tag{2.17}$$

with which the Hamiltonian in Eq. (2.18) is written in a diagonal form of

$$H_I(g) = \sum_k \varepsilon_k(g)(\gamma_k^\dagger \gamma_k - 1/2). \tag{2.20}$$

The diagonal form in Eq. (2.20) is obtained using the two consequent transformations of the Jordan-Wigner transformation[3] and the Bogolioubov transformation.[4]

The ground state, $|0\rangle$, of $H_I(g)$ has no γ fermions and therefore satisfies $\gamma_k|0\rangle = 0$ for all k. The excited states are created by occupying the single-particle states; they can clearly be classified by the total number of occupied states and a n-particle state has the form $\gamma_{k_1}^\dagger \gamma_{k_2}^\dagger ... \gamma_{k_n}^\dagger |0\rangle$, with all the k_i distinct. The energy gap between the ground state and the first excited one occurs at $k = 0$ and equals

$$\Delta(g) = 2J(1-g). \tag{2.21}$$

Therefore the model $H_I(g)$ exhibits a quantum phase transition at the critical coupling $g = 1$, which separates an ordered state with Z_2 symmetry broken ($g \ll 1$) from a quantum paramagnetic state where the symmetry remains unbroken ($g \gg 1$). The state at $g = 1$ is critical and there is a universal continuum quantum field theory that describes the critical properties in its vicinity.
We shall now obtain the critical theory for the model in Eq. (2.18). We define the continuum Fermi field

$$\Psi(x) = \frac{1}{\sqrt{a}} c_i, \tag{2.22}$$

that satisfies

$$\{\Psi(x), \Psi^\dagger(x')\} = \delta(x - x'). \tag{2.23}$$

To express $H_I(g)$ in terms of Ψ and the expansions in spatial gradients yields the continuum H_F,

$$H_F = E_0 + \int dx \left[\frac{c}{2} (\Psi^\dagger \frac{\partial \Psi^\dagger}{\partial x} - \Psi \frac{\partial \Psi}{\partial x}) + \Delta \Psi^\dagger \Psi \right] + ..., \tag{2.24}$$

where the ellipses represent terms with higher gradients, and E_0 is an uninteresting additive constant. The coupling constant in H_F are

$$\Delta = 2J(1-g), \quad c = 2Ja. \tag{2.25}$$

Notice that at the critical point $g = 1$, we have $\Delta = 0$, and we have $\Delta > 0$ in the magnetically ordered phase and $\Delta < 0$ in the quantum paramagnet.

[3] To map the Hamiltonian $H_I(g)$ with spin-1/2 degrees of freedom into a quadratic ones with the spinless Fermi operators

[4] To transform the quadratic Hamiltonian into a form whose number is conserved.

The subsequent scaling analysis of the continuum Hamiltonian H_F is performed in a Lagrangean path integral representation of the dynamics of H_F:

$$\mathcal{Z} = \int \mathcal{D}\Psi\mathcal{D}\Psi^\dagger \exp(-\int_0^{1/T} d\tau dx \mathcal{L}_I) \tag{2.26}$$

with the Lagrangean density $\mathcal{L}_I$,

$$\mathcal{L}_I = \Psi^\dagger \frac{\partial \Psi}{\partial \tau} + \frac{c}{2}(\Psi^\dagger \frac{\partial \Psi^\dagger}{\partial x} - \Psi \frac{\partial \Psi}{\partial x}) + \Delta \Psi^\dagger \Psi. \tag{2.27}$$

The fact that the action $\mathcal{L}_I$, as a universal critical theory of the model H_I, has to remain invariant under scaling transformations, where all modes of the field Ψ with momenta between Λ and Λe^{-l} are integrated out to yield an overall additive constant to the free energy $\mathcal{F} = -T \ln \mathcal{Z}$, determines the rescaling behaviors of the elements in the Lagrangean density $\mathcal{L}_I$:

$$\begin{aligned} x' &= x e^{-l}, \\ \tau' &= \tau e^{-zl}, \\ \Psi' &= \Psi e^{l/2}, \\ \Delta' &= \Delta e^{l}. \end{aligned} \tag{2.28}$$

Accordingly, the scaling dimension of each element is given as[5]

$$\begin{aligned} dim[x] &= -1, \\ dim[\tau] &= -z, \\ dim[\Psi] &= 1/2, \\ dim[\Delta] &= 1. \end{aligned} \tag{2.29}$$

The temperature T, is just an inverse time, therefore has a dimension,

$$dim[T] = z = 1, \tag{2.30}$$

for the given model H_I. The parameter z is the *dynamical critical exponent* and determines the relative rescaling factors of space and time. The present model H_I has $z = 1$ as it is related to classical problem that is fully isotropic in D spatial dimensions.

The scaling dimension of the order parameter $\hat{\sigma}^z$ is quite difficult to determine since it is not a simple local function of the Fermi field Ψ and here we present the result only.

$$dim[\hat{\sigma}^z] = 1/8. \tag{2.31}$$

Armed with the knowledge of the scaling dimensions, we can put important general constraints on the structure of universal scaling forms for various observables.

[5] $\Delta' = \Delta(e^l)^{dim[\Delta]}$

As an example of such considerations, let us consider the scaling form satisfied by the two-point correlation $C(x,t)$ defined in Eq. (2.16):

$$C(x,t) \;\; = \;\; ZT^{1/4}\Phi_I(\frac{Tx}{c}, Tt, \frac{\Delta}{T}). \tag{2.32}$$

A prefactor, consisting of an overall non-critical normalization constant Z and $T^{1/4}$, shows consistency of the scaling dimension of the $C(x,t)$.[6] A dimensionless universal scaling function Φ_I has three arguments; time and spatial coordinates x and t and the energy gap Δ are combined with a power of T to make the net scaling dimensions 0[7]. The properties of the two points correlation depends completely on the ratio of two energy scale, that of the $T = 0$ energy gap to temperature: Δ/T. There are two low-T regimes with $T \ll |\Delta|$; the magnetically ordered side for $\Delta > 0$ and the quantum paramagnetic ground state for $\Delta < 0$. Then there is a novel continuum high-T regime, $T \gg |\Delta|$, where the physics is controlled primarily by the quantum critical point $\Delta = 0$ and its thermal excitations and is described by the associated continuum quantum field theory. Here we focus on the last regime and show the structure of the scaling function in it.

At the quantum critical point ($T = 0$, $\Delta = 0$, $g = g_c$), we can deduce the form of the correlation by a simple scaling analysis. As the ground state is scale invariant at this point, the only scale that can appear in the equal-time correlation is the spatial separation x; from the scaling dimension $\hat{\sigma}^z$ in Eq. (2.31), we then know that the correlation must have the form

$$C(x,0) \sim \frac{1}{(|x|/c)^{1/4}} \tag{2.33}$$

at $T = 0$, $\Delta = 0$. We can also include time-dependent correlations at this level without much additional work. We know the continuum theory (2.27) is Lorentz invariant, and so we can easily extend (2.33) to the imaginary time result

$$C(x,\tau) \sim \frac{1}{(\tau^2 + x^2/c^2)^{1/8}} \tag{2.34}$$

at $T = 0$, $\Delta = 0$. This result can also be understood by the mapping to the classical $D = 2$ Ising model, where correlations are isotropic with all D dimensions, and so the long-distance correlations depend only upon the Euclidean distance between two points.

We extend the result (2.34) to $T > 0$ by the transformation

$$c\tau \pm ix \to \frac{c}{\pi T}\sin\left(\frac{\pi T}{c}(c\tau \pm ix)\right), \tag{2.35}$$

[6] $dim\,[C(x,t)] = dim\,[\langle\sigma_z(x,t)\sigma_z(0,0)\rangle] = 1/4$ with $dim\,[T] = z = 1$ for the given model H_I.
[7] the velocity c is invariant under the scaling transformation, i.e. dim[c]=0.

which makes a very general connection between *all* $T = 0$ and $T > 0$ two-point correlation of the continuum theory $\mathcal{L}_I$ (Cardy 1984). Applying the mapping in Eq. (2.35) to the Eq. (2.34) allow us to obtain the correlation at $T > 0$:

$$C(x,\tau) \sim T^{1/4} \frac{1}{[\sin(\pi T(\tau - ix/c))\sin(\pi T(\tau + ix/c))]^{1/8}} \tag{2.36}$$

at $T = 0$.

As expected, this result is of the scaling form in Eq. (2.32) of which the last argument is zero. It is the leading result everywhere in the continuum high-T (i.e. quantum critical) region. Notice that this result has been obtained in imaginary time. Normally, such results are not always useful in understanding the long real-time dynamics at $T > 0$ because the analytic continuation is ill-posed.

2.3 Impurity quantum phase transitions

We give an overview of the quantum phase transitions in impurity models (Bulla and Vojta 2003, Vojta 2006, Affleck 2005), of which the detailed contexts cover the rest of the thesis.

All our impurity models have the general form,

$$\mathcal{H} = \mathcal{H}_b + \mathcal{H}_{imp}, \tag{2.37}$$

where $\mathcal{H}_b$ contains the bulk degrees of freedom[8] and $\mathcal{H}_{imp}$ contains the impurity degrees of freedom, e.g., one or more quantum spins, together with their coupling to the bath, which typically is local in space.

The physical properties relevant to the impurity quantum phase transition are classified to two categories; one is the impurity contribution to the total system and the other is the local quantity at the impurity site.

In the former case, a physical observable $\mathcal{A}$ is defined to be the change in the total measured value of $\mathcal{A}$ brought about by adding a single impurity to the system. Each such contribution can be computed from an expression of the form

$$\begin{aligned} \langle \mathcal{A} \rangle_{imp} &= \langle \mathcal{A} \rangle - \langle \mathcal{A} \rangle_0 \\ &= \mathrm{Tr}(\mathcal{A} e^{-\beta \mathcal{H}}) - \mathrm{Tr}_0(\mathcal{A} e^{-\beta \mathcal{H}_b}) \end{aligned} \tag{2.38}$$

where Tr_0 means a trace taken over an impurity-free system.

For example, the impurity contributions to the entropy and the specific heat are obtained as (Krishna-murthy, Wilkins and Wilson 1980)

$$\begin{aligned} S_{imp} &= -\frac{\partial \mathcal{F}_{imp}}{\partial T}, \\ C_{imp} &= -T \frac{\partial^2 \mathcal{F}_{imp}}{\partial T^2}. \end{aligned} \tag{2.39}$$

[8] The bulk systems generically are interacting but, under certain circumstances the self-interaction is irrelevant and can be discarded from the outset.

Here, $\mathcal{F}_{imp}$ is the difference between the total Helmholtz free energy of the system with and without the impurity:

$$\mathcal{F}_{imp} = -T \ln \mathcal{Z}_{imp} = T \ln \frac{\mathcal{Z}_0}{\mathcal{Z}}, \tag{2.40}$$

with

$$\mathcal{Z} = \mathrm{Tr} e^{-\beta \mathcal{H}}, \quad \mathcal{Z}_0 = \mathrm{Tr} e^{-\beta \mathcal{H}_b}. \tag{2.41}$$

In general, zero-temperature impurity critical points can show a non-trivial residual entropy [contrary to bulk quantum critical points where the entropy usually vanishes with a power law $S(T) \propto T^y$]. The stable phases usually have the impurity entropy of the form $S_{imp}(T \to 0) = \ln g$ where g is the integer ground state degeneracy, e.g., $g = 1$ for a Kondo-screened impurity and $g = 2S + 1$ for an unscreened spin of size S. At a second-order transition, g can take fractional values (Andrei and Destri 1984, Bolech and Andrei 2002, Gonzalez-Buxton and Ingersent 1998).

Another quantity of interest is the impurity contribution to the zero-field magnetic susceptibility, given by

$$\chi_{imp} = -\left(\frac{\partial^2 \mathcal{F}_{imp}}{\partial H^2} \right)_{H=h=0} \tag{2.42}$$

where the uniform and local magnetic field, H and h, enter the Hamiltonian $\mathcal{H}$ in Eq. (2.37) through an additional term (Ingersent and Si 2002) [9],

$$\mathcal{H}_{mag} = \sum_{\sigma} \left[(H + h) S^z + \frac{H}{2} \sum_k c^\dagger_{k\sigma} \tau^z_{\sigma\sigma} c_{k\sigma} \right]. \tag{2.43}$$

For an unscreened impurity spin of size, S, we expect $\chi_{imp}(T \to 0) = S(S + 1)/(3T)$ in the low-temperature limit - note that this unscreened moment will be spatially speared out due to the residual coupling to the bath. A fully screened moment will be characterized by $T\chi_{imp} = 0$ (Gonzalez-Buxton and Ingersent 1998, Vojta 2006). In the presence of global SU(2) symmetry, the susceptibility χ_{imp} does not acquire an anomalous dimension at criticality, in contrast to χ_{loc} below, because it is a response function associated to the conserved quantity S_{tot} (Sachdev 1997). Thus we expect a Curie law

$$\lim_{T \to 0} \chi_{imp}(T) = \frac{\mathcal{C}_{imp}}{T}, \tag{2.44}$$

where the prefactor $\mathcal{C}_{imp}$ is in general a non-trivial universal constant different from the free-impurity value $S(S+1)/3$. Apparently, Eq. (2.44) can be interpreted

[9] S^z and $c^\dagger_{k\sigma} \tau^z_{\sigma\sigma} c_{k\sigma}$ represent the spin of the impurity and the conduction electrons, respectively.

as the Curie response of a fractional effective spin (Sachdev, Buragohain and Vojta 1999) - examples are e.g. found in the pseudo-gap Kondo model and in the Bose Kondo model (Vojta 2006).

An important example of the local quantities, i.e., the static local susceptibility χ_{loc}, naturally comes up from the field-dependent Hamiltonian $\mathcal{H}_{mag}$ (Ingersent and Si 2002).

$$\chi_{loc} = -\left(\frac{\partial^2 \mathcal{F}_{imp}}{\partial h^2}\right)_{H=h=0}. \tag{2.45}$$

In an unscreened phase we have $\chi_{loc} \propto 1/T$ as $T \to 0$. This Curie law defines a residual local moment m_{loc} at $T = 0$, which is the fraction of the total, free fluctuating, moment of size S, which is remained localized at the impurity site:

$$\lim_{T\to} \chi_{loc}(T) = \frac{m_{loc}^2}{T}. \tag{2.46}$$

A decoupled impurity has $m_{loc}^2 = \mathcal{C}_{imp} = S(S+1)/3$, but a finite coupling to the bath implies $m_{loc}^2 < \mathcal{C}_{imp}$. The quantity m_{loc} turns out to be a suitable order parameter (Ingersent and Si 2002) for the phase transitions between an unscreened and screened spin: at a second-order transition it vanishes continuously as $t \to 0^-$. Here, $t = (r - r_c)/r_c$ is the dimensionless measure of the distance to the criticality in terms of coupling constants, with $t > 0$ ($t < 0$) placing the system into the (un)screened phase. Thus, $T\chi_{loc}$ is not pinned to the value of $S(S+1)/3$ for $t < 0$ (in contrast to $T\chi_{imp}$).

An important observation from the above analysis on the impurity and local susceptibility is that the quantum critical behavior reveals itself, not in the response to a uniform magnetic field H, but rather in that to a local magnetic field h coupled solely to the impurity.

Given that the local field h act as a scaling variable, a scaling ansatz for the impurity part of the free energy takes the form,

$$\mathcal{F}_{imp} = T\Phi_{\mathcal{F}}(gT^{-1/\nu}, hT^{-b}), \tag{2.47}$$

where the coupling coefficients g measures the distance to criticality at $g = g_c$ and h is the local field. ν is the correlation length exponent which describes the vanishing energy scale Δ[10]:

$$\Delta \propto |g - g_c|^{\nu}.^{11} \tag{2.48}$$

With the local magnetization $M_{loc} = \langle \hat{S}_z \rangle = -\partial \mathcal{F}_{imp}/\partial h$ and the corresponding susceptibility $\chi_{loc} = -\partial^2 \mathcal{F}_{imp}/(\partial h)^2$ we can define critical exponents as

[10] The energy gap between the ground state and the first excitation

[11] Note that there is no independent dynnamical exponent z for the present impurity models, formally z=1. See Eq. (2.15).

usual (Ingersent and Si 2002, Vojta 2006):

$$\begin{aligned} M_{loc}(g < g_c, T = 0, h \to 0) &\propto (g_c - g)^{\beta}, \\ \chi_{loc}(g > g_c, T = 0) &\propto (g - g_c)^{\gamma}, \\ M_{loc}(g = g_c, T = 0) &\propto |h|^{1/\delta}, \\ \chi_{loc}(g = g_c, T) &\propto T^{-x}, \\ \chi''_{loc}(g = g_c, T = 0, \omega) &\propto |\omega|^{-y}\mathrm{sgn}(\omega). \end{aligned} \tag{2.49}$$

The last equation describes the dynamical scaling of the local susceptibility.

In the absence of a dangerously irrelevant variable, there are only two independent exponents. The scaling form in Eq. (2.47) allows to derive hyper-scaling relations:

$$\beta = \gamma\frac{1-x}{2x},\ 2\beta + \gamma = \nu,\ \delta = \frac{1+x}{1-x}. \tag{2.50}$$

Furthermore, hyper-scaling also implies $x = y$. This is equivalent to so-called ω/T scaling in the dynamical behavior-for instance, the local dynamic susceptibility will obey the full scaling form (Sachdev 1999),

$$\chi''_{loc}(\omega, T) = \frac{\mathcal{B}_1}{\omega^{1-\eta_\chi}}\Phi_1\left(\frac{\omega}{T}, \frac{T^{1/\nu}}{g - g_c}\right), \tag{2.51}$$

which describes critical local-moment fluctuations, and the local static susceptibility follows

$$\chi''_{loc}(T) = \frac{\mathcal{B}_2}{\omega^{1-\eta_\chi}}\Phi_2\left(\frac{T^{1/\nu}}{g - g_c}\right). \tag{2.52}$$

Here, $\eta_\chi = 1 - x$ is a universal anomalous exponent, and $\Phi_{1,2}$ are universal crossover functions (for the specific critical fixed point), whereas $\mathcal{B}_{1,2}$ are non-universal prefactors.

3. NUMERICAL RENORMALIZATION GROUP APPROACH

3.1 Kondo problem and invention of NRG

Wilson originally developed the numerical renormalization group method (NRG) for the solution of the Kondo problem (Wilson 1975). The history of this problem (Hewson 1993) goes back to the 1930's when a resistance minimum was found at very low temperatures in seemingly pure metals (de Haas, de Bör and van den Berg 1934). This minimum, and the strong increase of the resistance $\rho(T)$ upon further lowering of the temperature, has been later found to be caused by magnetic impurities (such as iron). Kondo successfully explained the resistance minimum within a perturbative calculation for the *s-d* (or Kondo) model (Kondo 1964), a model for magnetic impurities in metals. However, Kondo's result implies a divergence of $\rho(T)$ for $T \to 0$, in contrast to the saturation found experimentally. The numerical renormalization group method, where the concept of poor man's scaling (Anderson 1970) is adopted into the numerical diagonalization procedure, succeeded to obtain many-particles spectra with extremely high energy-resolution and to explain the finite value of resistance $\rho(T)$ for $T \to 0$. The detailed strategy is discussed in the following section.

3.2 Summary of the Basic Techniques

The fact that a proper description of $T \to 0$ limit is achieved only after thermodynamic limit ($N \to \infty$) is taken into account makes it difficult for the usual numerical approaches on impurity models to pursue the $T \to 0$ limit. For example, substituting a continuous band with a finite set of discrete states yields a finite size of mesh $\delta\varepsilon$ in energy-space, with which one can describe thermodynamics of the continuous system only for the temperature T larger than $\delta\varepsilon$. In this sense, a given temperature T makes a criterion for discretization,

$$\delta\varepsilon \ll T. \tag{3.1}$$

Assuming that an impurity couples to an electronic bath with a band-width D, the number of degrees of freedom of the discretized system (N) is roughly estimated as

$$N \propto \frac{D}{\delta\varepsilon} \gg \frac{D}{T}. \tag{3.2}$$

Brute-force technique holds good until $T \sim 10^{-3}D(N \sim 10^3)$ and discarding some of electronic states, so called *truncation*, is indispensable to proceed calculations into a lower temperature.

Let us assume that we reduce the system-size from $N \times N$ to $N/2 \times N/2$ by discarding the high-energy states, which are not stirred by thermal-fluctuations in given temperature T. We can invest the surplus degrees of freedom into the low-lying spectrums and improve the energy-resolution in the small energy-scale. With the additional elements, the new Hamiltonian produces N of many-particle states which are more concentrated on the low energy-scale compared to the previous case. The critical point is how to include extra degree of freedoms for low energy-scale in the existing spectrum. In general, adding new conduction electrons can break the symmetry of the previous system so that all the eigenstates are mixed up to construct a new set of eigenstates. Now, severe errors can occur if we lose some of the eigenstates of the previous system with truncation. To get around the trouble, Wilson introduced two sophisticated steps into the numerical renormalization group method:

- logarithmic discretization
- iterative diagonalization of a semi-infinite chain

The first one is to discretize the energy-space with a logarithmic mesh and select a discrete set of electronic degrees of freedom for numerical diagonalization. The reason why the mesh is logarithmic is discussed in Section 3.2.1. The second step is to add new degrees of freedom without touching the electronic configurations at the impurity-site. In these schemes, we can proceed the iterations avoiding artificial effects due to truncation and obtain the many-particles spectra with an arbitrary fine mesh $\delta\varepsilon$, which makes it possible to simulate the thermodynamics of a continuous system for an arbitrary low temperature T with a discretized band.

3.2.1 Logarithmic discretization

The Hamiltonian of the conventional single-impurity Anderson model (Wilson 1975, Hewson 1993) is given by

$$\begin{aligned} H &= \varepsilon_f \sum_\sigma f^\dagger_{-1\sigma} f_{-1\sigma} + U f^\dagger_{-1\uparrow} f_{-1\uparrow} f^\dagger_{-1\downarrow} f_{-1\downarrow} \\ &\quad + \sum_{k\sigma} \varepsilon_k c^\dagger_{k\sigma} c_{k\sigma} + \sum_{k\sigma} V(\varepsilon_k)\big(f^\dagger_{-1\sigma} c_{k\sigma} + c^\dagger_{k\sigma} f_{-1\sigma}\big) \end{aligned} \tag{3.3}$$

where the $c^{(\dagger)}_{k\sigma}$ denote standard annihilation (creation) operators for band states with spin σ and energy ε_k, the $f^{(\dagger)}_{-1,\sigma}$ those for impurity states with spin σ and energy ε_f. The Coulomb interaction for two electrons at the impurity site is given

by U and the two subsystems are coupled via an energy-dependent hybridization $V(\varepsilon_k)$.

The Hamiltonian in Eq. (3.3) can be written into a form which is more convenient for the derivation of the NRG equations:

$$\begin{aligned} H &= \varepsilon_f \sum_\sigma f^\dagger_{-1\sigma} f_{-1\sigma} + U f^\dagger_{-1\uparrow} f_{-1\uparrow} f^\dagger_{-1\downarrow} f_{-1\downarrow} \\ &\quad + \sum_\sigma \int_{-1}^{1} d\varepsilon\ g(\varepsilon) a^\dagger_{\varepsilon\sigma} a_{\varepsilon\sigma} + \sum_\sigma \int_{-1}^{1} d\varepsilon\ h(\varepsilon)\big(f^\dagger_{-1\sigma} a_{\varepsilon\sigma} + a^\dagger_{\varepsilon\sigma} f_{-1\sigma}\big), \end{aligned} \tag{3.4}$$

where we introduced a one-dimensional energy representation for the conduction band with band cut-offs at ± 1, dispersion $g(\varepsilon)$ and hybridization $h(\varepsilon)$. The band operators fulfill the standard fermionic commutation rules $\left[a^\dagger_{\varepsilon\sigma}, a_{\varepsilon'\sigma'}\right] = \delta(\varepsilon - \varepsilon')\delta_{\sigma\sigma'}$.

The Hamiltonian in Eq. (3.3) is equivalent to the Hamiltonian in Eq. (3.4) when we select $g(\varepsilon)$ and $h(\varepsilon)$ to satisfy the following condition:

$$\frac{\partial \varepsilon(x)}{\partial x} h(\varepsilon(x))^2 = V(\varepsilon(x))^2 \rho(\varepsilon(x)) = \frac{1}{\pi}\Delta(x), \tag{3.5}$$

where $\varepsilon(x)$ is the inverse of $g(\varepsilon)$, i.e.

$$\varepsilon(g(x)) = x, \tag{3.6}$$

and $\rho(\varepsilon)$ is the density of states for the free conduction electrons (Bulla, Pruschke and Hewson 1997).

As a first step of discretization, we divide a conduction band into N-intervals $\{I_n\}$,

$$\int_{-1}^{1} d\varepsilon \to \sum_n \int_{I_n} d\varepsilon, \tag{3.7}$$

with $I_n = [\varepsilon_n, \varepsilon_{n+1}]$, $(n = 0, 1, ..., N-1,\ \varepsilon_0 = -1$ and $\varepsilon_N = 1)$ and replace the operators of conduction electrons with the Fourier components in each interval I_n,

$$a^{(\dagger)}_{p\sigma,n} = \frac{1}{\sqrt{d_n}} \int_{I_n} d\varepsilon\ a^{(\dagger)}_{\varepsilon,\sigma} e^{-i2p\pi|\varepsilon|/d_n}, \tag{3.8}$$

with $d_n = |\varepsilon_{n+1} - \varepsilon_n|$ and $p = 0, 1, 2, 3, \cdots$. At the end, we drop all the non-zero p-terms and write the Hamiltonian only with the zero-th Fourier components, $a^{(\dagger)}_{0\sigma,n}$, in each interval. This, so called $p = 0$ approximation, is the first approximation in NRG.

Let us look into the hybridization and the kinetic term of the Hamiltonian to check the validity of the approximation. The hybridization term is given as

$$H_{hyb} = \sum_n \int_{I_n} d\varepsilon\ h_n f^\dagger_{-1\sigma} a_{\varepsilon\sigma} + h.c.. \tag{3.9}$$

Assuming that $h(\varepsilon)$ is constant in each interval I_n,

$$h(\varepsilon) = h_n = const.\ ,\ \varepsilon \in I_n. \tag{3.10}$$

makes H_{hyb} in Eq. (3.9) consist of only the "$p = 0$" Fourier components $\{a_{0\sigma,n}\}$.

$$\begin{aligned} H_{hyb} &= \sum_n h_n f^\dagger_{-1\sigma} \int_{I_n} d\varepsilon a_{\varepsilon\sigma} + h.c. \\ &= \sum_n \sum_p \frac{h_n}{\sqrt{d_n}} f^\dagger_{-1\sigma} \int_{I_n} d\varepsilon \sum_q a_{q\sigma,n}\ e^{i2q\pi|\varepsilon|/d_n} + h.c. \\ &= \sum_n h_n \sqrt{d_n} f^\dagger_{-1\sigma} a_{0\sigma,n} + h.c.. \end{aligned} \tag{3.11}$$

The energy-dependence of $V(\varepsilon)$ and $\rho(\varepsilon)$ is fully attributed to the inverse-dispersion function $\varepsilon(x)(= g^{-1}(x))$ such that

$$\frac{\partial\varepsilon(x)}{\partial x} = \frac{1}{h_n^2} V(\varepsilon(x))^2 \rho(\varepsilon(x)), \tag{3.12}$$

with $\varepsilon(x) \in [\varepsilon_n, \varepsilon_{n+1}]$. Thus there is no approximation up to this point.

The kinetic term of Hamiltonian with full Fourier components $\{a^{(\dagger)}_{p\sigma,n}\}$ is

$$\begin{aligned} H_{kinetic} &= \sum_\sigma \sum_n \int_{I_n} d\varepsilon\ g_n(\varepsilon) a^\dagger_{\varepsilon\sigma} a_{\varepsilon\sigma} \\ &= \sum_\sigma \sum_n \frac{1}{d_n} \sum_{p,q} \int_{I_n} d\varepsilon\ g_n(\varepsilon) a^\dagger_{p\sigma,n} e^{-i2p\pi|\varepsilon|/d_n} a_{q\sigma,n} e^{i2q\pi|\varepsilon|/d_n} \\ &= \sum_\sigma \sum_n \frac{1}{d_n} a^\dagger_{0\sigma,n} a_{0\sigma,n} \int_{I_n} d\varepsilon\ g_n(\varepsilon) \\ &\quad + \sum_\sigma \sum_n \frac{1}{d_n} \sum_{p\neq 0} a^\dagger_{p\sigma,n} a_{p\sigma} \int_{I_n} d\varepsilon\ g_n(\varepsilon) \\ &\quad + \sum_\sigma \sum_n \frac{1}{d_n} \sum_{p\neq 0} a^\dagger_{p\sigma,n} a_{0\sigma,n} \int_{I_n} d\varepsilon\ g_n(\varepsilon) e^{-i2p\pi|\varepsilon|/d_n} \\ &\quad + \sum_\sigma \sum_n \frac{1}{d_n} \sum_{q\neq 0} a^\dagger_{0\sigma,n} a_{q\sigma} \int_{I_n} d\varepsilon\ g_n(\varepsilon) e^{i2q\pi|\varepsilon|/d_n} \\ &\quad + \sum_\sigma \sum_n \frac{1}{d_n} \sum_{p\neq 0} \sum_{k\neq 0} a^\dagger_{p\sigma,n} a_{p+k\sigma,n} \int_{I_n} d\varepsilon\ g_n(\varepsilon) e^{i2k\pi|\varepsilon|/d_n} \end{aligned} \tag{3.13}$$

Neglecting the last three terms in the above Hamiltonian reduces the full Hamil-

tonian in Eq. (3.3) into a form:

$$\begin{aligned} H &\cong \varepsilon_f \sum_\sigma f^\dagger_{-1\sigma} f_{-1\sigma} + U f^\dagger_{-1\uparrow} f_{-1\uparrow} f^\dagger_{-1\downarrow} f_{-1\downarrow} \\ &+ \sum_\sigma \sum_n \xi_n a^\dagger_{0\sigma,n} a_{0\sigma,n} + \sum_\sigma \sum_n h_n \sqrt{d_n} (f^\dagger_{-1\sigma} a_{0\sigma,n} + a^\dagger_{0\sigma,n} f_{-1\sigma}) \\ &+ \sum_\sigma \sum_n \sum_{p\neq 0} \xi_n a^\dagger_{p\sigma,n} a_{p\sigma,n}, \end{aligned} \tag{3.14}$$

with

$$\begin{aligned} h_n^2 &= \frac{1}{\pi d_n} \int_{I_n} d\varepsilon\ \Delta(\varepsilon), \\ \xi_n &= \frac{\int_{\varepsilon_n}^{\varepsilon_{n+1}} d\varepsilon\ \varepsilon\Delta(\varepsilon)}{\int_{\varepsilon_n}^{\varepsilon_{n+1}} d\varepsilon\ \Delta(\varepsilon)}, \quad \int_{I_n} d\varepsilon\ = \int_{\varepsilon_n}^{\varepsilon_{n+1}} d\varepsilon. \end{aligned} \tag{3.15}$$

Disregarding the last term of Eq. (3.14) that is completely irrelevant to the others keeps only the $p = 0$ Fourier components in the Hamiltonian:

$$\begin{aligned} H &\cong \varepsilon_f \sum_\sigma f^\dagger_{-1\sigma} f_{-1\sigma} + U f^\dagger_{-1\uparrow} f_{-1\uparrow} f^\dagger_{-1\downarrow} f_{-1\downarrow} \\ &+ \sum_\sigma \sum_n \xi_n a^\dagger_{0\sigma,n} a_{0\sigma,n} + \sum_\sigma \sum_n h_n \sqrt{d_n} (f^\dagger_{-1\sigma} a_{0\sigma,n} + a^\dagger_{0\sigma,n} f_{-1\sigma}) \\ &= \varepsilon_f \sum_\sigma f^\dagger_{-1\sigma} f_{-1\sigma} + U f^\dagger_{-1\uparrow} f_{-1\uparrow} f^\dagger_{-1\downarrow} f_{-1\downarrow} \\ &+ \sum_\sigma \sum_n \xi_n a^\dagger_{0\sigma,n} a_{0\sigma} + \sum_\sigma (f^\dagger_{-1\sigma} f_{0\sigma} + f^\dagger_{0\sigma} f_{-1\sigma}), \end{aligned} \tag{3.16}$$

with

$$\begin{aligned} f_0 &= \frac{1}{\sqrt{\eta_0}} \sum_n h_n \sqrt{d_n} a_{0\sigma,n} = \frac{1}{\sqrt{\eta_0}} \sum_n \bar{h}_n a_{0\sigma,n}, \\ \eta_0 &= \sum_n \bar{h}_n^2. \end{aligned} \tag{3.17}$$

$$\tag{3.18}$$

The validity of the approximation can be examined by comparing the coefficients of the $p = 0$ Fourier component to the other $p \neq 0$ terms:

$$A_{k,n} \equiv \frac{g_n^{pq}}{g_n^{00}} = \frac{\int_{I_n} d\varepsilon g(\varepsilon) e^{-i2\pi k|\varepsilon|/d_n}}{\int_{I_n} d\varepsilon g(\varepsilon)} \tag{3.19}$$

with $p - q = k \neq 0$.

Assuming a linear dispersion $g(\varepsilon) \propto \varepsilon$[1],

$$\begin{aligned} A_{k,n} &= \frac{\int_{I_n} d\varepsilon\ \varepsilon\ e^{-i2\pi k|\varepsilon|/d_n}}{\int_{I_n} d\varepsilon\ \varepsilon} \\ &= \frac{\int_{\varepsilon_n}^{\varepsilon_{n+1}} d\varepsilon\ \varepsilon\ e^{-i2\pi k|\varepsilon|/d_n}}{\int_{\varepsilon_n}^{\varepsilon_{n+1}} d\varepsilon\ \varepsilon} \\ &= \frac{e^{-i2\pi k\varepsilon_n/d_n}}{-i\pi k}\frac{\varepsilon_{n+1}-\varepsilon_n}{\varepsilon_{n+1}+\varepsilon_n}. \end{aligned} \tag{3.20}$$

Thus, $|A_{n,k}|$ is proportional to the interval-length d_n and inverse-proportional to the frequency difference $|p-q|$ and the mean-energy $\bar{\varepsilon}_n$:

$$|A_{n,k}| = |\frac{g_n^{pq}}{g_n^{00}}| \propto \frac{d_n}{\bar{\varepsilon}_n}\frac{1}{|p-q|}, \tag{3.21}$$

with $d_n = \varepsilon_{n+1} - \varepsilon_n$ and $\bar{\varepsilon}_n = (\varepsilon_{n+1} + \varepsilon_n)/2$. The inverse-proportional factor $1/|p-q|$ makes slow-varying terms more dominant than fast-modulating ones.

Another observation is that $|g_n^{pq}/g_n^{00}|$ is proportional to $d_n/\bar{\varepsilon}_n$, which makes the type of discretization as a crucial point. Let's assume that we discretize a continuous band with a uniform mesh,

$$d_n = D/N = const., \tag{3.22}$$

with the number of divisions N and the band-width D. Now, $|g_n^{pq}/g_n^{00}|$ becomes infinitely large as $\bar{\varepsilon}_n$ approaches to zero and $p = 0$ approximation fails at $\varepsilon \approx 0$. The alternative way is to make $|g_n^{pq}/g_n^{00}|$ energy-independent:

$$|g_n^{pq}/g_n^{00}| \propto \frac{\Delta\varepsilon_n}{\bar{\varepsilon}_n}\frac{1}{k} = const., \tag{3.23}$$

with $\Delta\varepsilon_n = d_n$. Eq. (3.23) lets the energy-mesh uniform in a logarithmic scale.

$$\Delta(\ln \varepsilon_n) = const. \equiv \ln \Lambda \tag{3.24}$$

Here we introduce a control parameter Λ for discretization. In $\Lambda \to 1$ limit, the Hamiltonian in Eq. (3.16) recovers the original Hamiltonian in Eq. (3.3) since

$$\lim_{\Lambda\to 1} |g_n^{pq}/g_n^{00}| = 0. \tag{3.25}$$

According to the historical precedents, values of Λ are mostly $2 \sim 5$, with which one needs to divide a band $[-D, D]$ into about 40-sectors ($2^{-40} \sim 10^{-6}$) or 20-sectors ($5^{-20} \sim 10^{-6}$) to reach the energy scale $T \sim D \times 10^{-6}$. Accordingly, the size of Hamiltonian matrices becomes 4^{40} or 4^{20}.[2]

[1] More general cases involve complicate integrand in Eq. (3.19) but we believe that the same arguments as followings can be applied to the cases, too.

[2] All these numbers refer to fermionic systems.

NRG deals with those many electronic degrees of freedom in a certain sequence (iteratively). How do we distribute the huge number of electrons into a sequence of diagonalization steps? How can one describe the correlations among the electrons in different steps? Section 3.2.2 is devoted to answer the questions.

3.2.2 Iterative diagonalization of a semi-infinite chain

Let us start from the Hamiltonian with $p = 0$ Fourier components only.

$$\begin{aligned} H &= \varepsilon_f \sum_\sigma f^\dagger_{-1\sigma} f_{-1\sigma} + U f^\dagger_{-1\uparrow} f_{-1\uparrow} f^\dagger_{-1\downarrow} f_{-1\downarrow} + \sum_\sigma \sum_n \xi_n a^\dagger_{n\sigma} a_{n\sigma} \\ &+ \sqrt{\eta_0} \sum_\sigma (f^\dagger_{-1\sigma} f_{0\sigma} + f^\dagger_{0\sigma} f_{-1\sigma}), \end{aligned} \tag{3.26}$$

with

$$\begin{aligned} f_{0\sigma} &= \frac{1}{\sqrt{\eta_0}} \sum_n \bar{h}_n a_{n\sigma}, \\ \eta_0 &= \sum_n \bar{h}_n^2. \end{aligned} \tag{3.27}$$

Now we drop the index p $(= 0)$ from the conduction operators $(a^{(\dagger)}_{0\sigma,n} \to a^{(\dagger)}_{n\sigma})$. The well-known Lanczos algorithm for converting matrices to a tridiagonal form maps the Hamiltonian in Eq. (3.26) into a semi-infinite chain.

$$\begin{aligned} H &= \varepsilon_f \sum_\sigma f^\dagger_{-1\sigma} f_{-1\sigma} + U f^\dagger_{-1\uparrow} f_{-1\uparrow} f^\dagger_{-1\downarrow} f_{-1\downarrow} + \sqrt{\eta_0} \sum_\sigma (f^\dagger_{-1\sigma} f_{0\sigma} + f^\dagger_{0\sigma} f_{-1\sigma}) \\ &+ \sum_\sigma \sum_n \left[\varepsilon_n f^\dagger_{n\sigma} f_{n\sigma} + t_n (f^\dagger_{n\sigma} f_{n+1\sigma} + f^\dagger_{n+1\sigma} f_{n\sigma}) \right] \end{aligned} \tag{3.28}$$

where operators $f^{(\dagger)}_{n\sigma}$ $(n = 1, 2, ...)$ are represented as a linear combination of conduction operators $a^{(\dagger)}_{m\sigma}$ by a real orthogonal transformation U $(U^T U = U U^T = 1,\ U^* = U)$:

$$f_{n\sigma} = \sum_m U_{nm} a_{m\sigma}. \tag{3.29}$$

The parameters of the semi-infinite chain are calculated recursively with the relations (Bulla, Lee, Tong and Vojta 2005),

$$\begin{aligned} \varepsilon_m &= \sum_n \xi_n U^2_{mn}, \\ t^2_m &= \sum_n \left[(\xi_n - \varepsilon_m) U_{mn} - t_{m-1} U_{m-1n} \right]^2, \\ U_{m+1n} &= \frac{1}{t_m} \left[(\xi_n - \varepsilon_m) U_{mn} - t_{m-1} U_{m-1n} \right], \end{aligned} \tag{3.30}$$

starting with the initial conditions,

$$\begin{aligned} U_{0n} &= \frac{h_n}{\sqrt{\xi_0}}. \\ \varepsilon_0 &= \sum_n \xi_n U_{0n}^2. \\ U_{1n} &= \frac{1}{t_0}(\xi_n - \varepsilon_0)U_0. \end{aligned} \tag{3.31}$$

Before discussing the iterative diagonalization procedure, we mention the important consequences of the mapping to a semi-infinite chain.

i) The coefficients $\{\varepsilon_n, t_n\}$ show an exponential decay for large n.

$$\varepsilon_n \propto \Lambda^{-n/2}, t_n \propto \Lambda^{-n/2}, \text{[3]} \tag{3.32}$$

ii) The annihilation(creation) operator of the n-th chain-site $f_{n\sigma}^{(\dagger)}$ can be approximated as a finite sum of $a_{m\sigma}^{(\dagger)}$ instead of the infinite one.

$$\begin{aligned} f_{n\sigma}^{(\dagger)} &= \sum_{m=0}^{\infty} U_{nm}(a_{m\sigma}^{(\dagger)} + (-1)^n b_{m\sigma}^{(\dagger)}) \\ &\approx \sum_{m=i}^{f} U_{nm}(a_{m\sigma}^{(\dagger)} + (-1)^n b_{m\sigma}^{(\dagger)}) \end{aligned} \tag{3.33}$$

We will use the two results with discussing the details of the truncation procedure.

Let us define a finite size of Hamiltonian from the semi-infinite chain in Eq. (3.28)

$$\begin{aligned} H_N &= \varepsilon_f \sum_\sigma f_{-1\sigma}^\dagger f_{-1\sigma} + U f_{-1\uparrow}^\dagger f_{-1\uparrow} f_{-1\downarrow}^\dagger f_{-1\downarrow} + \sqrt{\eta_0} \sum_\sigma (f_{-1\sigma}^\dagger f_{0\sigma} + f_{0\sigma}^\dagger f_{-1\sigma}) \\ &+ \sum_\sigma \left[\sum_{n=0}^{N} \varepsilon_n f_{n\sigma}^\dagger f_{n\sigma} + \sum_{n=0}^{N-1} t_n (f_{n\sigma}^\dagger f_{n+1\sigma} + f_{n+1\sigma}^\dagger f_{n\sigma}) \right] \end{aligned} \tag{3.34}$$

[3] $\Lambda^{-n/2}$:Fermions, Λ^{-n}:Bosons

The semi-infinite chain is solved iteratively by starting from H_0 and successively adding the next site.

$$\begin{aligned}
H_0 &= H_{imp} + \sqrt{\xi_0}\sum_\sigma (f^\dagger_{-1\sigma} f_{0\sigma} + f^\dagger_{0\sigma} f_{-1\sigma}) + \varepsilon_0 \sum_\sigma f^\dagger_{0\sigma} f_{0\sigma} \\
H_1 &= H_0 + t_0 \sum_\sigma (f^\dagger_{0\sigma} f_{1\sigma} + f^\dagger_{1\sigma} f_{0\sigma}) + \varepsilon_1 \sum_\sigma f^\dagger_{1\sigma} f_{1\sigma} \\
H_2 &= H_1 + t_1 \sum_\sigma (f^\dagger_{1\sigma} f_{2\sigma} + f^\dagger_{2\sigma} f_{1\sigma}) + \varepsilon_2 \sum_\sigma f^\dagger_{2\sigma} f_{2\sigma} \\
H_3 &= H_2 + t_2 \sum_\sigma (f^\dagger_{2\sigma} f_{3\sigma} + f^\dagger_{3\sigma} f_{2\sigma}) + \varepsilon_3 \sum_\sigma f^\dagger_{3\sigma} f_{3\sigma} \\
&... \\
H_{N+1} &= H_N + t_N \sum_\sigma (f^\dagger_{N\sigma} f_{N+1\sigma} + f^\dagger_{N+1\sigma} f_{N\sigma}) + \varepsilon_{N+1} \sum_\sigma f^\dagger_{N+1\sigma} f_{N+1\sigma}
\end{aligned} \tag{3.35}$$

To prevent the rapid growth of the Hilbert space, it is indispensable to discard some of eigenstates before including an additional conduction site to the Hamiltonian. Let us assume that the Hamiltonian of the $N-1$-th iterative step, H_{N-1}, yields M of eigenstates,

$$H_{N-1}|\phi^{(N-1)}_n\rangle = E^{(N-1)}_n |\phi^{(N-1)}_n\rangle \tag{3.36}$$

with $n = 1, 2, ...M$.

The matrix representation of a new Hamiltonian H_N is based on the product states

$$|\psi^{(N)}_{nm}\rangle = |\phi^{(N-1)}_n\rangle \otimes |m\rangle,\ (n = 1, 2, ..., M,\ m = 1, 2, ..., l), \tag{3.37}$$

where $\{|m\rangle | m = 1, 2, ..., l\}$ corresponds to a basis for a new site. In fermionic cases

$$\begin{aligned}
|\Omega\rangle &= |0\rangle, \\
|\uparrow\rangle &= f^\dagger_{N\uparrow}|0\rangle, \\
|\downarrow\rangle &= f^\dagger_{N\downarrow}|0\rangle, \\
|\uparrow\downarrow\rangle &= f^\dagger_{N\uparrow} f^\dagger_{N\downarrow}|0\rangle.
\end{aligned} \tag{3.38}$$

The matrix elements of the new Hamiltonian H_N is

$$\begin{aligned}
\langle\psi^{(N)}_{n'm'}|H_N|\psi^{(N)}_{nm}\rangle &= \langle m'|m\rangle\langle\phi^{(N-1)}_{n'}|H_{N-1}|\phi^{(N-1)}_n\rangle + \varepsilon_N\langle\phi^{(N-1)}_{n'}|\phi^{(N-1)}_n\rangle\langle m'|f^\dagger_{N\sigma} f_{N\sigma}|m\rangle \\
&+ t_{N-1}\langle\phi^{(N-1)}_{n'}|f^\dagger_{N-1\sigma}|\phi^{(N-1)}_{n\sigma}\rangle\langle m'|f_{N\sigma}|m\rangle \\
&+ t_{N-1}\langle\phi^{(N-1)}_{n'}|f_{N-1\sigma}|\phi^{(N-1)}_{n\sigma}\rangle\langle m'|f^\dagger_{N\sigma}|m\rangle.
\end{aligned} \tag{3.39}$$

with $|\psi^{(N-1)}_{nm}\rangle = |\phi^{(N-1)}_n\rangle \otimes |m\rangle$ and $|m\rangle \in \{|\Omega\rangle, |\uparrow\rangle, |\downarrow\rangle, |\uparrow\downarrow\rangle\}$.

In NRG, we truncate the matrix of Hamiltonian by keeping the first $N_s \times N_s$ elements out of the $M \times M$ ones and discarding the remnants.

The truncated Hamiltonian gives a valid result (low-lying spectrums $\{E_n^{(N)}\}$) only if the off-diagonal elements for $|n-n'|>N_s$ are negligibly small compared to the diagonal ones:

$$\langle\psi_{n'm'}^{(N)}|H_N|\psi_{nm}^{(N)}\rangle \ll \langle\psi_{nm}^{(N)}|H_N|\psi_{nm}^{(N)}\rangle \tag{3.40}$$

for $|n-n'|>N_s$. Equivalently,

$$t_{N-1}\langle\phi_{n'}^{(N-1)}|f_{N-1\sigma}^{\dagger}|\phi_n^{(N-1)}\rangle\langle m'|f_{N\sigma}|m\rangle \ll E_n^{(N-1)}+\varepsilon_N\langle m|f_N^{\dagger}f_N|m\rangle \tag{3.41}$$

for $|n-n'|>N_s$.

Now, we check the order of magnitude of each element in Eq. (3.41). The first result in Eq. (3.32) tells us, for a given N, t_{N-1} and ε_N are same in order of magnitude:

$$t_N, \varepsilon_N \sim \Lambda^{-N/2}. \tag{3.42}$$

Two new elements, $\langle m|f_{N\sigma}^{\dagger}f_{N\sigma}|m\rangle$ and $\langle m'|f_{N\sigma}^{(\dagger)}|m\rangle$, are order of unity:

$$\begin{aligned}\langle m|f_{N\sigma}^{\dagger}f_{N\sigma}|m\rangle &\in \{0,1,2\},\\ \langle m'|f_{N\sigma}|m\rangle &\in \{0,1\}.\end{aligned} \tag{3.43}$$

To make simple explanation, we replace $E_n^{(N-1)}$ to $E_1^{(N-1)}$ and check the inequality (3.41). Since $E_1^{(N-1)}$ corresponds to the first excitation-energy of the Hamiltonian H_{N-1}[4], its energy-scale has to be similar to ε_{N-1} and t_{N-1} in order of magnitude.

$$E_1^{(N-1)} \sim \Lambda^{-N/2} \tag{3.44}$$

From Eq. (3.42), Eq. (3.44) and Eq. (3.44), we can conclude that the inequality (3.41) is satisfied (or truncation is allowed) if we can find an integer N_s smaller than M such that

$$\langle\phi_{n'}^{(N-1)}|f_{N-1,\sigma}^{\dagger}|\phi_n^{(N-1)}\rangle \ll 1, \tag{3.45}$$

for $N_s<|n-n'|<M$. To find a proper N_s, we use the result in Eq. (3.33). The finite summation in Eq. (3.33) begins with $m=i$ and stops at $m=f$, which means $f_{N-1,\sigma}$ involves the single-particle(hole) operators, $a_{m\sigma}(b_{m\sigma})$, with energy ξ_m smaller than ξ_i and larger than ξ_f.

$$\xi_f<\xi_m<\xi_i \quad \text{for} \quad i<m<f \tag{3.46}$$

Thus, the transition amplitude $\langle\phi_{n'}^{(N-1)}|f_{N-1,\sigma}^{\dagger}|\phi_n^{(N-1)}\rangle$ becomes effectively zero for

$$|E_{n'}^{(N-1)}-E_n^{(N-1)}|>\xi_i^{(N-1)} \tag{3.47}$$

[4] To be precise, $E_1^{(N-1)}$ is the energy-difference between the ground state and the first excited one.

and the subspace of the full Hamiltonian H_N with energy $0 \leq E_n^{(N-1)} \leq \xi_i^{(N-1)}$ can be effectively described by a truncated Hamiltonian $H_N(N_s l \times N_s l)$ where N_s is defined to satisfy

$$E_{N_s}^{(N-1)} \approx 2\xi_i. \tag{3.48}$$

The energy cutoff $\xi_i^{(N-1)}$ of the operator $f_{N-1,\sigma}$ shows exponential decrease and for large $N(> 10)$,

$$\xi_i^{(N-1)} \propto \Lambda^{-N/2}.^{5} \tag{3.49}$$

If Λ is very close to 1, the cut-off does not change so much with iterations but stays at the initial cut-off (band width) D and there is very little room for truncation. A large $\Lambda(\gg 1)$ makes computation easy but we lose too much information with logarithmic discretization (or $p = 0$ approximation).[6] Optimal values of Λ can be different according to the kind of models and also to the type of physical properties to be calculated. For examples, physics at the ground-state are usually obtained with a large value of $\Lambda(\sim 5)$ whereas relatively small $\Lambda(\sim 2)$ is demanded to investigate temperature-dependence of (thermo)dynamical quantities.

3.3 Flow diagrams and Fixed points

In analytic RG approach, the renormalization group is a mapping R of a Hamiltonian $H(\boldsymbol{K})$, which is specified by a set of interaction parameters or couplings $\boldsymbol{K} = (K_1, K_2, ...)$ into another Hamiltonian of the same form with a new set of coupling parameters $\boldsymbol{K'} = (K_1', K_2', ...)$. This is expressed formally by

$$R\{H(\boldsymbol{K})\} = H(\boldsymbol{K'}), \tag{3.50}$$

or equivalently,

$$R\{\boldsymbol{K}\} = \boldsymbol{K'}. \tag{3.51}$$

In applications to critical phenomena the new Hamiltonian is obtained by removing short range fluctuations to generate an effective Hamiltonian valid over larger length scales. The transformation is usually characterized by a parameter, say α, which specifies the ratio of the new length or energy scale to the old one. A sequence of transformations,

$$\boldsymbol{K'} = R_\alpha(\boldsymbol{K}),\ \boldsymbol{K''} = R_\alpha(\boldsymbol{K'}),\ \boldsymbol{K'''} = R_\alpha(\boldsymbol{K''}),\ etc. \tag{3.52}$$

generates a sequence of points or, where α is a continuous variable, a *trajectory* in the parameter space $\boldsymbol{K}$.

[5] In actual calculations, truncation is controlled by keeping the number of states constant.
[6] see Section 3.2.1

In numerical renormalization group approach, RG-transformation corresponds to a mapping of a iterative Hamiltonian H_N into H_{N+1}

$$\begin{aligned} H_{N+1} &= R(H_N) \\ &= H_N + t_N \sum_\sigma (f^\dagger_{N\sigma} f_{N+1\sigma} + f^\dagger_{N+1\sigma} f_{N\sigma}) + \varepsilon_{N+1} \sum_\sigma f^\dagger_{N+1\sigma} f_{N+1\sigma}. \end{aligned} \tag{3.53}$$

Including truncation-procedures, which keep the dimension of the iterative Hamiltonian H_N constant[7], defines R as a mapping between the points in a space of $N_s \times N_s$ - matrices.

A fixed point, one of the key concepts of the renormalization group, is a point K^* which is invariant under the RG-transformation.

$$R(K^*) = K^* \tag{3.54}$$

In the NRG method, a fixed point K^* is an invariant Hamiltonian H^* under the transformation in Eq. (3.53) and the iterative Hamiltonian H_N converges into the fixed point H^*:[8]

$$H^* = \lim_{N\to\infty} H_N. \tag{3.55}$$

We write the fixed point Hamiltonian H^* in terms of $N_s \times N_s$ matrix:

$$H^* = \sum_{n=1}^{N_s} E^*_n |\psi^*_n\rangle\langle\psi^*_n|, \tag{3.56}$$

where $|\psi^*_n\rangle$ and E^*_n are the eigenstates and eigenvalues of H^* so that

$$H^*|\psi^*_n\rangle = E^*_n|\psi^*_n\rangle, \quad (n = 1, ...N_s). \tag{3.57}$$

Using the eigenbasis in Eq. (3.57), H_N can be written as

$$H_N = \sum_{n=1}^{N_s}\sum_{m=1}^{N_s} h^{(N)}_{nm} |\psi^*_n\rangle\langle\psi^*_m|. \tag{3.58}$$

Inserting Eq. (3.56) and Eq. (3.58) to Eq. (3.55) gives:

$$\lim_{N\to\infty} h^{(N)}_{nm} = 0 \text{ for all n} \neq \text{m}. \tag{3.59}$$

In actual calculations, the eigenstates of $\hat{H}^*$ in Eq. (3.56) is obtained iteratively and each of iteration yields a diagonalized Hamiltonian H_N on the eigen-

[7] $\dim[H_N]=N_s$ for every iteration

[8] Precisely, the Eq. (3.53) is a definition for stable fixed points only.

basis $\{|\psi_n^{(N)}\rangle\}$.

$$\begin{aligned} H_0 &= \sum_{n=1}^{N_s} E_n^{(0)} |\psi_n^{(0)}\rangle\langle\psi_n^{(0)}| \\ H_1 &= \sum_{n=1}^{N_s} E_n^{(1)} |\psi_n^{(1)}\rangle\langle\psi_n^{(1)}| \\ &\cdot \\ &\cdot \\ &\cdot \\ H_N &= \sum_{n=1}^{N_s} E_n^{(N)} |\psi_n^{(N)}\rangle\langle\psi_n^{(N)}| \\ H_{N+1} &= \sum_{n=1}^{N_s} E_n^{(N+1)} |\psi_n^{(N+1)}\rangle\langle\psi_n^{(N+1)}| \end{aligned} \tag{3.60}$$

where $H_m|\psi_n^{(m)}\rangle = E_n^{(m)}|\psi_n^{(m)}\rangle$, $(m = 0, 1, ..., N+1$ and $n = 1, ..., N_s)$.

The iterative Hamiltonian H_N approaches to the fixed point H^* as the eigenstates $\{|\psi_n^{(N)}\rangle\}$ converges to constant states $\{|\psi_n^*\rangle\}$:

$$\lim_{N\to\infty} |\psi_n^{(N)}\rangle = |\psi_n^*\rangle, \tag{3.61}$$

for $n = 1, ..., N_s$.

Once the iterative Hamiltonian is very close to a fixed point, the mapping R hardly affects the structure of Hamiltonian but changes the overall energy-scale as α.[9]

A sequence of transformations gives

$$\begin{aligned} H_{N+1} &= R_\alpha(H_N) &&= \alpha\ H_N + O(1/N) \\ H_{N+2} &= R_\alpha(H_{N+1}) &&= \alpha^2\ H_N + O(1/N) \\ H_{N+3} &= R_\alpha(H_{N+2}) &&= \alpha^3\ H_N + O(1/N) \\ &... \end{aligned} \tag{3.62}$$

If we define an renormalized Hamiltonian $\bar{H}_N$ where overall energy scale is divided by α^N, $(\bar{H}_N = H_N \times \frac{1}{\alpha^N})$

$$\begin{aligned} \bar{H}_{N+1} &= \bar{H}_N + O(1/N) \\ \bar{H}_{N+2} &= \bar{H}_N + O(1/N) \\ \bar{H}_{N+3} &= \bar{H}_N + O(1/N) \\ &... \end{aligned} \tag{3.63}$$

[9] In fermionic (bosonic) NRG, $\alpha = 1/\sqrt{\Lambda}$ $(1/\Lambda)$.

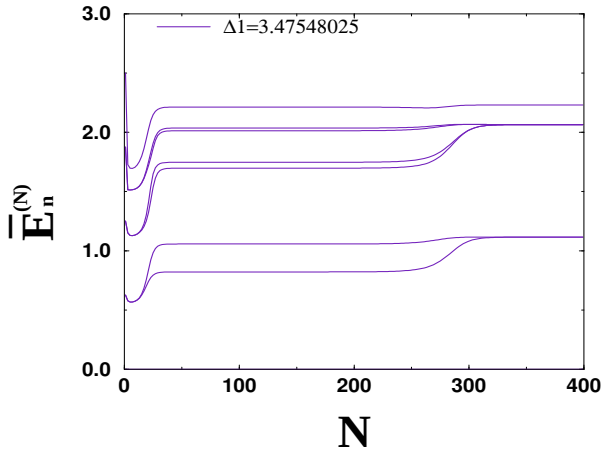

Figure 3.1: Many particle spectrums of Soft-Gap Anderson Model: The lowest seven levels for given quantum numbers $Q = 0$ and $S = 1/2$. :$\{\bar{E}_n^{(N)} \mid n = 1, 2, ...7\}$

Now, convergence of $\{|\psi_n^{(N)}\rangle\}$ directly gives convergence of renormalized eigenvalues $\bar{E}_n^{(N)}$:

$$\lim_{N\to\infty} \bar{E}_n^{(N)} = const. \equiv \bar{E}_n^*, \tag{3.64}$$

where

$$\bar{H}_N|\psi_n^{(N)}\rangle = \bar{E}_n^{(N)}|\psi_n^{(N)}\rangle. \tag{3.65}$$

Since it is more convenient to find fixed points with the renormalized Hamiltonian, $\bar{H}_N$, we introduce the scale factor α into the numerical procedure and obtain the eigenstates of $\bar{H}_N$ rather than that of H_N. In a formal expression, NRG transformation is written with $\bar{H}_N$:

$$\begin{aligned} \bar{H}_{N+1} &= R_\alpha(\bar{H}_N) \\ &= \frac{1}{\alpha}\left[\bar{H}_N + \bar{t}_N \sum_\sigma (f_{N\sigma}^\dagger f_{N+1\sigma} + f_{N+1\sigma}^\dagger f_{N\sigma}) + \bar{\varepsilon}_{N+1} \sum_\sigma f_{N+1\sigma}^\dagger f_{N+1\sigma}\right] \end{aligned} \tag{3.66}$$

with $\bar{H}_N = H_N/\alpha^N$, $\bar{t}_N = t_N/\alpha^N$, $\bar{\varepsilon}_{N+1} = \varepsilon_{N+1}/\alpha^N$. Eq. (3.66) is obtained with dividing both sides of Eq. (3.53) by α^{N+1}.

The NRG flow-diagram shows many-particles spectrums $\{\bar{E}_n^{(N)}\}$ (vertical axis) as a function of the iteration number N (horizontal axis). In Fig. 3.1, we observe two flat regions, ($N > 300$ and $50 < N < 200$), where $\{\bar{E}_n^{(N)}\}$ are almost independent on N. For $N > 300$, $\{\bar{E}_n^{(N)}\}$ satisfies the condition in Eq. (3.64), flowing (converging) to a fixed point, in particular, a stable fixed point. The other region ($50 < N < 200$), showing another constant structure of many-particles levels, also represents a fixed point but appears (survives) in the finite range of energy-scale. This is called an unstable fixed point as distinguished from the former

case. Summarizing,

$$R(\bar{H}_N) = \bar{H}_N + O(1/N) \approx K^* \qquad \text{for N} > 300 \tag{3.67}$$

$$R(\bar{H}_N) = \bar{H}_N + O(1/N) \approx J^* \qquad \text{for } 50 < \text{N} < 200 \tag{3.68}$$

where K^* and J^* are stable and unstable fixed points, respectively.

In most of RG approaches, fixed points themselves are important objects for investigations. Furthermore, when a model Hamiltonian shows more than one fixed point in the energy or parameter space, correlations among the fixed points are the most crucial points to understand the static/dynamical mechanisms of the model.

4. SOFT-GAP ANDERSON MODEL

4.1 Introduction

The Hamiltonian of the soft-gap Anderson model is given by

$$H = \varepsilon_f \sum_\sigma f_\sigma^\dagger f_\sigma + U f_\uparrow^\dagger f_\uparrow f_\downarrow^\dagger f_\downarrow + \sum_{k\sigma} \varepsilon_k c_{k\sigma}^\dagger c_{k\sigma} + V \sum_{k\sigma} (f_\sigma^\dagger c_{k\sigma} + c_{k\sigma}^\dagger f_\sigma). \qquad (4.1)$$

This model describes the coupling of electronic degrees of freedom at an impurity site (operators $f_\dagger^{(\dagger)}$ to a fermionic bath (operators $c_{k\sigma}^{(\dagger)}$) via a hybridization V. The f-electrons are subject to a local Coulomb repulsion U, while the fermionic bath consists of a non-interacting conduction band with dispersion ε_k. The model Eq. (4.1) has the same form as the single impurity Anderson model (Hewson 1993) but for the soft-gap model we require that the hybridization function

$$\tilde{\Delta}(\omega) = \pi V^2 \sum_k \delta(\omega - \varepsilon_k) \qquad (4.2)$$

has a soft-gap at the Fermi level,

$$\tilde{\Delta}(\omega) = \Delta |\omega|^r, \qquad (4.3)$$

with an exponent $r > 0$. This translates into a local conduction band density of states $\rho(\omega) = \rho_0 |\omega|^r$ at low energies. The power-law density of states was first introduced for the Kondo model (Withoff and Fradkin 1990). In contrast to the usual Kondo model, where conduction-electrons with a non-zero density of states at the Fermi energy form a Kondo-screening state for $T \to 0$, a gap vanishing at the Fermi energy brings about a non-trivial zero temperature critical point at a finite coupling constant J_c and the Kondo effect occurs only for $J > J_c$. The existence of the critical point was derived using a generalization of the "poor-man's-scaling" method for the density of states given in Eq. (4.3).

$$J_R \;=\; (D'/D)^r J' \approx J + J(JCD^r - r)\delta E/D \qquad (4.4)$$

In addition to the fixed points at $J = 0$ and ∞, there is a new infrared unstable fixed point at

$$J_c \;=\; r/CD^r \qquad (4.5)$$

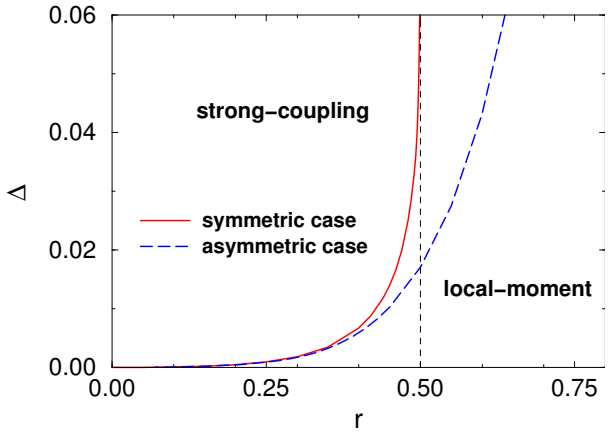

Figure 4.1: $T = 0$ phase diagram for the soft-gap Anderson model in the particle-hole symmetric case (solid line, $U = 10^{-3}$, $\varepsilon_f = -0.5 \times 10^{-3}$, conduction band cutoff at -1 and 1) and the p-h asymmetric case (dashed line, $\varepsilon_f = -0.4 \times 10^{-3}$); Δ measures the hybridization strength $\tilde{\Delta}(\omega) = \Delta|\omega|^r$

with neglecting terms beyond J^2. This result was confirmed by a large degeneracy technique (Withoff and Fradkin 1990). For $J > J_c$, the Kondo temperature T_0 was found to vanish at J_c like

$$T_0 \approx |J - J_c|^{1/r} \tag{4.6}$$

Extensive NRG studies on the single-impurity Anderson model with power-law density of states were devoted to describe the physical properties of the three quantum phases, local-moment, strong coupling and quantum critical phases. We now briefly describe the results (Chen, Jayaprakash and Krishna-Murthy 1992, Gonzalez-Buxton and Ingersent 1998, Bulla, Pruschke and Hewson 1997, Bulla, Glossop, Logan and Pruschke 2000).

Figure 4.1 shows a typical phase diagram for the soft-gap Anderson model. In the particle-hole symmetric case (solid line) the critical coupling Δ_c diverges at $r = \frac{1}{2}$, and no screening occurs for $r > 1/2$. No divergence occurs for particle-hole asymmetry (dashed line).

Due to the power-law conduction band density of states, already the stable LM and SC fixed points show non-trivial behavior. The LM phase has the properties of a free spin $\frac{1}{2}$ with residual entropy $S_{imp} = k_B \ln 2$ and low-temperature impurity susceptibility $\chi_{imp} = 1/(4k_BT)$, but the leading corrections show r-dependent power laws. The p-h symmetric SC fixed point has very unusual properties, namely $S_{imp} = 2rk_B \ln 2$, $\chi_{imp} = r/(8k_BT)$ for $0 < r < \frac{1}{2}$. In contrast, the p-h asymmetric SC fixed point simply displays a completely screened moment, $S_{imp} = T\chi_{imp} = 0$. The impurity spectral function follows an ω^r power law at both the LM and the asymmetric SC fixed point, whereas it diverges as ω^{-r} at the

symmetric SC fixed point [This "peak" can be viewed as a generalization of the Kondo resonance in the standard case ($r = 0$), and scaling of this peak is observed upon approaching the SC-LM phase boundary (Logan and Glossop 2000, Bulla, Pruschke and Hewson 1997, Bulla et al. 2000).]

At the critical point, non-trivial behavior corresponding to a fractional moment can be observed: $S_{imp} = k_B C_s(r)$, $\chi_{imp} = C_\chi(r)/(k_B T)$ with C_s, C_χ being universal functions of r. The spectral functions at the quantum critical points display an ω^{-r} power law (for $r < 1$) with a remarkable "pinning" of the critical exponent.

Apart from the static and dynamic observables described above, the NRG provides information about the many-body excitation spectrum at each fixed point. The non-trivial character of the quantum critical points are prominent in this case, too. For the strong-coupling and local-moment fixed points, a detailed understanding of the NRG levels is possible since the fixed point can be described by non-interacting electrons. Intermediate-coupling fixed point at the quantum critical points have a completely different NRG level structure, i.e., smaller degeneracies and non-equidistant levels. They cannot be cast into a free-particle description.

In this chapter, we demonstrate that a complete understanding of the NRG many-body spectrum of critical fixed points is actually possible, by utilizing renormalized perturbation theory around a non-interacting fixed point. In the soft-gap Anderson model, this approach can be employed near certain values of the bath exponent which can be identified as critical dimensions. Using the knowledge from perturbative RG calculations, which yield the relevant coupling constants being parametrically small near the critical dimension, we can construct the entire quantum critical many-body spectrum from a free-Fermion model supplemented by a small perturbation. In other words, we shall perform epsilon-expansions to determine a complete many-body spectrum (instead of certain renormalized couplings or observables). Conversely, our method allows us to identify relevant degrees of freedom and their marginal couplings by carefully analyzing the NRG spectra near critical dimensions of impurity quantum phase transitions.

This chapter is organized as follows. In Section 4.2 we summarize the recent results from perturbative RG for both the soft-gap Anderson and Kondo models. In Section 4.3, we discuss (i) the numerical data for the structure of the quantum critical points and (ii) the analytical description of these interacting fixed points close to the upper (lower) critical dimension $r = 0$ ($r = 1/2$).

4.2 Results from perturbative RG

The Anderson model (4.1) is equivalent to a Kondo model when charge fluctuations on the impurity site are negligible. The Hamiltonian for the soft-gap Kondo

model can be written as

$$H = J\vec{S} \cdot \vec{s}_0 + \sum_{k\sigma} \varepsilon_k c^\dagger_{k\sigma} c_{k\sigma} \tag{4.7}$$

where $\vec{s}(0) = \sum_{kk'\sigma\sigma'} c^\dagger_{k\sigma} \vec{\sigma}_{\sigma\sigma'} c_{k'\sigma'}/2$ is the conduction electron spin at the impurity site $\mathbf{r} = 0$, and the conduction electron density of states follows a power law $\rho(\omega) = \rho_0 |\omega|^r$ as above.

4.2.1 RG near r=0

For small values of the density of states exponent r, the phase transition in the pseudo-gap Kondo model can be accessed from the weak-coupling limit, using a generalization of Anderson's poor man's scaling. Power counting about the local-moment fixed point (LM) shows that dim[J]= $-r$, i.e., the Kondo coupling is marginal for $r = 0$. We introduce a renormalized dimensionless Kondo coupling j according to

$$\rho_0 J = \mu^{-r} j \tag{4.8}$$

where μ plays the role of a UV cutoff. The flow of the renormalized Kondo coupling j is given by the beta function

$$\beta(j) = rj - j^2 + O(j^3). \tag{4.9}$$

For $r > 0$ there is a stable fixed point at $j^* = 0$ corresponding to the local-moment phase(LM). An unstable fixed point controlling the transition to the strong-coupling phase, exists at

$$j^* = r, \tag{4.10}$$

and the critical properties can be determined in a double expansion in r and j (Vojta and Kirćan 2003). The p-h asymmetry is irrelevant, i.e., a potential scattering term E scales to zero according to $\beta(e) = re$ (where $\rho_0 E = \mu^{-r} e$), thus the above expansion captures the p-h symmetric critical fixed point (SCR). As the dynamical exponent ν, $1/\nu = r + O(r^2)$, diverges as $r \to 0^+$, $r = 0$ plays the role of a lower-critical dimension of the transition under consideration.

4.2.2 RG near r=1/2

For r near 1/2 the p-h symmetric critical fixed point moves to strong Kondo coupling, and the language of the p-h symmetric Anderson model becomes more appropriate (Vojta and Fritz 2004). First, the conduction electrons can be integrated out exactly, yielding a self-energy $\sum_f = V^2 G_{c0}$ for the f electrons, where G_{c0} is the bare conduction electron Green's function at the impurity location. In the low-energy limit the f electron propagator is then given by

$$G_f(i\omega_n)^{-1} = i\omega_n - iA_0 sgn(\omega_n)|\omega_n|^r \tag{4.11}$$

where the $|\omega_n|^r$ self-energy term dominates for $r < 1$, and the prefactor A_0 is

$$A_0 = \frac{\pi\rho_0 V^2}{cos\frac{\pi r}{2}}. \tag{4.12}$$

Eq. (4.11) describes the physics of a non-interacting resonant level model with a soft-gap density of states. Interestingly, the impurity spin is not fully screened for $r > 0$, and the residual entropy is $2r \ln 2$. This precisely corresponds to the symmetric strong-coupling (SC) phase of the soft-gap Anderson and Kondo models (Gonzalez-Buxton and Ingersent 1998). Dimensional analysis, using $\dim[f] = (1-r)/2$ [where f represents the dressed Fermion according to Eq. (4.11)], now shows that the interaction term U of the Anderson model scales as $\dim[U] = 2r - 1$, i.e., it is marginal at $r = 1/2$. This suggests a perturbative expansion in U around the SC fixed point. We introduce a dimensionless renormalized on-site interaction u via

$$U = \mu^{2r-1} A_0^2 u. \tag{4.13}$$

The beta function receives the lowest non-trivial contribution at two-loop order and reads (Vojta and Fritz 2004)

$$\beta(u) = (1-2r)u - \frac{3(\pi - 2\ln 4)}{\pi^2} u^3 + O(u^5). \tag{4.14}$$

For $r < 1/2$ a non-interacting stable fixed point is at $u^* = 0$ - this is the symmetric strong coupling fixed point; it becomes unstable for $r > 1/2$. Additionally, for $r < 1/2$ there is a pair of critical fixed points (SCR, SCR′) located at $u^{*2} = \pi^2(1-2r)/[3(\pi - 2\ln 4)]$, i.e.,

$$u^* = \pm 4.22\sqrt{(}1/2 - r). \tag{4.15}$$

These fixed points describe the transition between an unscreened (spin or charge) moment phase and the symmetric strong-coupling phase (Vojta and Fritz 2004).

Summarizing, both (4.9) and (4.14) capture the same critical SCR fixed point. This fixed point can be accessed either by an expansion around the weak-coupling LM fixed point, i.e., around the decoupled impurity limit, valid for $r \ll 1$, or by an expansion around the strong-coupling SC fixed point, i.e., around a non-interacting resonant-level (or Anderson) impurity, and this expansion is valid for $1/2 - r \ll 1$.

4.3 Structure of the quantum critical points

In Fig. 4.2, the many-particle spectra of the three fixed points (SC: dot-dashed lines, LM: dashed lines, and QCP: solid lines) of the symmetric soft-gap model

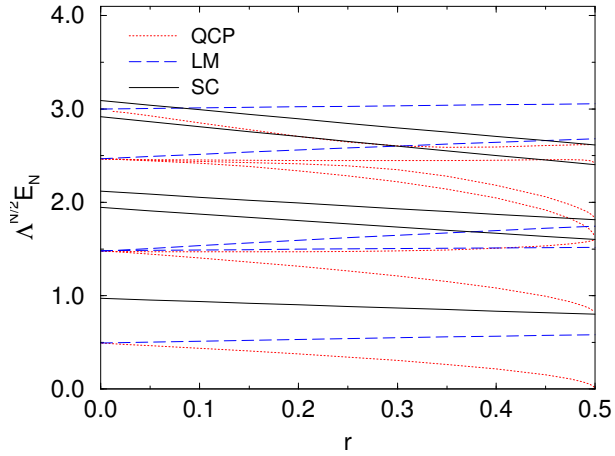

Figure 4.2: Dependence of the many-particle spectra for the three fixed points of the p-h symmetric soft-gap Anderson model on the exponent r: SC (black dot-dashed lines), LM(blue dashed lines), and the (symmetric) quantum critical point (red solid lines). The data are shown for the subspace $Q = 1$ and $S = 0$ only.

are plotted as function of the exponent r.[1] The data are shown for an odd number of sites only and we select the lowest-lying energy levels for the subspace $Q = 1$ and $S = 0$.

As usual, the fixed-point structure of the strong coupling and local moment phases can be easily constructed from the single-particle states of a free conduction electron chain. This is discussed in more detail later. Let us now turn to the line of quantum critical points. What information can be extracted from Fig. 4.2 to understand the structure of these fixed points?

First we observe that the levels of the quantum critical points, $E_{N,QCN}(r)$, approach the levels of the LM (SC) fixed points in the limit $r \to 0$ ($r \to 1/2$):

$$\lim_{r\to 0}\{E_{N,QCP}(r)\} = \{E_{N,LM}(r=0)\} \tag{4.16}$$

$$\lim_{r\to 1/2}\{E_{N,QCP}(r)\} = \{E_{N,SC}(r=1/2)\} \tag{4.17}$$

where $\{...\}$ denotes the whole set of many-particle states.

For $r \to 0$, each individual many-particle level $E_{N,QCP}(r)$ deviates linearly from the levels of the LM fixed point, while the deviation from the SC levels is proportional to $\sqrt{1/2-r}$ for $r \to 1/2$. This is illustrated in Fig. 4.3 where we plot a selection of energy differences ΔE between levels of QCP and SC fixed points close to $r = 1/2$. The inset shows the values of the exponents obtained from a fit to the data points. For some levels, there are significant deviations from the

[1] For a similar figure, see Fig. 13 in (Gonzalez-Buxton and Ingersent 1998)

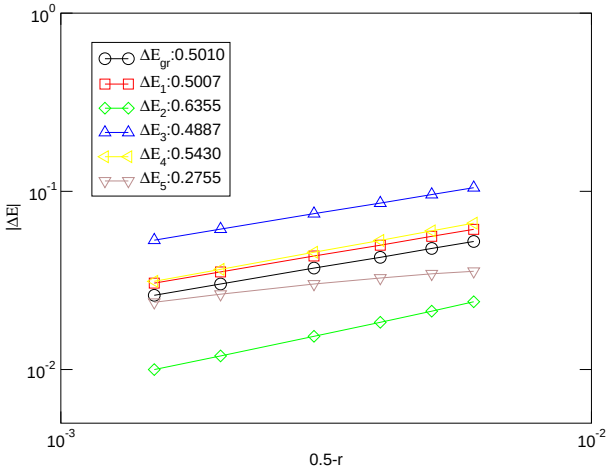

Figure 4.3: Difference ΔE between the energy levels of QCP and SC fixed points close to $r = 1/2$ in a double-logarithmic plot. The inset shows the values of the exponents obtained from a fit to the data points.

exponent 1/2. This is because the correct exponent is only obtained in the limit $r \to 1/2$. (The QCP levels have been obtained only up to $r = 0.4985$.)

Note that the behavior of the many-particle levels close to $r = 1/2$ has direct consequences for physical properties at the QCP; the critical exponent of the local susceptibility at the QCP, for example, shows a square-root dependence on $1/2 - r$ close to $r = 1/2$; see (Gonzalez-Buxton and Ingersent 1998).

In both limits, $r \to 0$ and $r \to 1/2$, we observe that degeneracies due to the combination of single-particle levels, present at the LM and SC fixed points, are lifted at the quantum critical fixed points as soon as one is moving away from $r = 0$ and $r = 1/2$, respectively. This already suggests that the quantum critical point is interacting and cannot be constructed from non-interacting single-particle states.

In the following sections we want to show how to connect this information from NRG to the perturbative RG. We know that the critical fixed point can be accessed via two different epsilon-expansions (Vojta and Kirćan 2003, Vojta and Fritz 2004) near the two critical dimensions, and, combined with renormalized perturbation theory, these expansions can be used to evaluate various observables near criticality. Here, we will employ this concept to perform renormalized perturbation theory for the entire many-body spectrum at the critical fixed point. To do so, we will start from the many-body spectrum of the one of the trivial fixed points, i.e., LM near $r = 0$ and SC near $r = 1/2$, and evaluate corrections to it in lowest-order perturbation theory. This will be done within the NRG concept working directly with the discrete many-body spectra corresponding to a finite NRG-chain (which is diagonalized numerically). As the relevant energy

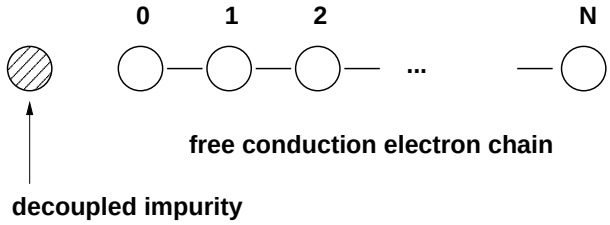

Figure 4.4: The spectrum of the LM fixed point is described by the impurity decoupled from the free conduction electron chain.

scale of the spectra decreases as $\Lambda^{-n/2}$ along the NRG iteration, the strength of the perturbation has to be scaled as well, as the goal is to capture a *fixed point* of the NRG method. This scaling of the perturbation follows precisely from its scaling dimension-the perturbation marginal at the value of r corresponding to the critical dimension. With the proper scaling, the operator which we use to capture the difference between the free-Fermion and critical fixed points becomes exactly marginal.

4.3.1 Perturbation theory close to $r = 0$

Let us now describe in detail the analysis of the deviation of the QCP levels from the LM levels close to $r = 0$. An effective description of the LM fixed point is given by a finite chain with the impurity decoupled from the conduction electron part; (see Fig. A.1). The conduction electron part of the effective Hamiltonian is given by

$$H_{c,N} = \sum_{\sigma n=0}^{N-1} t_n (c^\dagger_{n\sigma} c_{n+1\sigma} + c^\dagger_{n+1\sigma} c_{n\sigma}). \tag{4.18}$$

As usual, the structure of the fixed-point spectra depends on whether the total number of sites is even or odd. To simplify the discussion in the following, we only consider a total *odd* number of sites. For the LM fixed point, this means that the number of sites, $N + 1$, of the free conduction electron chain is even, so N in Eq. (4.18) is odd.

The single-particle spectrum of the free chain with an even number of sites, corresponding to the diagonalized Hamiltonian

$$\bar{H}_{c,N} = \sum_{\sigma p} \epsilon_p \xi^\dagger_{p\sigma} \xi_{p\sigma}, \tag{4.19}$$

is sketched in Fig. 4.4. As we assume p-h symmetry, the positions of the single-particle levels are symmetric with respect to 0 with

$$\epsilon_p = -\epsilon_{-p}, \quad p = 1, 3, \cdots, N, \tag{4.20}$$

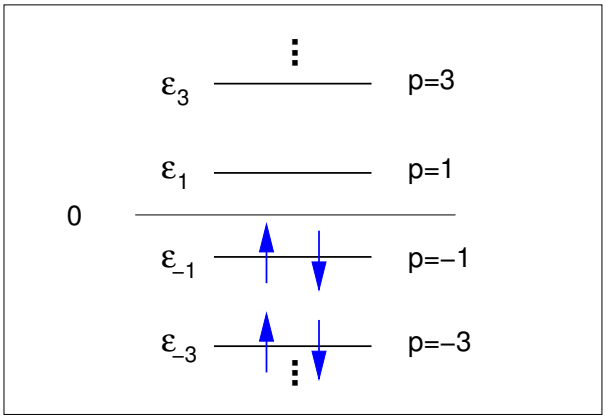

Figure 4.5: Single-particle spectrum of the free conduction electron chain Eq. (A.12). The ground state is given by all the levels with $p < 0$ filled.

and

$$\sum_p \equiv \sum_{p=-N, p \text{ odd}}^{p=N} . \tag{4.21}$$

Note that an equally spaced spectrum of single-particle levels is only recovered in the limit $\Lambda \to 1$; see Fig. 6 in (Bulla, Hewson and Zhang 1997) for the case $r = 0$.

The RG analysis of Section 4.2 tells us that the critical fixed point is perturbatively accessible from the LM one using a Kondo-type coupling as perturbation. We thus focus on the operator

$$H'_N = \alpha(r) f(N) \vec{S}_{imp} \cdot \vec{s}_0, \tag{4.22}$$

with the goal to calculate the many-body spectrum of the critical fixed point via perturbation theory in H'_N for small r. The function $\alpha(r)$ contains the fixed-point value of the Kondo-type coupling, and $f(N)$ will be chosen such that H'_N is exactly marginal, i.e., the effect of H'_N governs the scaling of the many-particle spectrum itself. The scaling analysis of Section 4.2, Eq. (4.8), Eq. (4.10), suggests a parametrization of the coupling as

$$\alpha(r) = \frac{\mu^{-r}}{\rho_0} \alpha r, \tag{4.23}$$

where ρ_0, is the prefactor in the density of states, and μ is a scale of order of the bandwidth-such a factor is required here to make α a *dimensionless* parameter. Thus, the strength of perturbation increases linearly with r at small r (where $\mu^{-r}/\rho_0 = D + O(r)$ for a featureless $|\omega|^r$ density of states).

The qualitative influence of the operator $\vec{S}_{imp} \cdot \vec{s}_0$ on the many-particle states has been discussed in general in (Gonzalez-Buxton and Ingersent 1998) for finite

r and in (Wilson 1975) for $r = 0$. Whereas an anti-ferromagnetic exchange coupling is marginally relevant in the gap-less case ($r = 0$), it turns out to be irrelevant for finite r; see (Gonzalez-Buxton and Ingersent 1998). This is of course consistent with the scaling analysis of Section 4.2: the operator (4.22) shows that it decreases as $\Lambda^{-Nr/2}\Lambda^{-N/2} = \Lambda^{-N(r+1)/2}$ with increasing N. Consequently, we have to choose

$$f(N) = \Lambda^{Nr/2}. \tag{4.24}$$

This result also directly follows from dim[J]$= -r$: as the NRG discretization yields a decrease of the running energy scale of $\Lambda^{-N/2}$, the $\vec{S}_{imp} \cdot \vec{s}_0$ term in Eq. (4.22) scales as $\Lambda^{-Nr/2}$.

The function $f(N)$ is now simply chosen to compensate this effect using Eq. (4.24) scales as $\Lambda^{-Nr/2}$. The function $f(N)$ is now simply chosen to compensate this effect; using Eq. (4.24) the operator H'_N becomes exactly marginal.

Now we turn to a discussion of the many-body spectrum. The relevant ground state of the effective model for the LM fixed point consists of the filled impurity level (with one electron with either spin $\uparrow$ or $\downarrow$) and all the conduction electron states with $p < 0$ filled with both $\uparrow$ and $\downarrow$, as shown in Fig. A.1. Let us now focus on excitations with energy $\epsilon_1+\epsilon_2$ measured with respect to the ground state. (For more subspaces with different excitation-energy, refer Appendix A.1.) Fig. 4.6 shows one such excitation; in this case, one electron with spin $\downarrow$ is removed from the $p = -3$ level and one electron with spin $\downarrow$ is added to the $p = 1$ level. The impurity level is assumed to be filled with an electron with spin $\uparrow$, so the resulting state has $Q = 0$ and $S_z = +1/2$. In total, there are 32 states with excitation energy $\epsilon_1 + \epsilon_3$. These states can be classified using the quantum numbers Q, S, and S_z.

Here we consider only the states with quantum numbers $Q = 0$, $S = 1/2$, and $S_z = 1/2$ (with excitation energy $\epsilon_1+\epsilon_3$) which form a four-dimensional subspace. As the state shown in figure 4.6 is not an eigenstate of the total spin S, we have to form proper linear combinations to obtain a basis for this subspace; this basis can be written in the form

$$\begin{aligned}
|\psi_3\rangle &= \frac{1}{\sqrt{2}} f^\dagger_\uparrow (\xi^\dagger_{1\uparrow}\xi_{-3\uparrow} + \xi^\dagger_{1\downarrow}\xi_{-3\downarrow})|\psi_0\rangle \\
|\psi_4\rangle &= \frac{1}{\sqrt{6}} f^\dagger_\uparrow (\xi^\dagger_{1\uparrow}\xi_{-3\uparrow} - \xi^\dagger_{1\downarrow}\xi_{-3\downarrow})|\psi_0\rangle + \frac{2}{\sqrt{6}} f^\dagger_\downarrow \xi^\dagger_{1\uparrow}\xi_{-3\downarrow}|\psi_0\rangle \\
|\psi_5\rangle &= \frac{1}{\sqrt{2}} f^\dagger_\uparrow (\xi^\dagger_{3\uparrow}\xi_{-1\uparrow} + \xi^\dagger_{3\downarrow}\xi_{-1\downarrow})|\psi_0\rangle \\
|\psi_6\rangle &= \frac{1}{\sqrt{6}} f^\dagger_\uparrow (\xi^\dagger_{3\uparrow}\xi_{-1\uparrow} - \xi^\dagger_{3\downarrow}\xi_{-1\downarrow})|\psi_0\rangle + \frac{2}{\sqrt{6}} f^\dagger_\downarrow \xi^\dagger_{3\uparrow}\xi_{-1\downarrow}|\psi_0\rangle
\end{aligned} \tag{4.25}$$

where the state $|\psi_0\rangle$ is given by the product of the ground state of the conduction

electron chain and the empty impurity level:

$$|\psi_0\rangle = |0\rangle_{imp} \otimes \big[\prod_{p<0} \xi^\dagger_{p\uparrow}\xi^\dagger_{p\downarrow}|0\rangle_{cond}\big]. \tag{4.26}$$

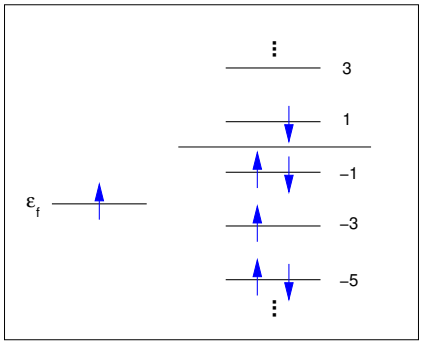

Figure 4.6: One possible excitation with energy $\epsilon_1+\epsilon_3$ and quantum numbers $Q=0$ and $S_z=+1/2$.

The fourfold degeneracy of the subspace $(Q=0, S=1/2, S_z=1/2)$ of the LM fixed point at energy $\epsilon_1+\epsilon_2$ is partially split for finite r in the spectrum of the quantum critical fixed point. Let us now calculate the influence of the perturbation H'_N on the states $|\psi_1\rangle, \cdots, |\psi_4\rangle$, concentrating on the splitting of the energy levels up to first order. Degenerate perturbation theory requires the calculation of the matrix

$$W_{ij} = \langle\psi_i|H'_N|\psi_j\rangle, \quad i,j=1,...,4, \tag{4.27}$$

and a subsequent calculation of the eigenvalues of $\{W_{ij}\}$ gives the level splitting.

Details of the calculation of the matrix elements W_{ij} are given in Appendix A.2. The result is

$$\{W_{ij}\} = \alpha(r)f(N)\begin{bmatrix} 0 & \frac{\sqrt{3}}{4}\gamma & 0 & 0 \\ \frac{\sqrt{3}}{4}\gamma & -\frac{1}{2}\beta & 0 & 0 \\ 0 & 0 & 0 & \frac{\sqrt{3}}{4}\gamma \\ 0 & 0 & \frac{\sqrt{3}}{4}\gamma & -\frac{1}{2}\beta \end{bmatrix}, \tag{4.28}$$

with $\gamma = [|\alpha_{01}|^2 - |\alpha_{0-3}|^2]$ and $\beta = [|\alpha_{01}|^2 + |\alpha_{0-3}|^2]$. The N-dependence of the coefficients α_{0p} [which relate the operators $c_{0\sigma}$ and $\xi_{p\sigma}$, see Eq. (A.50)] is given by

$$|\alpha_{0p}|^2 \propto \Lambda^{-Nr/2}\Lambda^{-N/2}, \tag{4.29}$$

; see also Sec. III A in Ref. (Gonzalez-Buxton and Ingersent 1998). Numerically we find that

$$\begin{aligned} \gamma &= -0.1478 \cdot \Lambda^{-Nr/2} \Lambda^{-N/2} \\ \beta &= 2.0249 \cdot \Lambda^{-Nr/2} \Lambda^{-N/2} \ , \end{aligned}$$

where the prefactors depend on the exponent r and the discretization parameter Λ (the quoted values are for $r = 0.01$ and $\Lambda = 2.0$). The matrix $\{W_{ij}\}_{r=0.01}$ then takes the form

$$\begin{aligned} \{W_{ij}\}_{r=0.01} &= \alpha(r = 0.01)\, \Lambda^{-N/2} \\ &\times \begin{bmatrix} 0 & -0.064 & 0 & 0 \\ -0.064 & -1.013 & 0 & 0 \\ 0 & 0 & 0 & -0.064 \\ 0 & 0 & -0.064 & -1.013 \end{bmatrix} . \end{aligned} \tag{4.30}$$

Diagonalization of this matrix gives the first-order corrections to the energy levels

$$\begin{aligned} \Delta E_1(r = 0.01) &= \Delta E_3(r = 0.01) \\ &= \alpha(r = 0.01)\, \Lambda^{-N/2} \cdot (-1.0615) \\ \Delta E_2(r = 0.01) &= \Delta E_4(r = 0.01) \\ &= \alpha(r = 0.01)\, \Lambda^{-N/2} \cdot 0.0004 \end{aligned} \tag{4.31}$$

with

$$E_{N,\mathrm{QCP}}(r = 0.01, i) = E_{N,\mathrm{LM}}(r = 0.01, i) + \Delta E_i(r = 0.01) \ , \tag{4.32}$$

($i = 1, \ldots 4$). Apparently, the fourfold degeneracy of the subspace ($Q = 0$, $S = 1/2$, $S_z = 1/2$) with energy $\epsilon_1 + \epsilon_3$ is split in two levels which are both twofold degenerate.

We repeated this analysis for a couple of other subspaces and a list of the resulting matrices $\{W_{ij}\}$ and the energy shifts ΔE is given in Appendix A.2.

Let us now proceed with the comparison of the perturbative results with the structure of the quantum critical fixed point calculated from the NRG. For our specific choice of the conduction band density of states, the relation (4.23) yields $\alpha(r) = \alpha\, r\, D$ for small r (where $\mu^r \approx 1$). Using the corresponding equations for the energy shifts, in Appendix A.2, we observe that a *single* parameter α must be sufficient to describe the level shifts in *all* subspaces, provided that the exponent r is small enough so that the perturbative calculations are still valid. A numerical fit gives $\alpha \approx 1.03$ for $\Lambda = 2.0$, (the Λ-dependence of α is discussed later, see Fig. 4.8).

Figure 4.7 summarizes the NRG results together with the perturbative analysis for exponents r close to 0. A flow diagram of the lowest lying energy levels is shown in Fig. 4.7-(a) for a small value of the exponent, $r = 0.03$, so that the levels

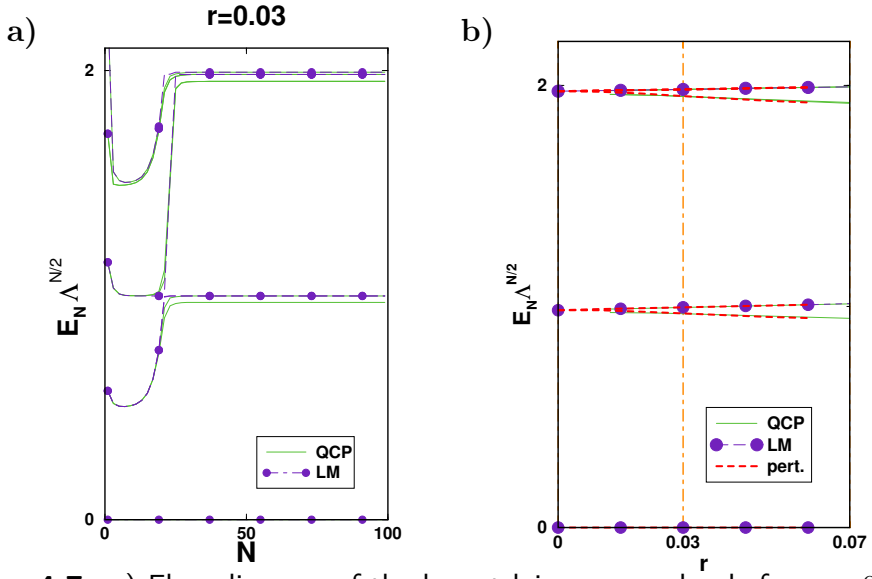

Figure 4.7: a) Flow diagram of the lowest lying energy levels for $r = 0.03$; dashed lines: flow to the LM fixed point; solid lines: flow to the quantum critical fixed point. b) The deviation of the QCP levels from the LM levels increases linearly with r. This deviation together with the splitting of the energy levels can be explained by the perturbative calculation (crosses) as described in the text.

of the QCP only slightly deviate from those of the LM fixed point. As discussed above, the deviation of the QCP levels from the LM levels increases linearly with r, see Fig. 4.7-(b). We indeed get a very good agreement between the perturbative result (crosses) and the NRG-data (lines) for exponents up to $r \approx 0.07$. The data shown here are for the subspaces ($Q = 0$, $S = 1/2$, $S_z = 1/2$) and energy $2\epsilon_1$ (the levels at $E_N\Lambda^{N/2} \approx 1$, see Appendix A.2.1) and ($Q = 0$, $S = 1/2$, $S_z = 1/2$) and energy $\epsilon_1 + \epsilon_3$ (the levels at $E_N\Lambda^{N/2} \approx 2$, see the example discussed in this section).

In the NRG, the continuum limit corresponds to the limit $\Lambda \to 1$, but due to the drastically increasing numerical effort upon reducing Λ, results for the continuum limit have to be obtained via extrapolation of NRG data for Λ in, for example, the range $1.5 < \Lambda < 3.0$. Figure 4.8 shows the numerical results from the NRG calculation together with a linear fit to the data: $\alpha(\Lambda) = 0.985 + 0.045(\Lambda - 1.0)$. Taking into account the increasing error bars for smaller values of Λ, the extrapolated value $\alpha(\Lambda \to 1) = 0.985$ is in excellent agreement with the result from the perturbative RG calculation, which is directly for the continuum limit and gives $\alpha = 1.0$.

4.3.2 Perturbation theory close to $r = 1/2$

To describe the deviation of the QCP levels from the SC levels close to $r = 1/2$, we have to start from an effective description of the SC fixed point. This is

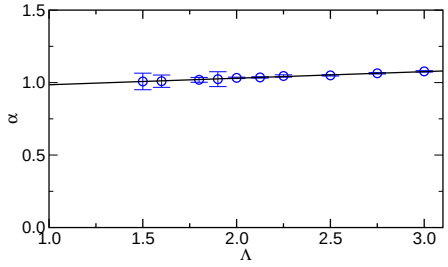

Figure 4.8: Dependence of the coupling parameter α on the NRG-discretization parameter Λ. The circles correspond to the NRG data and the solid line is a linear fit to the data: $\alpha(\Lambda) = 0.985 + 0.045(\Lambda - 1.0)$.

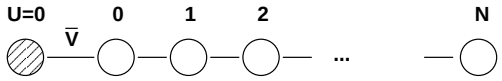

Figure 4.9: The spectrum of the SC fixed point is described by the non-interacting impurity coupled to the free conduction electron chain.

given by a finite chain *including* the impurity site with the Coulomb repulsion $U = 0$ at the impurity site and a hybridization $\bar{V}$ between impurity and the first conduction electron site, see Fig. 4.9.

Note that the SC fixed point can also be described by the limit $\bar{V} \to \infty$ and finite U which means that impurity and first conduction electron site are removed from the chain. This reduces the number of sites of the chain by two and leads to exactly the same level structure as including the impurity with $U = 0$. However, the description with the impurity included (and $U = 0$) is more suitable for the following analysis.

The corresponding effective Hamiltonian is that of a soft-gap Anderson model on a finite chain with $N+2$ sites and $\varepsilon_f = U = 0$ (i.e., a p-h symmetric resonant level model).

$$H_{\mathrm{sc},N} = \bar{V} \sum_{\sigma} \left[f_\sigma^\dagger c_{0\sigma} + c_{0\sigma}^\dagger f_\sigma \right] + H_{\mathrm{c},N} \ , \tag{4.33}$$

with $H_{\mathrm{c},N}$ as in Eq. (4.18).

As for the effective description of the LM fixed point, the effective Hamiltonian is that of a free chain. Focussing, as above, on odd values of N, the total number of sites of this chain, $N+2$, is odd. The single-particle spectrum of the free chain with an odd number of sites, corresponding to the diagonalized Hamiltonian

$$\bar{H}_{\mathrm{sc},N} = \sum_{\sigma l} \epsilon_l \, \xi_{l\sigma}^\dagger \xi_{l\sigma} \ , \tag{4.34}$$

is sketched in Fig. 4.10.

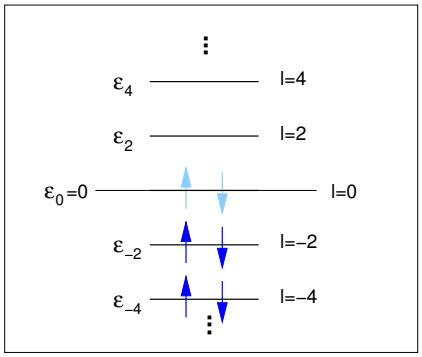

Figure 4.10: Single-particle spectrum of the free conduction electron chain Eq. (4.34). The ground state is fourfold degenerate with all the levels with $l < 0$ filled and the level $l = 0$ either empty, singly ($\uparrow$ or $\downarrow$) or doubly occupied.

As we assume p-h symmetry, the positions of the single-particle levels are symmetric with respect to 0 with

$$\epsilon_0 = 0 \quad , \quad \epsilon_l = -\epsilon_{-l} \quad , \quad l = 2, 4, \ldots, (N+1) \; , \tag{4.35}$$

and

$$\sum_l \equiv \sum_{l=-(N+1),\; l \text{ even}}^{l=N+1} \; . \tag{4.36}$$

The ground state of the effective model for the SC fixed point is fourfold degenerate, with all levels with $l < 0$ filled and the level $l = 0$ either empty, singly ($\uparrow$ or $\downarrow$) or doubly occupied.

According to Section 4.2 the proper perturbation to access the critical fixed point from the SC one is an on-site repulsion, thus we choose

$$H'_N = \beta(r)\bar{f}(N)(n_{f\uparrow} - \frac{1}{2})(n_{f\downarrow} - \frac{1}{2}), \tag{4.37}$$

($n_{f\sigma} = f^\dagger_\sigma f_\sigma$) with the strength of the perturbation parameterized as

$$\beta(r) = \mu^{2r-1}\rho_0^2\bar{V}^4\beta\sqrt{1/2 - r}; \tag{4.38}$$

see Section 4.2. Note that $\rho_0^2(r = 1/2) = 9/(2D^3)$ for a featureless power-law density of states with bandwidth D. The N dependence of the operator $(n_{f\uparrow} - \frac{1}{2})(n_{f\downarrow} - \frac{1}{2})$ is given by $\Lambda^{(r-1/2)N}\Lambda^{-N/2} = \Lambda^{(r-1)N}$, so we have to choose

$$\bar{f}(N) = \Lambda^{(1/2-r)N}. \tag{4.39}$$

This again follows from the scaling analysis of Section 4.2: the on-site repulsion has scaling dimension $\dim[U] = 2r - 1$. Thus the $(\sum_\sigma f^\dagger_\sigma f_\sigma - 1)^2$ term in H'_N in

Eq. (4.37) scales as $\Lambda^{N(r-1/2)}$, and $\bar{f}(N)$ in Eq. (4.39) compensates this behavior to make H'_N exactly marginal.

The matrix $W_{ij} = \langle\psi_i|H'_N|\psi_j\rangle$ $(i,j=1,2)$ is given by

$$\{W_{ij}\} = \beta(r)\bar{f}(N)|\alpha_{f2}|^4 \begin{bmatrix} 2-2\kappa+\kappa^2 & 2\sqrt{2}\kappa \\ 2\sqrt{2}\kappa & 2+\kappa^2 \end{bmatrix} , \tag{4.40}$$

with $\kappa = |\alpha_{f0}|^2/|\alpha_{f2}|^2$. The N-dependence of the coefficients $|\alpha_{fl}|$ [which relate the operators f_μ and $\xi_{l\mu}$, see Eq. (A.73).] is given by

$$|\alpha_{fl}|^2 \propto \Lambda^{(r-1)N/2} , \tag{4.41}$$

Numerically we find that

$$\begin{aligned} |\alpha_{f2}|^2 &= 0.1462 \cdot (D/\bar{V})^2 \Lambda^{(r-1)N/2} \\ |\alpha_{f0}|^2 &= 0.3720 \cdot (D/\bar{V})^2 \Lambda^{(r-1)N/2} , \end{aligned}$$

where the prefactors depend on the exponent r and the quoted value is for $r = 0.499$. The matrix $\{W_{ij}\}_{r=0.499}$ then takes the form

$$\{W_{ij}\}_{r=0.499} = \beta(r=0.499)(D/\bar{V})^4 \Lambda^{-N/2} \begin{bmatrix} 0.07 & 0.15 \\ 0.15 & 0.18 \end{bmatrix} , \tag{4.42}$$

Diagonalization of this matrix gives the first-order corrections to the energy levels

$$\begin{aligned} \Delta E_1(r=0.499) &= \beta(r=0.499)(D/\bar{V})^4 \, \Lambda^{-N/2} \cdot (-0.036) \\ \Delta E_2(r=0.499) &= \beta(r=0.499)(D/\bar{V})^4 \, \Lambda^{-N/2} \cdot (0.290) \end{aligned} \tag{4.43}$$

with

$$E_{N,\mathrm{QCP}}(r=0.499,i) = E_{N,\mathrm{SC}}(r=0.499,i) + \Delta E_i(r=0.499) , \tag{4.44}$$

$(i=1,2)$. We repeated this analysis for a couple of other subspaces and a list of the resulting matrices $\{W_{ij}\}$ and the energy shifts ΔE is given in Appendix A.3.

The comparison of the perturbative results with the numerical results from the NRG calculation is shown in Fig. 4.11-(b). As for the case $r \approx 0$ we observe that a single parameter β is sufficient to describe the level shifts in all subspaces, provided the exponent r is close enough to $r = 1/2$ so that the perturbative calculations are valid. For $\Lambda = 2.0$ we find $\beta \approx 9.8$ and the $\Lambda \to 1$ extrapolation results in $\beta(\Lambda \to 1) \approx 9.8 \pm 0.5$ (the error bars are significantly larger as for the extrapolation of the coupling α). The results from perturbative RG, Section 4.2, specifically Eq. (4.13) and Eq. (4.14), yield $\beta(r) = \mu^{2r-1}\rho_0^2\bar{V}^4\, 2\pi^2 u^*$. This gives $\beta = 83.3$.

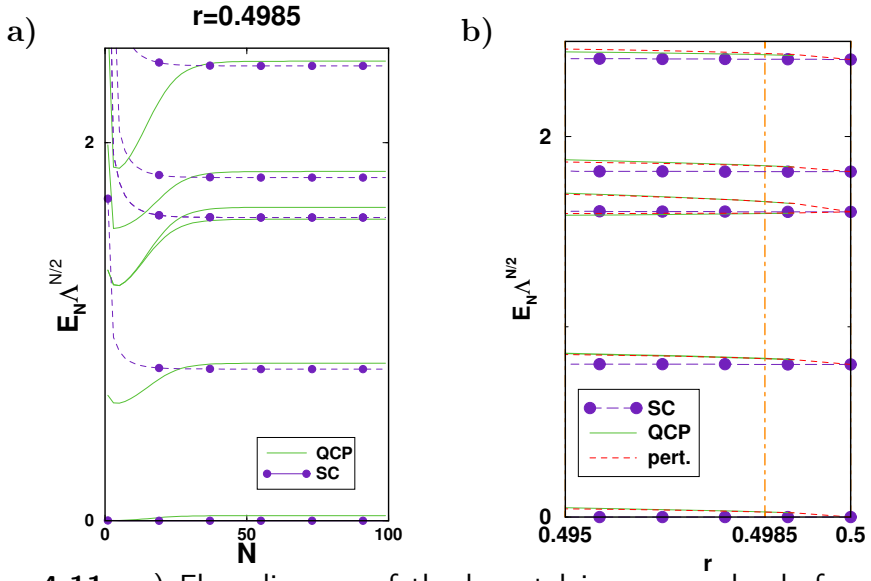

Figure 4.11: a) Flow diagram of the lowest lying energy levels for $r = 0.4985$; dashed lines: flow to the SC fixed point; solid lines: flow to the quantum critical fixed point. b) The deviation of the QCP levels from the SC levels is proportional to $\sqrt{1/2 - r}$. This deviation together with the splitting of the energy levels can be explained by the perturbative calculation (crosses) as described in the text.

Similar to Fig. 4.7 above, we show in Fig. 4.11-(a) a flow diagram for an exponent very close to 1/2, $r = 0.4985$, so that the levels of the QCP only slightly deviate from those of the SC levels. As discussed above, this deviation is proportional to $\sqrt{1/2 - r}$, see Fig. 4.11-(b). The data shown here are all for subspaces with ($Q = -1$, $S = 0$, $S_z = 0$); the unperturbed energies E of these subspaces are:

- $E = 0$: the levels at $E_N \Lambda^{N/2} \approx 0$, see Appendix A.3.2,
- $E = \epsilon_2$: the levels at $E_N \Lambda^{N/2} \approx 0.8$, see Appendix A.3.3,
- $E = 2\epsilon_2$: the levels at $E_N \Lambda^{N/2} \approx 1.6$, see the example discussed in this section,
- $E = \epsilon_4$: the levels at $E_N \Lambda^{N/2} \approx 1.8$, see Appendix A.3.4,
- $E = 3\epsilon_2$: the levels at $E_N \Lambda^{N/2} \approx 2.4$.

We again find a very good agreement between the perturbative results (crosses) and the NRG data (lines).

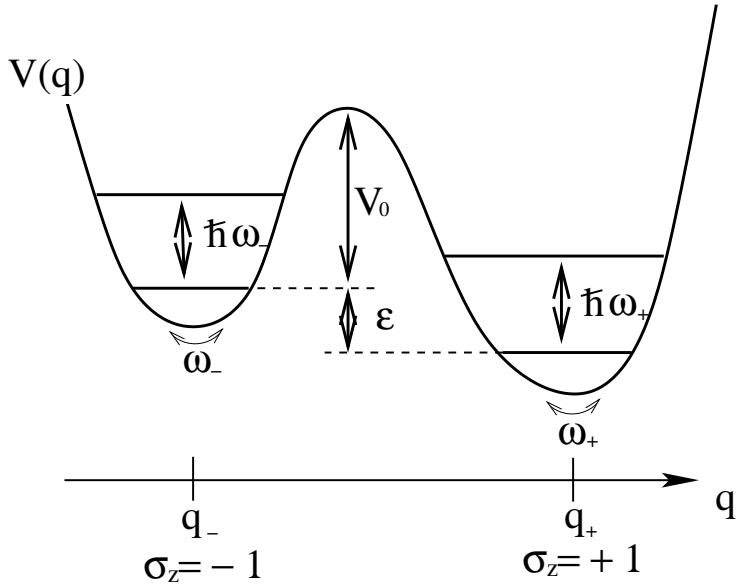

Figure 5.1: A double-well system in the "two-state" limit.

5. SPIN-BOSON MODEL

5.1 Introduction

The spin-boson model (Leggett et al. 1987) is a generic model describing quantum dissipation. The Hamiltonian is given by

$$H = -\frac{\Delta}{2}\sigma_x + \frac{\varepsilon}{2}\sigma_z + \sum_i \omega_i a_i^\dagger a_i + \frac{\sigma_z}{2}\sum_i \lambda_i (a_i + a_i^\dagger). \tag{5.1}$$

Here the Pauli matrices σ_j describe a spin, i.e., a generic two-level systems, which possesses a degree of freedom that can take only two values. As simple examples, the spin projection in the case of a nucleus of spin 1/2, the strangeness in the case of a neutral K meson, or the polarization in the case of photon correspond the intrinsic case.

A more common situation for the two-level system is that the system in question has continuous degree of freedom q, for example, a geometrical coordinate, with which a potential energy function $V(q)$ is associated with two separate minima, as illustrated in Fig. 5.1. Suppose that the barrier height V_0 is large

compared to the quantities $\hbar\omega_+$ and $\hbar\omega_-$, where $\hbar\omega_+$ and $\hbar\omega_-$ are the separation of the first excited state (of each "isolated" well) from the ground state. If, moreover, the bias ("detuning") ε between the ground states in the two wells is small compared to $\omega_\pm$, then the system could be effectively restricted to the two-dimensional Hilbert space spanned by these two ground states.

Now we take into account the possibility of tunneling between two wells, with the tunneling matrix elements $\hbar\Delta$ for this process in the limit,

$$\hbar\Delta \ll \hbar\omega_\pm \ll V_0, \tag{5.2}$$

so that the tunneling does not mix the states of this "ground" two dimensional Hilbert space with the excited states of the system.

Then, the motion of the isolated two-state system in the two dimensional Hilbert space can be described by

$$H_{imp} = -\frac{\Delta}{2}\sigma_x + \frac{\varepsilon}{2}\sigma_z, \tag{5.3}$$

where the σ_i $(i = 1, 2, 3)$ are Pauli matrices, and the basis is chosen so that the eigenstate of σ_z with eigenvalue $+1$ (-1) corresponds to the systems being localized in the right(left) well.

The next term in Eq. (5.1) corresponds to the environment which consists of infinitely many harmonic oscillators,

$$H_{bath} = \sum_i \omega_i a_i^\dagger a_i, \tag{5.4}$$

each of which couples to the two-state system through a term of the form

$$H_{coupling} = \frac{\sigma_z}{2}\sum_i \lambda_i (a_i + a_i^\dagger).^{1} \tag{5.5}$$

As an example, we consider a two-level system interacting with laser in the vacuum field.[2] A coupling of the form in Eq. (5.5) means that the light is sensitive to the value of σ_z, in other words, that the light can observe the value of σ_z (i.e., whether the system is in the right or left well)

The laser itself cannot be considered as a bath as long as it makes a perfect coherent photon with a single frequency ω. However the spontaneous emission

[1] In Eq. (5.3), Eq. (5.4) and Eq. (5.5), $\hbar$ is set to 1.

[2] The spin-boson model has found applications in a wide variety of physical situations: (Leggett et al. 1987, Weiss 1999) mechanical friction, damping in electric circuits, decoherence of quantum oscillations in qubits (Costi and McKenzie 2003, Khveshchenko 2004, Thorwart and Hänggi 2002), impurity moments coupled to bulk magnetic fluctuations (Sachdev 1999, Castro Neto, Novais, Borda, Zaránd and Affleck 2003), atomic quantum dots coupled to a reservoir of a superfluid Bose-Einstein condensate (Recati, Fedichev, Zwerger, von Delft and Zoller 2005), and electron transfer in biological molecules (Garg, Onuchic and Ambegaokar 1985, Mühlbacher and Egger 2003).

into the vacuum field creates photons with random direction, polarization and the energy so that the laser in the vacuum field should be considered as an incoherent and dissipative bosonic bath of Eq. (5.4) rather than a coherent light source of a simple harmonic oscillator $\omega\ a^{\dagger}a$.[3]

In that case, the complete information about the effect of the bath can be encapsulated in a single spectral function $J(\omega)$, defined by the expression

$$J(\omega) = \pi \sum_i \lambda_i^2 \delta(\omega - \omega_i). \tag{5.6}$$

It is highly non-trivial to predict the time-evolution of the phase of the two-level system,

$$P(t) = \langle \sigma_z(t) \rangle, \tag{5.7}$$

in the presence of incoherent and dissipating media H_{bath}.

The focus of the investigation on the spin-boson model, therefore, has been to calculate $P(t)$ for various types of baths, in particular, of which $J(\omega)$ is assumed to have a simple power-law behavior. With the standard parametrization,

$$J(\omega) = 2\pi\alpha\omega_c^{1-s}\omega^s, \quad , 0 < \omega < \omega_c, \quad s < -1 \tag{5.8}$$

where the dimensionless parameter α characterizes the dissipation strength, and ω_c is a cutoff energy.

The case $s = 1$ is known as ohmic dissipation, where the spin-boson model has a delocalized and a localized zero-temperature phase, separated by a Kosterlitz-Thouless transition (for the unbiased case of $\varepsilon = 0$). In the delocalized phase, realized at a small dissipation strength α ($\alpha < 1$), the ground state is non-degenerate and represents a (damped) tunneling particle. For large α ($\alpha > 1$), the dissipation leads to a localization of the particle in one of the two σ_z-eigenstates, thus the ground state is doubly degenerate. $P(t)$ shows rather subtle changes according to the dissipation strength α and temperature.[4]

For the sub-ohmic case ($0 < s < 1$), it was found that the system is localized at zero temperature in the well it started in. The NRG approach, however, for the spin-boson model found that there are also quantum phase transitions and the transition line shows quantum critical behaviors (Bulla et al. 2003). Following sections are devoted exactly to these issues.

5.2 Quantum phase transitions in the sub-ohmic Spin-Boson model

Precedent works on the sub-ohmic spin-boson model, in most of which $\Delta/\omega_c \to 0$ limit is assumed, report that a particle in the two-level system is localized in the

[3] As an example of the latter case, a single-impurity Anderson model with a linear coupling to a local phonon model was studied in (Hewson and Meyer 2002, Meyer, Hewson and Bulla 2002).

[4] For details, see e.g., (Leggett et al. 1987).

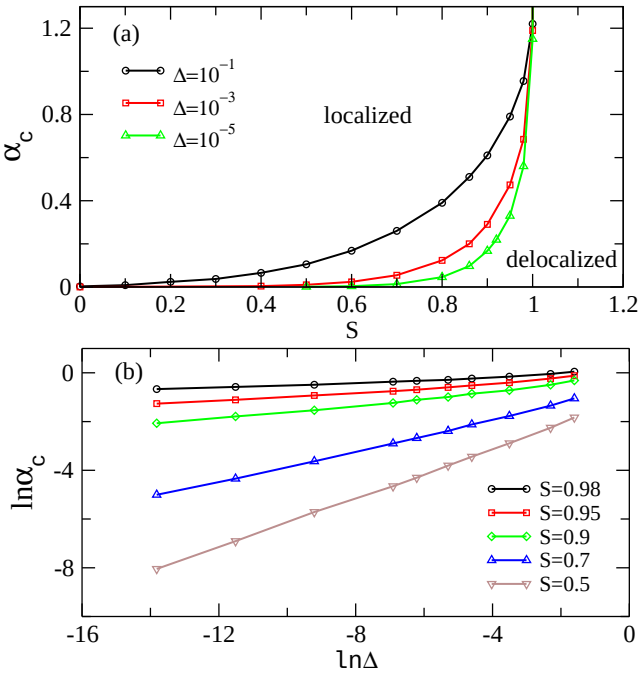

Figure 5.2: (a) Phase diagram for the transition between delocalized($\alpha < \alpha_c$) and localized phases($\alpha > \alpha_c$) of the spin-boson model 5.1 for bias $\varepsilon = 0$ and various values of Δ, deduced from the NRG flow. (b) Δ dependence of the critical coupling α_c for various values of the bath exponent s. For s close to 1 the asymptotic regimes is reached only for very small Δ. NRG parameters here are $\Lambda = 2, N_b = 8$, and $N_s = 100$.

well it started in for any nonzero coupling to the bath. However the argument for localization becomes subtle when the two limits $(\alpha\omega_c)/\omega_c \to 0$ and $\Delta/\omega_c \to 0$ are considered simultaneously. In the case, the relative scale of $\alpha\omega_c$ to Δ might be important but comparison of the bare energy scale is not sufficient to explain the low temperature behavior, for which more knowledge is required on how the two parameters α and Δ are renormalized with decreasing temperature and which one is dominant in the zero temperature limit.

The NRG calculation has been performed to answer these questions and found a continuous (2nd order) transition with associated critical behavior for the range $0 < s < 1$.

In this approach, the frequency range of the bath spectral function $[0, \omega_c]$ is divided into intervals $\left[\omega_c\Lambda^{-(n+1)}, \omega_c\Lambda^{-n}\right]$, $n = 0, 1, 2, ...$, with Λ the NRG dis-

cretization parameter. The continuous spectral function within these intervals is approximated by a single bosonic state and the resulting discretized model is then mapped onto a semi-infinite chain with the Hamiltonian

$$\begin{aligned} H &= -\frac{\Delta}{2}\sigma_x + \frac{\varepsilon}{2}\sigma_z + \sqrt{\frac{\eta_0}{\pi}}\frac{\sigma_z}{2}(b_0 + b_0^\dagger) + \sum_{n=0}^{\infty}\varepsilon_n b_n^\dagger b_n \\ &+ \sum_{n=0}^{\infty} t_n(b_n^\dagger b_{n+1} + b_{n+1}^\dagger b_n), \end{aligned} \tag{5.9}$$

with

$$\eta_0 = \int_0^{\omega_c} d\omega J(\omega) = 2\pi\alpha\omega_c^{1-s}\int_0^{\omega_c} d\omega\ \omega^s. \tag{5.10}$$

Figure 5.2-(a) shows the zero temperature phase diagram, where the phase boundaries are determined from the NRG flow for fixed NRG parameters $\Lambda = 2$, $N_b = 8$, and $N_s = 100$ (Bulla et al. 2003). As displayed in Fig. 5.2-(b), the critical coupling α_c closely follows a power law as a function of the bare tunnel splitting, $\alpha_c \propto \Delta^x$ for small $\Delta(<< \omega_c)$, with an s-dependent exponent x. The data are consistent with $x = 1 - s$.

The character of each fixed point is described by the two renormalized parameters Δ_r and α_r.[5] At the localized and delocalized fixed points, one of the two parameters is far dominant to the other and the system is driven by the former one only. The delocalized fixed point can be effectively described by putting $\Delta_r \neq 0$ and $\alpha_r = 0$ in the Hamiltonian (5.9). The localized phase is the other way around ($\Delta_r = 0$ and $\alpha_r \neq 0$). At the quantum critical points, all renormalized parameters Δ_r and α_r are similar in the order of magnitude so that none of them are to be disregarded.

We describe the physics of the three fixed points through the NRG flow-diagram and the thermodynamic quantities in the following sections.

5.2.1 Localized/Delocalized fixed points

At the localized fixed points ($\alpha_r \neq 0$ and $\Delta_r = 0$),[6] the dynamics of the two-level system, oscillations(or tunneling) between two levels, is suppressed by the bosonic bath with strong energy-dissipation. The effective Hamiltonian is

$$H_L = \sqrt{\frac{\eta_0}{\pi}}\frac{\sigma_z}{2}(b_0 + b_0^\dagger) + \sum_{n=0}^{\infty}\varepsilon_n b_n^\dagger b_n + \sum_{n=0}^{\infty} t_n(b_n^\dagger b_{n+1} + b_{n+1}^\dagger b_n), \tag{5.11}$$

[5] We consider the case of zero-bias $\varepsilon = 0$.

[6] In the language of the (perturbative) renormalized group (Leggett et al. 1987, Anderson, Yuval and Hamann 1970) the localized phase corresponds to the *line* of fixed points, parameterized by α although the fixed-point value α does not influence the eigenenergies of the many-body Hamiltonian, but only its eigenstates.

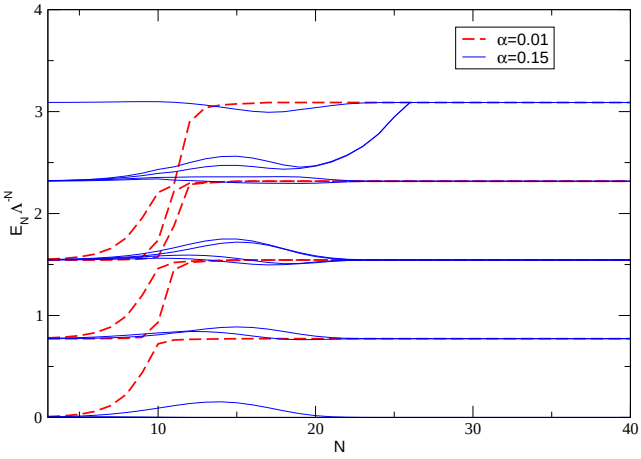

Figure 5.3: Flow diagram of the lowest lying many-particle energies calculated with the star-NRG for the sub-Ohmic case($s = 0.8, \Delta = 0.001$), using displaced oscillators as optimized basis. The critical value is $\alpha_c = 0.125$. The NRG parameters are $N_s = 60$, $N_b = 6$, and $\Lambda = 2$

which yields the same structure of the NRG-spectrum as the one of the bosonic bath except that there are additional two-fold degeneracies due to the two-level system. According to the precedent works (Leggett et al. 1987), this is the only stable fixed point in the sub-ohmic spin-boson model.

The NRG approach, however, found regions in the parameter-space where the stable fixed point is replaced by the delocalized one ($\alpha_r = 0$ and $\Delta_r \neq 0$). The effective Hamiltonian for the delocalized fixed point is

$$H_D = -\frac{\Delta}{2}\sigma_x + \sum_{n=0}^{\infty} \varepsilon_n b_n^\dagger b_n + \sum_{n=0}^{\infty} t_n (b_n^\dagger b_{n+1} + b_{n+1}^\dagger b_n). \tag{5.12}$$

The delocalized fixed points appear for values of s in the range $0 < s < 1$ and the coupling strength $\alpha < \alpha_c$.

The structure of the low-lying spectrum at the delocalized fixed point is same as that at the localized one apart from the absence of the two-fold degeneracy. Figure 5.3 show the lowest lying many-particle energies calculated with the star-NRG[7] for the sub-ohmic case ($s = 0.8, \Delta = 0.001$), using displaced oscillators as optimized basis. Solid and dashed lines corresponds to the result for $\alpha = 0.01$ ($< \alpha_c$: delocalized) and $\alpha = 0.15$ ($> \alpha_c$: localized), from which we can see the

[7] See the chapter II in Ref. (Bulla et al. 2005)

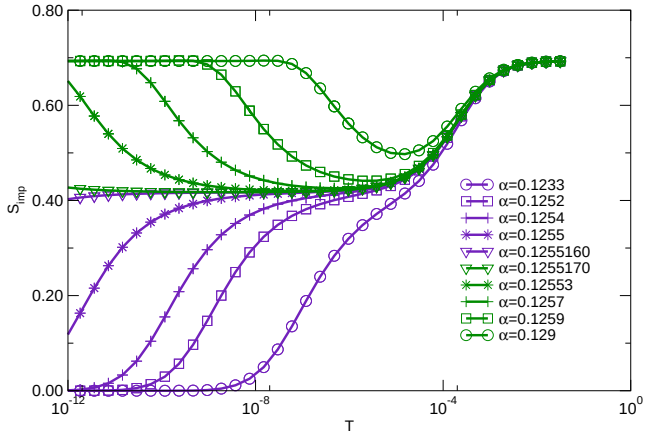

Figure 5.4: Temperature dependence of the impurity contribution to the entropy, $S_{imp}(T)$, in the sub-ohmic case ($s = 0.8$) for various values of α.

degeneracy of the localized fixed point is exactly twice as many as that of the delocalized one.

Figure 5.4 shows temperature dependence of the impurity contribution to the entropy $S_{imp}(T)$ for $s = 0.8$ and various values of α. Comparing the residual entropy of the two different cases, $\alpha = 0.1233$ ($< \alpha_c$:delocalized) and $\alpha = 0.1290$ ($> \alpha_c$:localized), we observe the $\ln 2$ (≈ 0.69) difference as a consequence of the double degeneracy at the localized fixed point.[8]

At high temperature, the impurity contribution to the entropy takes a value of $\ln 2$ regardless of the coupling strength α, due to the fact that, for temperature $T \gg \Delta$, both states of the two-level system contribute equally to the thermodynamics. Therefore, the temperature-dependent entropy $S_{imp}(T)$ undergoes the $\ln 2$ differences as the system flows to the delocalized fixed point with $S_{imp} = 0$.

Quite a striking feature of negative slope in $S_{imp}(T)$ (negative specific heat) appears in the localized phase. The non-trivial effects becomes more prominent as the system approaches to the critical point $\alpha = \alpha_c$ where the impurity contri-

[8] The double degeneracy in the localized fixed points makes the partition function Z_L twice larger than Z_D. Thus, the difference in the impurity contribution of the entropy is given as

$$\begin{aligned} S^L_{imp} &= k_B \ln Z_L \\ &= k_B \ln(2Z_D) \\ &= k_B \ln 2 + k_B \ln Z_D \\ &= k_B \ln 2 + S^D_{imp} \end{aligned} \tag{5.13}$$

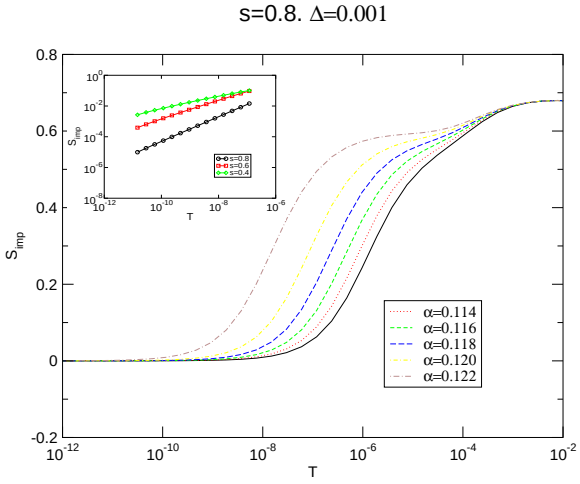

Figure 5.5: Temperature dependence of the impurity contribution to the entropy, $S_{imp}(T)$, in the sub-Ohmic case for various values of α and $s = 0.8$ (main panel) and various values of s (inset). The coupling α is below α_c so that the flow is to the delocalized phase for all parameters in this figure. Lines with symbols in the inset are data from the bosonic NRG and solid lines are fits assuming a power-law, $S_{imp}(T) \propto T^s$.

bution to the entropy is quenched to a value less than $\ln 2$ ($S_{imp} \approx 0.41$ in the Fig. 5.4). Furthermore, nice scaling behavior is observed in the crossover between the quantum critical phase and the localized/delocalized phase. We discuss the issues on the quantum criticality in a separate section.

5.2.2 Quantum critical fixed points

Figure 5.5 shows the temperature dependence of the impurity contribution to the entropy, $S_{imp}(T)$, in the sub-Ohmic case, $s = 0.8$, for various values of α below the critical value $\alpha_c \approx 0.125$.[9] For α close to α_c, we observe a two stage quenching of the entropy of the free moment (the quantum critical point has a nontrivial zero-point entropy of $S_{qcp}(T \to 0) \approx 0.6$ for $s = 0.8$). The temperature scale (T^*) for the crossover to the delocalized fixed point increases with the distance from

[9] The data in Fig.5.5 is calculated with the chain NRG. The results from the star-NRG look similar. (They give, in particular the correct values $S_{imp}(T \to 0) = \ln 2$ if the flow is to the localized phase.) We observe, however, a low temperature behavior for $S_{imp}(T)$ which is *different* from the correct form $S_{imp}(T) \propto T^s$. The reason for this failure is presently not clear but probably due to truncation errors.

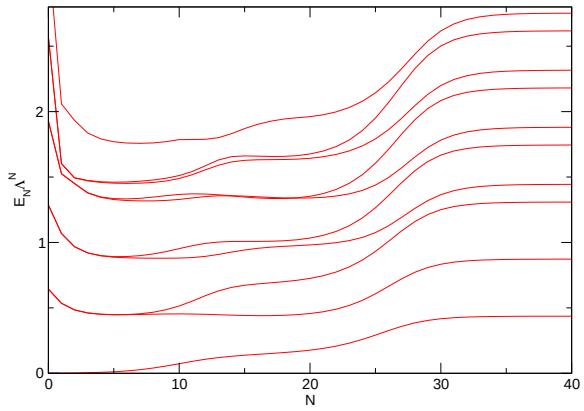

Figure 5.6: Flow diagram of the lowest lying many particle energies calculated with the chain-NRG for the sub-Ohmic case ($s = 0.8$, $\Delta = 0.001$ and $\alpha = 0.122$). The NRG parameters are $N_s = 100$, $N_b = 8$, and $\Lambda = 2.0$.

the critical point following the scaling relation (Bulla et al. 2005),

$$T^* \propto \Delta^{1/|\alpha-\alpha_c|}. \tag{5.14}$$

The low-temperature behavior of $S_{imp}(T)$ for $\alpha < \alpha_c$ is given by $S_{imp}(T) \propto T^s$ which can be seen more clearly in the inset of Fig. 5.5 where $S_{imp}(T)$ is plotted for various values of s. This behavior is in agreement with the calculations of Ref. (Göhrlich and Weiss 1998), where $C(T) \propto T^s$ was found for the slightly asymmetric ($\epsilon \neq 0$) sub-Ohmic spin-boson model.

Now we look into the quenched entropy at the critical point $\alpha = \alpha_c$.

$$S_{qcp}(T \to 0) \approx 0.6. \tag{5.15}$$

The absolute value (≈ 0.6) is still questionable in a sense that the value itself changes with the numerical conditions such as N_s and Λ. Nevertheless, we believe that the residual entropy at the critical point is different from the one at the localized and delocalized fixed point, since the structure of the low-lying spectrum at the quantum critical point is clearly distinguished from the other two cases.

Figure 5.6 shows the low-lying spectra corresponding to the curve "$\alpha = 0.122$" in Fig. 5.5. We see three stages of plateau in the spectra: the localized fixed point ($3 < N < 8$),[10] the quantum critical fixed point ($12 < N < 22$) and

[10] As briefly mentioned in the previous section, the vicinity to the localized fixed point for early iterations (which results in the high-temperature value $S_{imp}(T) \approx \ln 2$) does not imply localization. However, the structure of the low-lying spectrum and all the results out of the spectrum happen to be same as the ones in the localized case so that we use the same terminology for the case, too.

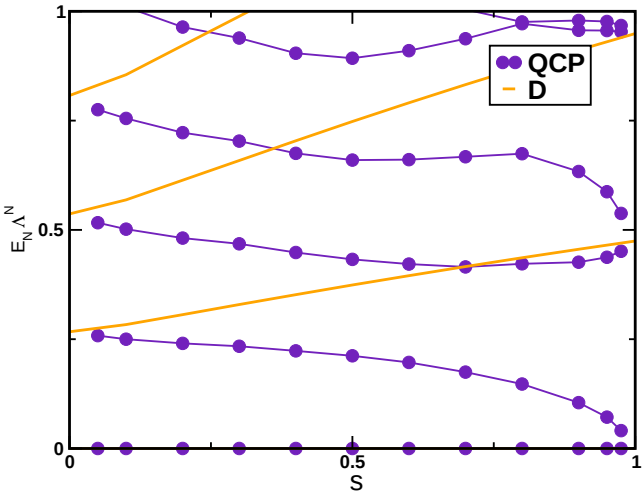

Figure 5.7: Dependence of the many-particle spectra for the two fixed points of the spin-boson model on the exponent s: D:delocalized fixed points(solid lines without symbol) and the quantum critical points(solid lines with circles).

the delocalized fixed point($N > 30$), which result in the three steps at $\ln 2, 0.6$ and zero in $S_{imp}(T)$. The quantum critical fixed point has obviously different structure from the others.

In Fig. 5.7, the many-particle spectra of the two fixed points, delocalized and quantum critical ones are plotted as functions of the exponent s. At $s = 0$ limit, many-particle levels of the quantum critical fixed point (solid lines with circles) coincide with the ones of the delocalized fixed point (solid lines without symbols). In the other limit, $s = 1$, the many-particle levels of the quantum critical point approaches toward the same delocalized fixed points in pairs. Thus, we can conclude that the levels of the quantum critical points, $E_{N,QCP}(s)$, approach the levels of the delocalized (localized) fixed points in the limit $s \to 0$ ($s \to 1$).

$$\begin{aligned} \lim_{s\to 0}\{E_{N,QCP}(s)\} &= \{E_{N,D}(s=0)\}, \\ \lim_{s\to 1}\{E_{N,QCP}(s)\} &= \{E_{N,L}(s=1)\}. \end{aligned} \tag{5.16}$$

The structure of the quantum critical fixed points shows continuous change from the delocalized fixed points ($s = 0$) to the localized fixed points ($s = 1$) with increasing s. Accordingly, the residual entropy at the quantum critical fixed point S_{crit} also has a continuous change from $S_{imp} = 0$ (delocalized) to $S_{imp} = \ln 2$ (localized) leading to the quenched entropy ($S_{crit} < \ln 2$) in between.

To search out the origin of the suppressed entropy at the critical point might require a similar analysis as we did for the soft-gap Anderson model: find proper

marginal operators at the quantum critical points and show how the subsystem (two-level system) fluctuates via the marginal interaction with the bath.

In the vicinity of the critical dimensions $s = 0$ and $s = 1$, the effects of marginal interaction is pretty weak such that the many-particle spectrum at the quantum critical points is perturbatively accessible within a single-particle picture. The explicit formation of the many-particle states will give intuitive knowledge on the quantum fluctuations represented by the quenched entropy $S_{crit} < \ln 2$.

6. BOSONIC SINGLE-IMPURITY ANDERSON MODEL

6.1 Introduction

The focus of this work is the physics of a bosonic impurity state coupled to a non-interacting bosonic environment modeled by the Hamiltonian

$$H = \varepsilon_0 b^\dagger b + \frac{1}{2} U b^\dagger b (b^\dagger b - 1) + \sum_k \varepsilon_k b_k^\dagger b_k + \sum_k V_k (b_k^\dagger b + b^\dagger b_k). \tag{6.1}$$

The energy of the impurity level (with operators $b^{(\dagger)}$) is given by ε_0; the parameter U is the local Coulomb repulsion acting on the bosons at the impurity site. The impurity couples to a bosonic bath via the hybridization V_k, with the bath degrees of freedom given by the operators $b_k^{(\dagger)}$ with energy ε_k.

Similar to other quantum impurity models, the influence of the bath on the impurity is completely specified by the bath spectral function

$$\Delta(\omega) = \pi \sum_k V_k^2 \delta(\omega - \varepsilon_k). \tag{6.2}$$

Here we assume that $\Delta(\omega)$ can be parameterized by a power-law for frequencies up to a cutoff ω_c. (We set $\omega_c = 1$ in the calculations.)

$$\Delta(\omega) = 2\pi\alpha\omega_c^{1-s}\omega^s, \ 0 < \omega < \omega_c. \tag{6.3}$$

The parameter α is the dimensionless coupling constant for the impurity-bath interaction.

We term the system defined by Eq. (6.1) the "bosonic single-impurity Anderson model" (bsiAm), in analogy to the standard (fermionic) siAm (Hewson 1993), which has a very similar structure except that all fermionic operators are replaced by bosonic ones. Furthermore, we do not consider internal degrees of freedom of the bosons, such as the spin (an essential ingredient in the fermionic siAm).

Our main interest of the bsiAm is the low-temperature behavior of Bose-Einstein condensation (BEC) and, possibly, quantum phase transitions from BEC to other phases. We raise several questions related to the issues, concerning the model in Eq. (6.1).

Q-1. Does BEC appear as a possible ground state of the bsiAm?

Q-2. Is the NRG able to capture features of BEC such as the critical temperature T_c and the BEC-gap Δ_{gap}?

Q-3. What are the effects of an impurity that involves correlations among the particles? Does it generate a new phase suppressing the BEC?

The NRG considers a non-interacting bosonic bath (gas) as a grand canonical system with a fixed chemical potential $\mu = 0$, where the bosonic bath itself shows BEC exactly at zero temperature.[1] However the BEC of ideal Bose gas (with fixed chemical potential $\mu = 0$) at zero temperature is not captured within the NRG approach since the contribution of the state at $\varepsilon = 0$[2] is neglected during the logarithmic discretization of the bosonic bath.

Although it looks a very critical defect that the NRG misses the ground state property of the reservoir, we can get around the drawback by bringing the impurity quantum phase transition into focus of interest. From the viewpoint of the impurity quantum phase transitions, the existence of a state $\varepsilon = \mu = 0$ becomes essential only if it takes a significant role to change the impurity contribution at the ground state. Here we examine the importance of the $\varepsilon = 0$ state in each phase.[3]

S-1. *The Mott phase*: As we will discuss in the later section, the low temperature behavior (the low lying spectrum) of the Mott phase can be understood as the one of ideal Bose gas in the presence of a frozen impurity. The existence of the $\varepsilon = \mu = 0$ state and the resulting BEC transition at $T = 0$ do not affect the configuration at the impurity-site since the impurity is completely decoupled from the continuum states of the bath.

S-2. *The BEC phase*: A system with negative chemical potential $\mu < 0$ enters the BEC phase below finite (non-zero) temperature T^* where the ground state with a condensate wave function is separated from the other excited ones by the BEC gap Δ_g. Condensation occurs exactly at the state sitting at the chemical potential $\varepsilon = \mu < 0$ and the effect of $\varepsilon = 0$ state is negligible.

S-3. *The quantum critical phase*: One of the non-trivial cases would be an interacting system with zero chemical potential $\mu = 0$, possibly a system at the critical point. In this case, the effect of the state at $\varepsilon = \mu = 0$ might be significant at all excited states including the ground state.

The first two statements tell that the properties of the Mott and the BEC phase are accessible to the NRG in spite of the drawback of discretization. Most of

[1] Details are discussed in the appendix C.

[2] In other words, the state sitting at the chemical potential $\mu = 0$.

[3] Here we briefly mention the contents of quantum phase transitions such as the Mott, BEC and the quantum critical phases without touching the details. Each phase will be treated in the separate sections.

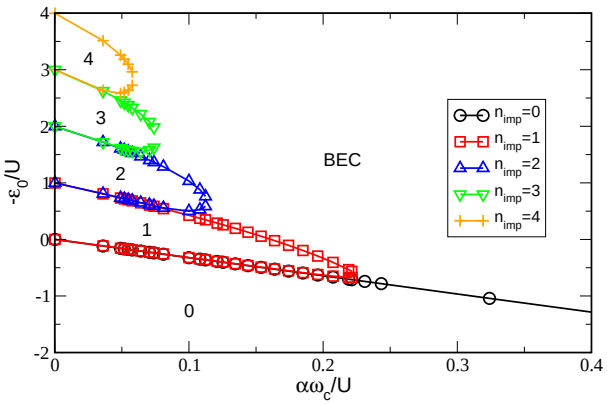

Figure 6.1: Zero-temperature phase diagram of the bosonic siAm for bath exponent $s = 0.6$ and fixed impurity Coulomb interaction $U = 0.5$. The different symbols denote the phase boundaries between Mott phases and the BEC phase. The Mott phases are labeled by their occupation n_{imp} for $\alpha = 0$. Only the Mott phases with $n_{imp} \leq 4$ are shown. The NRG parameters are $\Lambda = 2.0$, $N_b = 10$, and $N_s = 100$.

this chapter is devoted to the issues of the two phases. It is also expected that the NRG calculation gives the correct descriptions of the transition between the Mott and BEC phase but the physics at the phase boundary, represented by the non-trivial quantum critical fixed points, might be sensitive to the missing states at $\varepsilon = \mu = 0$.

6.2 Quantum phase transitions in the bosonic single-impurity Anderson model

On the contrary to the non-interacting BEC phase at $T = 0$, the BEC phase with finite critical temperature T^* is observed in the NRG flow diagram, which shows the BEC gap (Δ_{gap}) opening at $N^* = -\ln T^*$. Interestingly, we found quantum phase transitions between phases with $T_c = 0$ (Mott phase) and with $T_c \neq 0$ (BEC phase). In the former case (Mott phase), the impurity is independent of the bath and the non-interacting bath itself shows a BEC (ideal Bose gas) phase at $T = 0$ ($T > 0$). We call it as a Mott phase following the convention of the Bose-Hubbard Model (Bruder and Schön 1993, Kampf and Zimanyi 1993, Rokhsar and Kotliar 1991, Krauth, Caffarel and Bouchaud 1992, Freericks and Monien 1993).[4]

[4] Mott phases in the two models, bosonic single-impurity Anderson model and Bose-Hubbard model, imply different physical situations. For examples, a Mott phase in Bose-Hubbard model is an insulating phase whereas it corresponds to an ideal gas phase in bosonic single-impurity Anderson model. Nevertheless, we use the same terminology in a sense that, in both cases, the Coulomb repulsion U stabilizes a localized state at the impurity site (bosonic single-impurity Anderson model) or at each local site (Bose-Hubbard model).

In the latter case (BEC phase), at $T < T_c$, all the existing particles (bosons) form a condensate cloud (wave-function), being separated from continuum states of the bath with a gap Δ_{gap}.

The full phase diagram Fig. 6.1, showing the Mott, BEC phase and the phase boundary between them, is calculated with the bosonic NRG (Bulla et al. 2005), where the Hamiltonian Eq. (6.1) is mapped onto a semi-infinite chain,

$$H = \varepsilon_0 b^\dagger b + \frac{1}{2} U b^\dagger b (b^\dagger b - 1) + V(b^\dagger \bar{b}_0 + \bar{b}_0^\dagger b) + \sum_{n=0}^{\infty} \varepsilon_n \bar{b}_n^\dagger \bar{b}_n + \sum_{n=0}^{\infty} t_n (\bar{b}_n^\dagger \bar{b}_{n+1} + \bar{b}_{n+1}^\dagger \bar{b}_n). \tag{6.4}$$

Here the impurity couples to the first site of the chain via the hybridization $V = \sqrt{2\alpha/(1+s)}$. The bath degrees of freedom are in the form of a tight-binding chain with operators $\bar{b}_n^{(\dagger)}$, on-site energies ε_n, and hopping matrix elements t_n, which both fall off exponentially: $t_n, \varepsilon_n \propto \Lambda^{-n}$.

The technical details are same as in the spin-boson model except that we use the total particle-number N_{tot} as a conserved quantity in the Hamiltonian Eq. (6.1).[5] In actual calculations, N_{tot} is limited to the maximum value N_{tot}^{max} so that the grand canonical ensemble consists of a set of canonical ensemble systems with $N_{tot} = 0, 1, 2, ..., N_{tot}^{max}$. The maximum number N_{tot}^{max} is chosen to be large enough to avoid the artificial effects on the low-lying spectrum.

The $T = 0$ phase diagram in Fig. 6.1[6] is calculated for fixed $U = 0.5$ with the parameter space spanned by the dimensionless coupling constant α and the impurity energy ε_0. We choose $s = 0.6$ as the exponent of the power-law in $\Delta(\omega)$. (The s-dependence of the phase diagram is discussed in Fig. 6.10 below.) The phase diagram is characterized by a sequence of lobes, which we label by the occupation at the ground state n_{gr}. The Mott phases are separated from the BEC phase by lines of quantum critical points, which terminate (for $s = 0.6$) at a finite value of α, except for the $n_{gr} = 0$ phase, where the boundary extends up to infinite α. These transition can be viewed as the impurity analogue of the Mott transition in the lattice model, since it is the local Coulomb repulsion that prevents the formation of the BEC state.

6.2.1 BEC phase

A grand canonical system in the BEC phase, showing affinity for infinitely many particles, is characterized by the negative chemical potential $\mu < 0$. In the bosonic single-impurity model, the negative chemical potential appears in several ways of creating an attractive site into the reservoir.

[5] For details, see Appendix D.

[6] Precisely, it is a phase diagram at infinitesimal temperature $T > 0$. At zero temperature, the entire region is covered by BEC phase. See Appendix C.

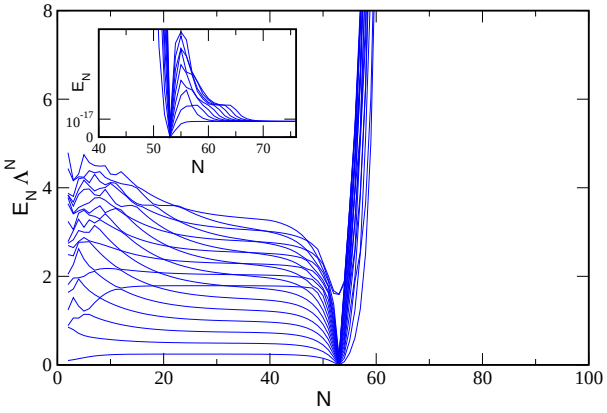

Figure 6.2: Flow diagram of the lowest lying many-particle levels E_N versus iteration number N for parameters $s = 0.4$, $\alpha = 0.007$, $U = 0.5$, and $\varepsilon_0 = -0.91383437$. There exists a gap Δ_g in the BEC phase ($N > 53$) between the ground state and the first excited state. See the inset where E_N (instead of $E_N\Lambda^N$) is plotted versus N.

1. An isolated ($\alpha = 0$) impurity with $\varepsilon_0 < 0$ and $U = 0$ creates a delta-peak at $\omega_{peak} = \varepsilon_0$ in the spectral density shifting the chemical potential to the peak position $\mu = \omega_{peak} = \varepsilon_0$. A finite coupling ($\alpha$) between the impurity and the bath will push the peak position ω_{peak} further down to the negative frequency ($\mu = \omega_{peak} < \varepsilon_0$).[7]

2. A similar situation can occur even for a positive ε_0 if the coupling α is large enough to generate a peak at $\omega_{peak} < 0$.

3. The same arguments on the spectral density and the negative ω_{peak} hold for an impurity with the finite U except that non-zero coupling α is necessary to get over the Coulomb repulsion U and form a condensate state with infinitely many particles.

A sharp peak in the spectral density $A(\omega)$ at $\omega = \omega_{peak} < 0$ is a good indication of BEC. Equivalently, the many particle spectra, which are more convenient objects for the NRG approach, also manifest the condensation with the appearance of gap Δ_g between the ground state and the first excited one.

See the inset of Fig. 6.2 where the many-particle energy $\{E_N\}$ is plotted as a function of the iteration number N. We focus on the BEC phase starting at $N \approx 53$.

The ground state is lying at zero of the vertical axis and the first excited state corresponds to the horizontal line at $E_N \approx 9 \times 10^{-18}$ for $N > 55$. There is a gap opening ($\Delta_g \approx 9 \times 10^{-18}$) at $N \approx 53$.

[7] See Fig. 6.3.

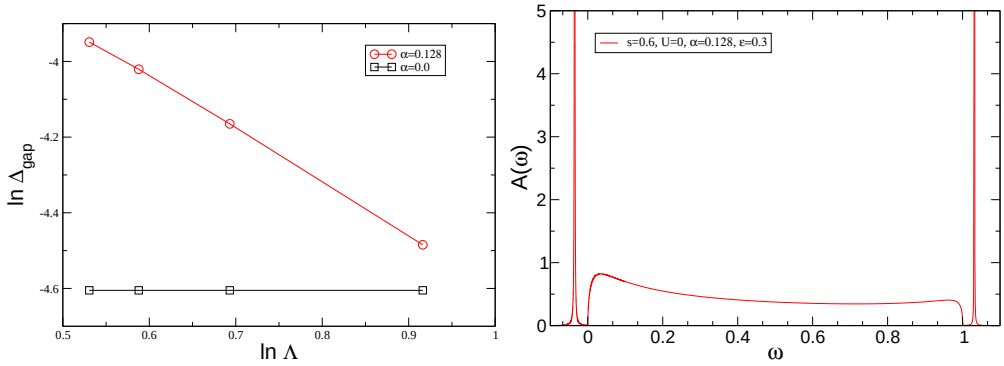

Figure 6.3: Left: The size of BEC gap Δ_g versus the logarithmic discretization parameter Λ. Data are shown for the bath exponent $s = 0.6$ and the zero Coulomb repulsion $U = 0$. The coupling strength α and the on-site energy ε_0 are given for each case differently. ($\alpha = 0.128$ and $\varepsilon_0 = 0.3$ for circle, $\alpha = 0.0$ and $\varepsilon_0 = -0.01$ for square.) The intersection at $x = 0$ determines the value of $\Delta_g(\Lambda \to 1)$: 0.036 (circle) and 0.01(square). Right: The spectral density $A(\omega)$ for parameters $s = 0.6$, $U = 0$, $\alpha = 0.128$ and $\varepsilon = 0.3$ (corresponding to the data with circles in the left). The coupling α creates two peaks out of the continuum. The distance from zero to the position of the left peak $|\omega_{peak}| \approx 0.036$ coincides with the size of gap in the NRG spectrum in the limit of $\Lambda \to 1$.

The many-particle levels in Fig. 6.2 show the states with quantum numbers $N_{tot} = 0, 1, 2, ...,$ and $N_{tot}^{max} (= 19)$[8]. In the ground state, all N_{tot}^{max} particles are occupied at a state with energy $\omega = -\Delta_g \approx -9 \times 10^{-18}$ whereas the first excited state has $N_{tot}^{max} - 1$ particles at $\omega = -\Delta_g \approx -9 \times 10^{-18}$ and the remaining one particle is excited to the lowest single-particle state $\omega = \xi_0^{(N)}$.[9] Thus the energy difference between the ground state and the first excited states is

$$\delta E = (-(N_{tot}^{max} - 1)\Delta_g + \xi_0^{(N)}) - (-N_{tot}^{max}\Delta_g) = \Delta_g + \xi_0^{(N)}. \tag{6.5}$$

The $\xi_0^{(N)}$ becomes much smaller than $\Delta_g \approx 9 \times 10^{-18}$ for large enough N (larger than sixty in Fig. 6.2)[10] so that we neglect it from Eq. (6.5):

$$\delta E \approx \Delta_g. \tag{6.6}$$

[8] The effect of N_{tot}^{max} on the size of gap Δ_g is less than 0.1% for $N_{tot}^{max} \geq 19$.

[9] $\xi_{0,N}$ is the lowest eigenvalues(eigenstates) of a free chain H_N.

$$H_N = \sum_{n=0}^{N-1} \varepsilon_n \bar{b}_n^\dagger \bar{b}_n + \sum_{n=0}^{N} t_n (\bar{b}_n^\dagger \bar{b}_{n+1} + \bar{b}_n \bar{b}_{n+1}^\dagger) = \sum_{n=1}^{N+1} \xi_n^{(N)} a_n^\dagger a_n$$

[10] $\xi_0^{(N)} \sim \Lambda^{-N} = 2^{-N}$ with $\Lambda = 2$.

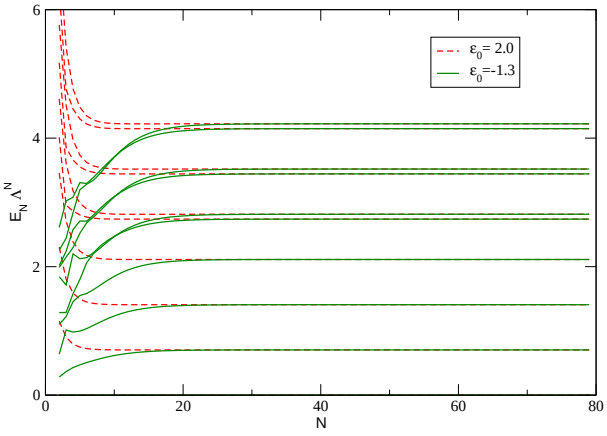

Figure 6.4: Flow diagram of the lowest lying many-particle levels $E_N\Lambda^{N-1}$ versus iteration number N for parameters $s = 0.4$, $\alpha = 0.007$, $U = 0.5$, and two values of $\varepsilon_0 = -1.3$ and 2.0.

For non-interacting systems ($U = 0$), the spectral density $A(\omega)$ and the position of the peak in the negative region make reasonable predictions of the size of the BEC gap Δ_g. The isolated and uncorrelated impurity with negative energy ε_0, ($\varepsilon_0 < 0$, $U = 0$ and $\alpha = 0$) generates a delta-function of the impurity spectral density $A(\omega) = \delta(\omega - \varepsilon_0)$ and the size of gap is purely determined by the on-site energy ε_0 independent of the bath (Fig. 6.3-Left :$\alpha = 0.0$):

$$\Delta_g(\Lambda \to 1) = |\varepsilon_0|. \tag{6.7}$$

However the impurity coupled to a bath with the finite coupling α causes the redistribution of the total spectral weight and the position of the peak (ω_{peak}) depends on the properties of the bath (α and s). Accordingly, the BEC gap Δ_g, corresponding to the distance from the peak to zero, also contains the detailed informations of the bath including the effect of discretization as well. The position of the peak in the impurity spectral density conforms with the size of the BEC gap shown in the NRG spectrum in the limit of $\Lambda \to 1$ (Fig. 6.3):

$$\Delta_g(\Lambda \to 1) = |\omega_{peak}|. \tag{6.8}$$

The spectral density $A(\omega)$ of the system with $U \neq 0$ has not been calculated yet but we expect that Eq. (6.8) is valid for the case, too.

6.2.2 Mott phase

The low-lying spectrum of the Mott phase (the flat-region in Fig. 6.4) is described by the Hamiltonian of the free semi-infinite chain,

$$H_{bath} = \sum_{n=0}^{\infty} \varepsilon_n \bar{b}_n^\dagger \bar{b}_n + \sum_{n=0}^{\infty} t_n (\bar{b}_n^\dagger \bar{b}_{n+1} + \bar{b}_{n+1}^\dagger \bar{b}_n). \tag{6.9}$$

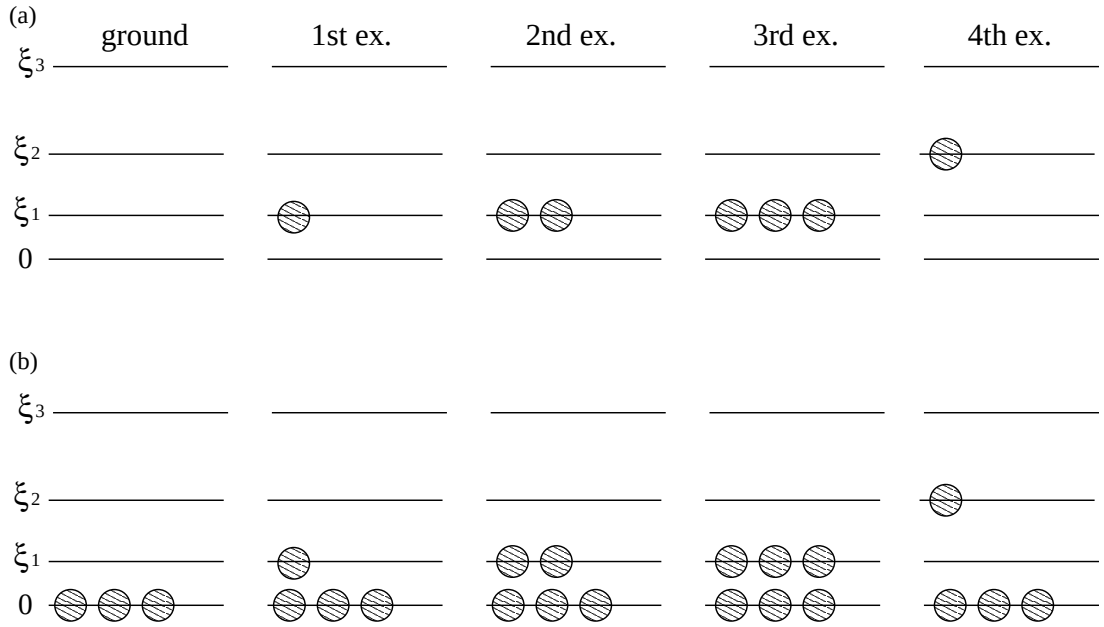

Figure 6.5: Single-particle spectrum of the non-interacting Hamiltonian $H_{bath,N}$ and the occupation of the ground, first,..., and the fourth excited states ($E_N = 0,\ \xi_{1,N},\ 2\xi_{1,N},\ 3\xi_{1,N}$ and $\xi_{2,N}$). For $\varepsilon_0 = 2.0$ (-1.3), the total number of particles at the ground, first, second, third and the fourth excited state are $N_{tot} = 0, 1, 2, 3$ $(3, 4, 5, 6)$ and 1 (4).

Fig. 6.4 shows two sets of energy-flows taken from two different lobes of the Mott phases in Fig. 6.1 ($\varepsilon_0 = -1.3$ and 2.0 for fixed $\alpha = 0.007$ and $U = 0.5$). Different structure in the early stage of iterations ($N < 20$) is a consequence of valence fluctuations at the impurity site. Both sets of many-particle spectra seem to flow into the same non-interacting fixed point H_{bath} but distinction is drawn by the assigned quantum numbers for the two cases.

For $\varepsilon_0 = 2.0$, the quantum number of the ground state, first, second, third and the fourth excited one are $N_{tot} = 0, 1, 2, 3$ and 1 whereas all the numbers are increased by three ($N_{tot} = 3, 4, 5, 6$, and 4) for $\varepsilon_0 = -1.3$. The three additional particles (bosons) in the latter case, consistently showing up in the higher states, all turn out to occupy the zero single-particle level. We discuss the details with the single-particle eigenvalues of the non-interacting Hamiltonian $H_{bath,N}$,

$$H_{bath,N} = \sum_{n=0}^{N-1} \varepsilon_n \bar{b}_n^\dagger \bar{b}_n + \sum_{n=0}^{N} t_n (\bar{b}_n^\dagger \bar{b}_{n+1} + \bar{b}_n \bar{b}_{n+1}^\dagger) = \sum_{n=1}^{N+1} \xi_{n,N} a_n^\dagger a_n. \qquad (6.10)$$

The eigenvalues of the lowest five many-particle states are given as $E_{0,N} = 0,\ E_{1,N} = \xi_{1,N}\ E_{2,N} = 2\xi_{1,N},\ E_{3,N} = 3\xi_{1,N}$ and $E_{4,N} = \xi_{2,N}$. Fig. 6.5 depicts the configurations of the five states: (a) $\varepsilon_0 - 2.0$ and (b) $\varepsilon_0 = -1.3$. The

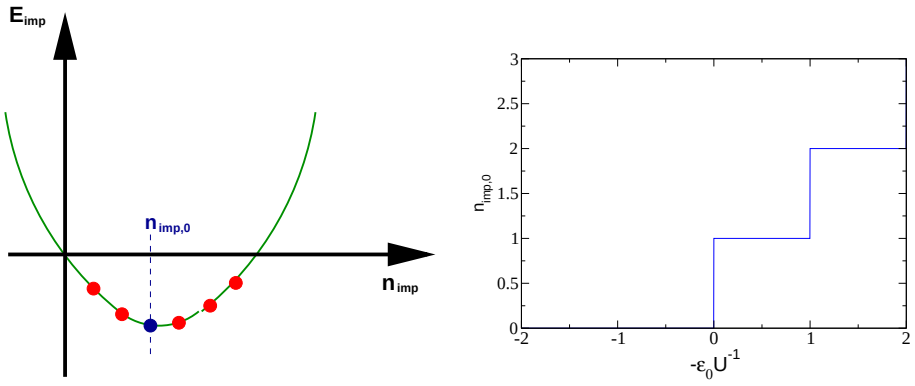

Figure 6.6: Left: The energy for an isolated impurity as a function of n_{imp}. The minimum point of the parabola is given by $(-\frac{\varepsilon_0}{U}+\frac{1}{2}, \frac{U}{2}(\frac{\varepsilon_0}{U}-\frac{1}{2})^2)$ and the actual occupation for energy minimum is determined by the nearest (non-negative) integer $n_{imp,0}$. The $n_{imp,0}$ is zero for a positive ε_0 regardless of the position of the minimum point. Right: The occupation at the minimum point $n_{imp,0}$ shows discontinuous jump for each integer value of $-\varepsilon_0/U$, where two values of $n_{imp,0}$ give equal minimum-energy. Between the integer points, the minimum point is determined by the single integer $n_{imp,0}$.

many-particle states with same energy have same number of particles at $\xi_{i,N} \neq 0$ so that the difference in N_{tot} is attributed to $\langle 0|\hat{n}_{tot}|0\rangle$ such as

$$\begin{aligned} \langle 0|\hat{n}_{tot}|0\rangle &= 0 \text{ for } \varepsilon_0 = 2.0, \\ \langle 0|\hat{n}_{tot}|0\rangle &= 3 \text{ for } \varepsilon_0 = -1.3 \end{aligned} \tag{6.11}$$

with $\hat{n}_{tot} = b^\dagger b + \sum_i \bar{b}_i^\dagger \bar{b}_i$.[11]

Two values of $\varepsilon_0 = 2.0$ and -1.3 were selected to represent the two different Mott phases labeled by 0 and 3 in Fig. 6.1. The similar arguments apply to the other Mott phases with different labels $1, 2, 4, 5$,... and so forth, and each phase is distinguished by the types of occupation at $|0\rangle$ (zero's single-particle level).[12] We use the zero-mode occupancy $\langle 0|\hat{n}_{tot}|0\rangle$ to label the different Mott phases and the next few pages are devoted to explain the properties of $\langle 0|\hat{n}_{tot}|0\rangle$. A remarkable point of the Mott phase is that the particles at $|0\rangle$ are excluded from thermal excitations being confined to the zero single-particle level $|0\rangle$. The reason is very obvious for the system with zero-coupling $\alpha = 0$, namely, a system with an isolated impurity. Let us focus on the impurity-part H_{imp}. Since the Hamiltonian is quadratic to $n_{imp} = b^\dagger b$, there exist certain occupations $n_{imp,0}$ that cause the minimum energy of the impurity. The minimum point $(n_{imp,0})$ is determined by ε_0 and U as shown in Fig. 6.6. The values of $-\varepsilon_0/U = 0.5$ determines the

[11] See the Hamiltonian in Eq. (6.4).
[12] The phases labeled by $1, 2, 4, 5$ have one, two, four and five bosons at $|0\rangle$.

occupation at the minimum point by $n_{imp,0} = 1$ and the corresponding minimum energy(ground state energy) by $E_{imp,0} = -U/2$. The energy-cost $U/2$ is charged for the transition from the ground state to the lowest excite ones $E_{imp,1} = E_{imp,2} = 0$ with $n_{imp} = n_{imp,0} \pm 1$.

Now, we consider the states of the bath $H_{bath,N}$ together with H_{imp}. The zero-coupling $\alpha = 0$ makes H_{imp} and $H_{bath,N}$ commute each other so that the eigenenergy (eigenfunction) of the full system is a simple sum (product) of the eigenenergy (eigenfunction) of H_{imp} and $H_{bath,N}$:

$$E_{tot,nm} = E_{imp,n} + E_{bath,m}, \quad |\Psi_{tot,nm}\rangle = |\psi_n\rangle \otimes |\phi_m\rangle, \tag{6.12}$$

with

$$\begin{aligned} H_{imp}|\psi_n\rangle &= E_{imp,n}|\psi_n\rangle, \quad H_{imp} = \varepsilon_0 b^\dagger b + \frac{1}{2} U b^\dagger b (b^\dagger b - 1), \\ H_{bath}|\phi_m\rangle &= E_{bath,m}|\phi_m\rangle, \quad H_{bath,N} = \sum_{n=1}^{N+1} \xi_{n,N} a_n^\dagger a_n. \end{aligned} \tag{6.13}$$

The ground state of the full system $H = H_{imp} + H_{bath}$ is given as

$$E_{tot,0} = E_{imp,0} = -U/2, \quad |\Psi_{tot,00}\rangle = b^\dagger |\Omega_{imp}\rangle \otimes |\Omega_{bath}\rangle, \tag{6.14}$$

where the impurity is occupied with a single boson[13] and the bath is empty. The lowest excited states are

$$\begin{aligned} E_{tot,1} &= -U/2 + \xi_{1,N}, \quad |\Psi_{tot,01}\rangle = a_1^\dagger |\Psi_{tot,00}\rangle, \\ E_{tot,2} &= -U/2 + 2\xi_{1,N}, \quad |\Psi_{tot,02}\rangle = (a_1^\dagger)^2 |\Psi_{tot,00}\rangle, \\ E_{tot,3} &= -U/2 + 3\xi_{1,N}, \quad |\Psi_{tot,03}\rangle = (a_1^\dagger)^3 |\Psi_{tot,00}\rangle, \\ E_{tot,4} &= -U/2 + \xi_{2,N}, \quad |\Psi_{tot,04}\rangle = a_2^\dagger |\Psi_{tot,00}\rangle, \\ &\cdots \end{aligned} \tag{6.15}$$

The many-particle levels with energy less than zero show the uniform occupancy at the impurity-site,

$$n_{imp} = \langle \Psi_{tot,00} | b^\dagger b | \Psi_{tot,00} \rangle = 1, \tag{6.16}$$

for the parameterization $-\varepsilon_0/U = 0.5$. Changing the value of $-\varepsilon_0/U$, we found discontinuous steps of n_{imp}[14]:

$$\begin{aligned} n_{imp} &= n_{imp,0} = 0, \quad -\varepsilon_0/U < 0, \\ n_{imp} &= n_{imp,0} = 1, \quad 0 < -\varepsilon_0/U < 1, \\ n_{imp} &= n_{imp,0} = 2, \quad 1 < -\varepsilon_0/U < 2, \\ n_{imp} &= n_{imp,0} = 3, \quad 2 < -\varepsilon_0/U < 3, \\ n_{imp} &= n_{imp,0} = 4, \quad 3 < -\varepsilon_0/U < 4, \\ &\cdots \end{aligned} \tag{6.17}$$

[13] The ground state of the isolated impurity system with $-\varepsilon_0/U = 0.5$.
[14] See Fig. 6.7.

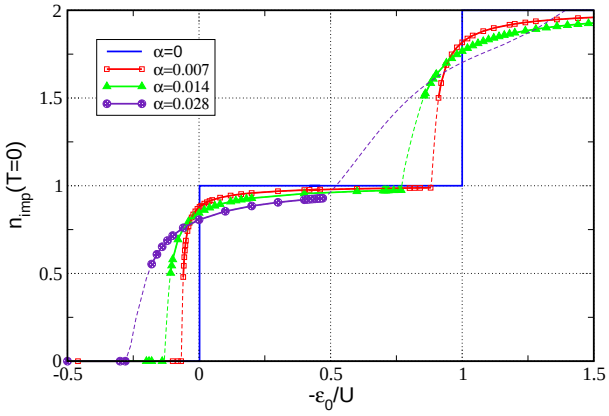

Figure 6.7: Impurity occupation n_{imp} as a function of ε_0 for temperature $T = 0$, $s = 0.4$, $U = 0.5$, and various values of α. The sharp steps for the decoupled impurity $\alpha = 0$ are rounded for any finite α. Symbols (dashed lines) correspond to data points within the Mott(BEC) phase.

The second case $n_{imp,0} = 3$ in Eq. (6.20) corresponds to the one that is illustrated in Fig. 6.5-(b) where three bosons are confined to the zero-level $|0\rangle$.[15] Thus "trapping" the particles at zero-mode (zero single-particle level $|0\rangle$) occurs exactly at the impurity-site if the coupling to the bath α is zero:

$$n_{imp,0} = \langle 0|\hat{n}_{tot}|0\rangle = 3, \tag{6.18}$$

for $\alpha = 0$ and $2 < -\varepsilon_0/U < 3$.

For a finite α, H_{imp} no more commutes to H_{bath} and the eigenstates of the full system are now linear combinations of $|\psi_n\rangle \otimes |\phi_m\rangle$ for various n and m:[16]

$$|\Phi_{tot,l}\rangle = \sum_{nm} u_{l,nm}|\psi_n\rangle \otimes |\phi_m\rangle. \tag{6.19}$$

The total number of particles n_{tot} has to be conserved and, for a ground state, we found that

$$\begin{aligned}
n_{tot,0} &= 0, \quad && -\tfrac{\varepsilon_0}{U} < 0, \\
n_{tot,0} &= 1, && 0 < -\tfrac{\varepsilon_0}{U} < 1, \\
n_{tot,0} &= 2, && 1 < -\tfrac{\varepsilon_0}{U} < 2, \\
n_{tot,0} &= 3, && 2 < -\tfrac{\varepsilon_0}{U} < 3, \\
n_{tot,0} &= 4, && 3 < -\tfrac{\varepsilon_0}{U} < 4, \\
&\cdots
\end{aligned} \tag{6.20}$$

[15] See Eq. (6.11).
[16] Compare this with Eq. (6.12).

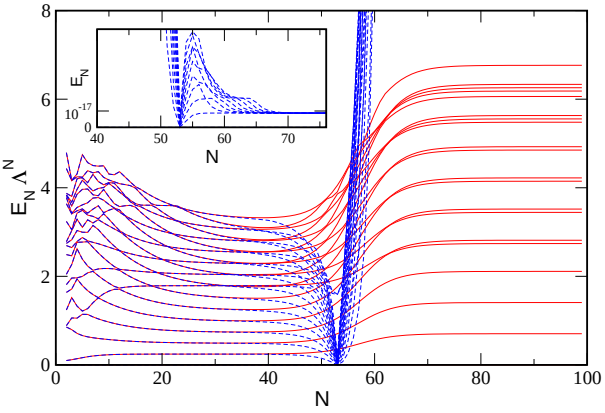

Figure 6.8: Flow diagram of the lowest lying many-particle levels E_N versus iteration number N for parameters $s = 0.4$, $\alpha = 0.007$, $U = 0.5$, and two values of ε_0 very close to the quantum phase transition between the Mott phase with $n_{imp} = 2$ and the BEC phase. Both the quantum critical point and the Mott phase appear as fixed points in this scheme whereas in the BEC phase, a gap Δ_g appears between the ground state and the first excited state, see the inset where E_N (instead of $E_N\Lambda^N$) is plotted versus N.

with $n_{tot,0} = \langle\Phi_{tot,0}|\hat{n}_{tot}|\Phi_{tot,0}\rangle$.

The excited states are written in the same way as in Eq. (6.15) by replacing the ground state $|\Psi_{tot,00}\rangle$ in Eq. (6.14) to $|\Phi_{tot,0}\rangle$ in Eq. (6.19).

$$\begin{aligned}
E_{tot,1} &= E_{tot,0} + \xi_{1,N}, \quad |\Phi_{tot,1}\rangle = a_1^\dagger|\Phi_{tot,0}\rangle, \\
E_{tot,2} &= E_{tot,0} + 2\xi_{1,N}, \quad |\Phi_{tot,2}\rangle = \left(a_1^\dagger\right)^2|\Phi_{tot,0}\rangle, \\
E_{tot,3} &= E_{tot,0} + 3\xi_{1,N}, \quad |\Phi_{tot,3}\rangle = \left(a_1^\dagger\right)^3|\Phi_{tot,0}\rangle, \\
E_{tot,4} &= E_{tot,0} + \xi_{2,N}, \quad |\Phi_{tot,4}\rangle = a_2^\dagger|\Phi_{tot,0}\rangle, \\
&\ldots
\end{aligned} \tag{6.21}$$

Thus the only effect of the coupling α is in the energy and the wavefunction of the ground state. The ground state energy is always defined as zero in NRG approach so that the many-particle spectrum does not change with the value of α. However the wavefunction $|\Phi_{tot,0}\rangle$, a mixed state between the impurity and the bath, has some dependences on the coupling α. Since the impurity occupation $\hat{n}_{imp} = b^\dagger b$ no more commutes to the full Hamiltonian $H = H_{imp} + H_{bath}$, calculation of the average impurity-occupation at the ground state yields a fractional number for a non-zero coupling $\alpha \neq 0$. Fig. 6.7 shows the dependence of

$$n_{imp}(T = 0) = \langle\Phi_{tot,0}|\hat{n}_{imp}|\Phi_{tot,0}\rangle \tag{6.22}$$

on ε_0 for $s = 0.4$, $U = 0.5$, and various values of α. Different Mott phases and the transitions among them are very distinctive in the step-function of the n_{imp}-

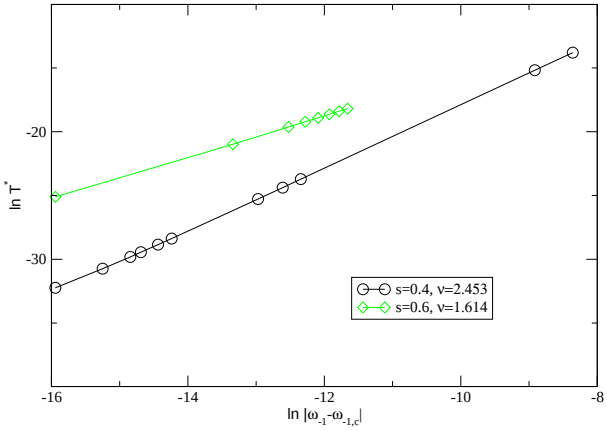

Figure 6.9: The crossover scale from the quantum critical phase to the BEC/Mott phase. Upon variation of ε_0 close to the critical value $\varepsilon_{0,c}$, the crossover scale T^* vanishes with a power-law at the transition point, $T^* \propto |\varepsilon_0 - \varepsilon_{0,c}|^\nu$ with a non-trivial exponent ν.

curve for $\alpha = 0$. However, for finite α, the sharp steps and the well-developed plateaus disappear so that it is hard to find out the evidences of transitions and the different phases within the n_{imp}-curve. Nevertheless we checked the value of $n_{tot,0}$ in Eq. (6.19) for each data point in Fig. 6.7 and clarified the corresponding phase. For $\alpha = 0.007$ and $\alpha = 0.014$, there are three Mott phases (symbols) with $n_{tot,0} = 0, 1$ and 2, which are intercepted by fragments of BEC-phases identified with $n_{tot,0} = N_{tot}^{max}$ (dashed lines). For $\alpha = 0.028$, only two Mott phases with $n_{tot} = 0$ and 1 appear and the rest region is covered by BEC-phase.[17]

The ground state occupation $n_{tot,0}$ shows discontinuous change or even singular behavior at the phase-boundary between Mott phases and BEC phases. On the contrary, the impurity contribution n_{imp} always shows continuous increase even when the curves cross the BEC phase.[18]

6.2.3 Quantum critical phase

The flow diagram in Fig. 6.8 shows the lowest lying many-particle levels for parameters $s = 0.4$, $\alpha = 0.007$, $U = 0.5$, and two values of ε_0 very close to the quantum critical point.[19] The NRG spectrum of the BEC phase (dashed lines :$N \geq 53$) has been already discussed in Section 6.2.1 with the same spectrum in Fig. 6.2. A slight change of ε_0 from -0.91383437 to -0.91383436 results in a new set of low lying states (solid lines). Both sets of energy states show identical

[17] Compare the data with the phase-diagrams in Fig. 6.1.

[18] The N_{tot}^{max}-dependence of $n_{imp}(T = 0)$ is checked with increasing N_{tot}^{max}. The error is less than 0.01% for $N_{tot}^{max} \gtrsim 19$.

[19] $\varepsilon_0 = -0.91383436$: solid lines, $\varepsilon_0 = -0.91383437$: dashed lines

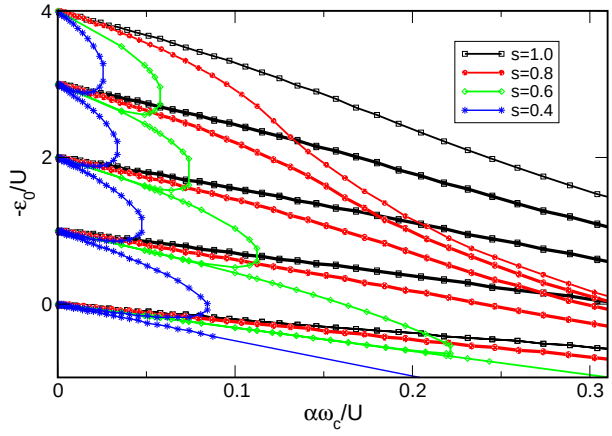

Figure 6.10: Zero-temperature phase diagram of the bosonic siAm as in Fig.6.1, but now for different values of the bath exponent s. For increasing values of s, the areas occupied by the Mott phases significantly change their shapes, and for $s = 0.8$ it appears that each Mott phase extends up to arbitrarily large values of α.

structure in the earlier iterations ($N \lesssim 40$) but turn into the different phases of the Mott (solid lines) and the BEC phase (dashed lines) around $N \sim 50$. The non-interacting fixed point in the Mott phase has been analyzed in Section 6.2.2 and the BEC gap between the ground state and the first excited one in Section 6.2.1. The intermediate fixed point showing up in the earlier stage of iterations has different structure from the non-interacting fixed point: the density of states is higher and the level-spacing is even. More quantitative analysis of the quantum critical fixed points has to be done in near future.

Another interesting point is the crossover scale from the quantum critical phase to the BEC and Mott phase. Numerically we find that upon variation of ε_0 close to its critical value $\varepsilon_{0,c}$, the crossover scale vanishes with a power-law at the transitions,

$$T^* \propto |\varepsilon_0 - \varepsilon_{0,c}|^\nu, \tag{6.23}$$

on both sides of the transition, with a non-trivial exponent ν. Preliminary results suggest that $\nu = 1/s$ holds for $0 < s < 1$.

6.3 Effects of the bath exponent in $T = 0$ phase diagrams

The precise shape of the boundaries in the phase diagram in Fig. 6.1 depends on the form of $\Delta(\omega)$ for *all* frequencies. Here we stick to the power-law form Eq. (6.3) and present the dependence of the phase diagram on the bath exponent s in Fig. 6.10. We observe that upon increasing the value of s, the areas occupied by the Mott phases extend to larger values of α and significantly change their shape. A qualitative change is observed for large exponent $s = 0.8$ and $s = 1.0$.

The Mott phases appear to extend up to arbitrarily large values of α and the BEC phase which separates the Mott phases is completely absent.

The case $s = 0$ (constant bath density of states) turns out to be difficult to access numerically. An extrapolation of the phase boundaries for values of s in the range $0.1, \cdots, 0.4$ to $s = 0$ is inconclusive, but the Mott phase is at least significantly suppressed in this limit.

7. SUMMARY

The NRG, originally developed for the solution of the Kondo problem, proved the power of a non-perturbative method in other impurity models by successfully describing the physics of quantum phase transitions and quantum critical points of the models.

The focus of investigating the impurity quantum phase transitions is rather different from the ones in lattice models. For example, the physics of spatial correlations, one of the most important features that describes the criticality of lattice systems, has no counterpart in impurity systems, where quantum criticality is involved in the local physics at the impurity site such as the local magnetic susceptibility

$$\chi_{loc} = \left[\frac{\partial^2 \mathcal{F}_{imp}}{\partial h^2}\right]_{h=0}. \tag{7.1}$$

Here h is the local magnetic field. The temporal correlations is important in any case but, in particular for the impurity models, the local dynamics of the impurity spin, σ^z, would be a matter of interest. i.e.:

$$\mathcal{C}(\tau) = \langle \sigma^z(\tau)\sigma^z(0)\rangle. \tag{7.2}$$

The global dynamics can also attract our attentions if the impurity contribution of the thermodynamic quantities of $S_{imp}(T)$ and $\chi_{imp}(T)$ show non-trivial prefactors that frequently indicate the fractional charges or spin momentums at the critical points.

The quantum phase transition in the soft-gap Anderson model, found in the early nineties (Withoff and Fradkin 1990), was studied in many different contexts and here we added a complete understanding of the NRG many-body spectrum of critical fixed points by utilizing renormalized perturbation theory around a non-interacting fixed point. The non-trivial level structure with reduced degeneracies and non-equidistant levels was reconstructed by adding the perturbative corrections of the marginal interactions in the vicinity of the critical dimensions, $r = 0$ and $r = 1/2$. We found that the impurity spin in the quantum critical phase is fluctuating in arbitrary small temperature T, which gives a clue to the non-trivial Curie-Weiss constant $\mathcal{C}_{imp}$[1] different from the free-impurity value $S(S+1)/3$.

A new extension of the NRG method to the spin-boson model broadened our viewpoints from a fixed exponent $s = 1$ to the range of exponents $0 < s \leq 1$ and,

[1] $\lim_{T\to 0} \chi_{imp}(T) = \mathcal{C}_{imp}/T$.

as the most important outcome, we found second order transitions dividing the parameter space into the localized and the delocalized phases, where the two-level system stays either at the two-fold degenerate eigenstates of $\hat{\sigma}_z$ (localized) or the single lowest eigenstate of $\hat{\sigma}_x$ (delocalized). The two-fold degeneracy in the localized phase and the lifting in the delocalized phase are manifested in the residual value of S_{imp} by the $\ln 2$ difference. In the quantum critical phase, the residual entropy is quenched to a value between 0 and $\ln 2$, implying that the subsystem is fluctuating for arbitrarily small temperature T. The origin of the quantum fluctuation could be clarified with analysing the structure of the quantum critical fixed points. We expect that, in the vicinity of the critical dimensions $s = 0$ and $s = 1$, the many-particle spectrum at the quantum critical points is perturbatively accessible within a single-particle picture.

A model with a bosonic impurity state coupled to a non-interacting bosonic surrounding, what is called, the bosonic single-impurity Anderson model, was studied with the NRG and it turned out that there exist quantum phase transitions and quantum critical points separating the BEC phase from the Mott phases. The terminology was obtained in analogy to the Bose-Hubbard model regarding the connection of the bosonic single-impurity Anderson model with the Bose-Hubbard model via DMFT (Dynamic Mean-Field Theory). The physics of the two cases, however, is quite different and the distinct description[2] is necessary to prevent the possible confusion. The $T = 0$ phase diagram of the bosonic single-impurity Anderson model for various α/U and ε_0/U shows apparent similarity as the one for the Bose-Hubbard model depicted in the two-dimensional plane of t/U and μ/U.[3] The character of the Mott phase is pretty clear in a sense that the many-particle spectrum is simply understood as the one of the non-interacting bath. The low-lying spectrum of the BEC phase is rather sensitive to the computational errors that are originated from discretization and truncation processes. However the size of the gap Δ_g itself is quite reliable even in that condition and, for simple cases, we confirmed that the continuum limit, $\Lambda \to 1$, shows good agreements with the exact value. The current results strongly indicate that the BEC gap Δ_g vanishes at the transition from the BEC phase to the Mott phase and the system shows quantum critical behavior near to the transition point. Details about the quantum critical phase such as the size of the gap $|\Delta_g|$ and the structure of the quantum critical point are under investigation. Furthermore, it is very desirable to calculate the dynamical quantities of the given impurity model and make a self-consistent connection to the Bose-Hubbard model via DMFT (Metzner and Vollhardt 1989, Georges, Kotliar, Krauth and Rozenberg 1996, Bulla 1999, Bulla, Costi and Vollhardt 2001).

[2] We regard a phase as a BEC state only if the critical temperature T^* is finite (to be precise, the crossover temperature T^*), the Mott phases do not guarantee the integer occupation at the local (impurity) site, and so forth.

[3] t:hopping parameter, μ:chemical potential and U:Coulomb repulsion.

APPENDIX

A. FIXED-POINTS ANALYSIS: SOFT-GAP ANDERSON MODEL

The low-lying spectra at the local-moment and strong coupling fixed points are the eigenstates of the non-interacting Hamiltonian $H_{c,N}$,

$$H_{c,N} = \sum_{\sigma n=0}^{N-1} t_n (c^\dagger_{n\sigma} c_{n+1\sigma} + c^\dagger_{n+1\sigma} c_{n+1\sigma}), \tag{A.1}$$

which is written in a diagonal form,

$$\bar{H}_{c,N} = \sum_{\sigma p} \epsilon_p \xi^\dagger_{p\sigma} \xi_{p\sigma}. \tag{A.2}$$

The energy of the many-particle levels in the two cases is understood with the single-particle spectrum $\{\epsilon_p\}$.

On the contrary, the spectrum at the quantum critical fixed point is not captured within the single-particle picture of $H_{c,N}$ since the marginal interaction $\hat{O}$ raises electronic correlations among particles. However, the effect of marginal interaction vanishes in the limit of $r \to 0$ and $r \to 1/2$ and the perturbative corrections to the eigenstates of $H_{c,N}$ give the correct structure of the quantum critical fixed point. For a non-degenerate case, the first order correction is

$$\Delta E^{(1)}_i = \langle \psi^{(0)}_i | \hat{O} | \psi^{(0)}_i \rangle, \tag{A.3}$$

where $|\psi^{(0)}_i\rangle$ and $E^{(0)}_i$ are the eigenstate and the eigenvalue of $H_{c,N}$, respectively.[1]

As a first step to calculate Eq. (A.3), we obtain the explicit form of the non-interacting eigenstates $|\psi^{(0)}_i\rangle$ in terms of the single-particle operators $\{\xi^{(\dagger)}_{p\sigma}\}$ and the vacuum field $|0\rangle$.

$$|\psi^{(0)}_i\rangle = \sum_{\{n_p, n_q\}} A_{n_p,n_q} \prod_{pq} (\xi^\dagger_{p\uparrow})^{n_p} (\xi^\dagger_{q\downarrow})^{n_q} |0\rangle. \tag{A.4}$$

The occupation $\{n_p, n_q\}$ and the corresponding coefficients A_{n_p,n_q} are determined to yield the quantum numbers (charge and spin) of the given state. In Appendix A.1, we perform the calculation for various quantum states.

[1] $\hat{H}_{c,N} |\psi^{(0)}_i\rangle = E^{(0)}_i |\psi^{(0)}_i\rangle$.

In the next step, we write the marginal operator $\hat{O}$ in terms of $\{\xi^{(\dagger)}_{p,\sigma}\}$. Near to the critical dimension $r = 0$, the marginal interaction is given by a Kondo-type coupling,

$$\begin{aligned}\hat{J} = \vec{S}_{\rm imp} \cdot \vec{s}_0 &= \frac{1}{2} S^{+}_{\rm imp} c^{\dagger}_{0\downarrow} c_{0\uparrow} + \frac{1}{2} S^{-}_{\rm imp} c^{\dagger}_{0\uparrow} c_{0\downarrow} \\ &\quad + \frac{1}{2} S^{z}_{\rm imp} \left(c^{\dagger}_{0\uparrow} c_{0\uparrow} - c^{\dagger}_{0\downarrow} c_{0\downarrow} \right). \end{aligned} \tag{A.5}$$

Since the electronic operator $c^{(\dagger)}_{0\mu}$ is expressed with the operators $\xi^{(\dagger)}_{p\mu}$:

$$c_{0\mu} = \sum_{p} \alpha_{0p} \xi_{p\sigma}, \quad c^{\dagger}_{0\mu} = \sum_{p} \alpha^{*}_{0p} \xi^{\dagger}_{p\sigma}, \tag{A.6}$$

the interaction $\hat{J}$ is expressed with linear sums of the quadratic excitations $\xi^{\dagger}_{p\mu}\xi_{q\nu}$ for various momentums and spins:

$$\begin{aligned}\hat{J} = \vec{S}_{\rm imp} \cdot \vec{s}_0 &= \frac{1}{2} S^{+}_{\rm imp} \left(\sum_{pq} \alpha^{*}_{0p} \alpha_{0q} \xi^{\dagger}_{p\downarrow} \xi_{q\uparrow} \right) + \frac{1}{2} S^{-}_{\rm imp} \left(\sum_{pq} \alpha^{*}_{0p} \alpha_{0q} \xi^{\dagger}_{p\uparrow} \xi_{q\downarrow} \right) \\ &\quad + \frac{1}{2} S^{z}_{\rm imp} \left(\sum_{pq} \alpha^{*}_{0p} \alpha_{0q} \xi^{\dagger}_{p\uparrow} \xi_{q\uparrow} - \sum_{pq} \alpha^{*}_{0p} \alpha_{0q} \xi^{\dagger}_{p\downarrow} \xi_{q\downarrow} \right). \end{aligned} \tag{A.7}$$

In the vicinity of $r = 1/2$, the Coulomb repulsion,

$$\hat{U} = (\hat{n}_{\uparrow} - \frac{1}{2})(\hat{n}_{\downarrow} - \frac{1}{2}), \tag{A.8}$$

is applied to the first site of the conduction chain so that the terms like

$$\begin{aligned}\hat{n}_{\uparrow}\hat{n}_{\downarrow} &= c^{\dagger}_{0\uparrow} c_{0\uparrow} c^{\dagger}_{0\downarrow} c_{0\downarrow}, \\ \hat{n}_{\uparrow} &= c^{\dagger}_{0\uparrow} c_{0\uparrow}, \\ \hat{n}_{\downarrow} &= c^{\dagger}_{0\downarrow} c_{0\downarrow}, \end{aligned} \tag{A.9}$$

create the one-particle, $\xi^{\dagger}_{p\uparrow}\xi_{q\downarrow}$, or the two-particle excitations, $\xi^{\dagger}_{p\uparrow}\xi_{q\downarrow}\xi^{\dagger}_{r\uparrow}\xi_{s\downarrow}$, in the marginal operators $\hat{U}$:

$$\hat{U} = \left(\sum_{pq} \alpha^{*}_{0p} \alpha_{0q} \xi^{\dagger}_{p\uparrow} \xi_{q\uparrow} - \frac{1}{2} \right) \left(\sum_{rs} \alpha^{*}_{0r} \alpha_{0s} \xi^{\dagger}_{r\downarrow} \xi_{s\downarrow} - \frac{1}{2} \right). \tag{A.10}$$

The first order correction of $\langle \psi^{(0)}_i | \hat{J} | \psi^{(0)}_i \rangle$ and $\langle \psi^{(0)}_i | \hat{U} | \psi^{(0)}_i \rangle$ can be calculated if we know the coefficients A_{n_p,n_q} and α_{0p} for all indices p and q. The detailed calculations will be given in Appendix A.2 and A.3.

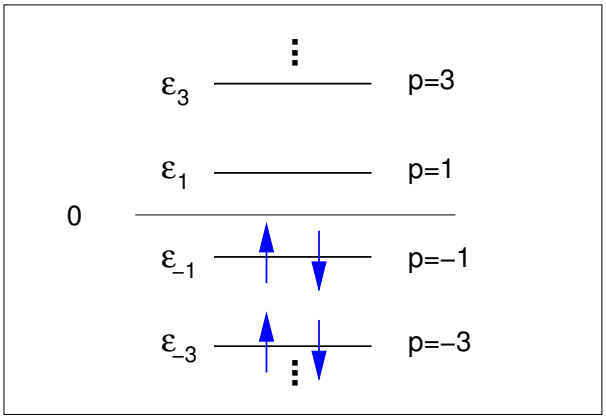

Figure A.1: Single-particle spectrum of the free conduction electron chain Eq. (A.12). The ground state is given by all the levels with $p < 0$ filled.

A.1 Local moment fixed points

The conduction-electron part of the iterative Hamiltonian (Nth step) is given by

$$H_{c,N} = \sum_{\sigma n=0}^{N-1} t_n (c^\dagger_{n\sigma} c_{n+1\sigma} + c^\dagger_{n+1\sigma} c_{n+1\sigma}). \tag{A.11}$$

The $H_{c,N}$ can be written in a diagonal form,

$$\bar{H}_{c,N} = \sum_{\sigma p} \epsilon_p \xi^\dagger_{p\sigma} \xi_{p\sigma} \tag{A.12}$$

where ϵ_p is the single-particle spectrum of $H_{c,N}$. Since the single-particle spectrum depends on whether the total number of sites is even or odd, we discuss two cases separately.

If $N+1$ (the total number of free-electronic sites) is even, the single-particle spectrum of the free chain is as sketched in Fig. A.1. As we assume particle-hole symmetry, the positions of the single-particle levels are symmetric with respect to 0 with

$$\epsilon_p = -\epsilon_{-p}, \;\; p = 1, 3, \cdots, N, \tag{A.13}$$

and

$$\sum_p \equiv \sum_{p=-N,\; p \;odd}^{p=N} \tag{A.14}$$

Note that an equally spaced spectrum of single-particle levels is only recovered in the limit $\Lambda \to 1$ for the case $r = 0$.[2] Figure A.1 shows the ground-state

[2] See Fig. 6 in (Bulla, Hewson and Zhang 1997).

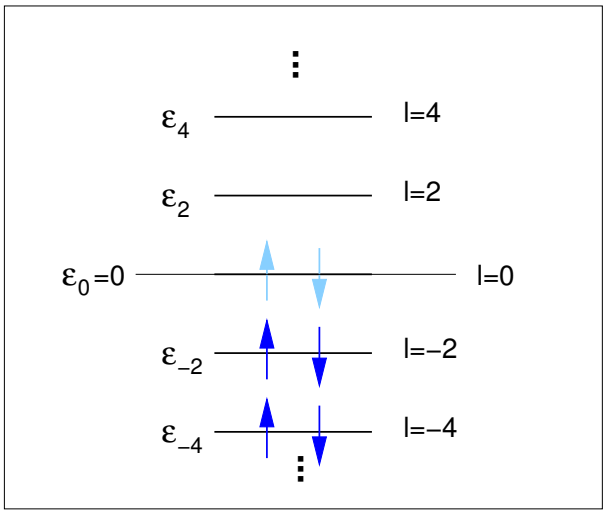

Figure A.2: Single-particle spectrum of the free conduction electron chain for odd-number of free-sites. The ground state is fourfold degenerate with all the levels with $p < 0$ filled and the level $p = 0$ either empty, singly ($\uparrow$ or $\downarrow$) or doubly occupied.

configuration (half-filling). The states of the lowest excitations are easily obtained by creating a few particles and holes from the ground state. In terms of the single-particle operators in Eq. (A.12),[3]

$$\begin{aligned} |\psi_{1\mu}\rangle &= \xi^\dagger_{1\mu}\xi_{-1\mu}|\psi_0\rangle,\ E = 2\epsilon_1 \\ |\psi_{2\mu}\rangle &= \xi^\dagger_{3\mu}\xi_{-1\mu}|\psi_0\rangle,\ E = \epsilon_1 + \epsilon_3 \\ |\psi_{30}\rangle &= \xi^\dagger_{1\mu}\xi_{-1\mu}\xi^\dagger_{1\nu}\xi_{-1\nu}|\psi_0\rangle,\ E = 4\epsilon_1\ (\mu \neq \nu) \\ &\cdots \end{aligned} \tag{A.15}$$

with

$$|\psi_0\rangle = \prod_{p<0} \xi^\dagger_{p\uparrow}\xi^\dagger_{p\downarrow}|0\rangle. \tag{A.16}$$

The spin-indices are determined by the quantum numbers of the states and we will discuss them later on.

If $N + 1$ is odd, the single-particle spectrum of the free chain is as sketched in Fig. A.2. As in the previous case, the positions of the single-particle levels are symmetric with respect to 0 with

$$\epsilon_0 = 0,\ \epsilon_p = -\epsilon_{-p},\ p = 2, 4, \cdots, N, \tag{A.17}$$

[3] All the bracket states in Eq. (A.15) and Eq. (A.19) consist of only the conduction-electrons ($|\psi_n\rangle = |\psi_n\rangle^{cond}$). The eigenstates of the full system are expressed in products with the ones of impurities. For example, $|\psi\rangle^{tot} = a|\psi_{1\uparrow}\rangle^{cond} \otimes |\downarrow\rangle^{imp} + b|\psi_{1\downarrow}\rangle^{cond} \otimes |\uparrow\rangle^{imp} + \cdots$. The coefficients a and b are determined according to the quantum numbers of $|\psi\rangle^{tot}$.

and

$$\sum_{p} \equiv \sum_{p=-N,\ p\ odd}^{p=N} . \tag{A.18}$$

In this case, the ground state of the effective model for an odd-number of free sites is fourfold degenerate, with all levels with $p < 0$ filled and the level $p = 0$ either empty, singly ($\uparrow$ or $\downarrow$) or doubly occupied. Possible lowest excitations are

$$\begin{aligned} |\psi_1\rangle &= \xi^\dagger_{0\uparrow}\xi_{-2\uparrow}|\psi_0\rangle,\ E = \epsilon_2 \\ |\psi_2\rangle &= \xi^\dagger_{0\uparrow}\xi_{-2\uparrow}\xi^\dagger_{0\downarrow}\xi_{-2\downarrow}|\psi_0\rangle,\ E = 2\epsilon_2 \\ |\psi_3\rangle &= \xi^\dagger_{0\uparrow}\xi_{-4\uparrow}|\psi_0\rangle,\ E = \epsilon_4 \\ &\cdots \end{aligned} \tag{A.19}$$

with

$$|\psi_0\rangle = \prod_{p<0} \xi^\dagger_{p\uparrow}\xi^\dagger_{p\downarrow}|0\rangle. \tag{A.20}$$

Comparing the two equations, Eq. (A.19) and Eq. (A.15), we find the differences in the many-particle spectrum depending on the parity of $N + 1$. This even-odd effect, which is originated from discretization of a continuous band, seems to make it difficult to define fixed points since the RG-mapping ($\boldsymbol{R}$) in Eq. (3.53) changes parity of H_N in every iteration. However the original Hamiltonian in Eq. (3.3) conserves total charge and parity so that any transitions are forbidden between states with different parity. Therefore we can choose one subset of eigenstates with even (or odd) parity and, regardless of the choice, investigate general properties of the model. The many-particles spectrums collected in every other iterative step belong to the same parity-group and quickly flow into the fixed point of the conduction band.

In the following section, we obtain the explicit form of the many-particle states for several sets of $\{Q, S, S_z\}$. We focus on the case of $N + 1 = even$.

A.1.1 $\mathrm{Q} = 0$, $\mathrm{S} = 1/2$ and $\mathrm{S_z} = 1/2$

The local-moment fixed point is described with an effective Hamiltonian,

$$H_{LM} = \lim_{U\to\infty} H_{imp} + \sum_{\sigma p} \epsilon_p \xi^\dagger_{p\sigma}\xi_{p\sigma} \tag{A.21}$$

with

$$H_{imp} = \varepsilon_f \sum_{\sigma} f^\dagger_{-1\sigma} f_{-1\sigma} + U f^\dagger_{-1\uparrow} f_{-1\uparrow} f^\dagger_{-1\downarrow} f_{-1\downarrow}. \tag{A.22}$$

Infinitely large Coulomb repulsion U prohibits a double-occupied and empty state from the impurity-site and leaves a single electron with spin-up or spin-down on it, which makes $\mathrm{Q^{imp}} = 0$, $\mathrm{S^{imp}} = 1/2$ and $\mathrm{S_z^{imp}} = \pm 1/2$.

$$|\psi\rangle_{imp} = f^\dagger_\sigma|0\rangle_{imp},\ (\sigma = \uparrow \text{ or } \downarrow) \tag{A.23}$$

The ground state of the local moment fixed point is a product of $|\psi\rangle_{imp}$ and the half-filled ground state of the free chain, depicted in Fig. A.1:

$$|\psi_{gr}\rangle = f_\sigma^\dagger|\psi_0\rangle, \tag{A.24}$$

with

$$|\psi_0\rangle = |0\rangle_{imp} \otimes \big[\prod_{p<0} \xi_{p\uparrow}^\dagger \xi_{p\downarrow}^\dagger |0\rangle_{cond}\big]. \tag{A.25}$$

Since the charge of the ground state is zero, all excitations with $Q = 0$ should create the same number of particles and holes from the ground state. Considering the excitations with a single-pair of particle and hole,

$$|\psi\rangle \;=\; f_\sigma^\dagger \xi_{p\mu}^\dagger \xi_{q\nu} |\psi_0\rangle,\; E = \epsilon_p - \epsilon_q \tag{A.26}$$

with $p > 0$, $q < 0$, $\epsilon_p > 0$ and $\epsilon_q < 0$.

Spin-indices μ, ν and σ are determined by given S and S_z. Taking account of all possible configurations of the three-spin system, we have a 8-dimensional space with a set of basis:

$$\begin{aligned}
|+1/2,+1/2,+1/2\rangle &= f_\uparrow^\dagger \xi_{p\uparrow}^\dagger \xi_{q\downarrow} |\psi_0\rangle, \\
|+1/2,+1/2,-1/2\rangle &= f_\uparrow^\dagger \xi_{p\uparrow}^\dagger \xi_{q\uparrow} |\psi_0\rangle, \\
|+1/2,-1/2,+1/2\rangle &= f_\uparrow^\dagger \xi_{p\downarrow}^\dagger \xi_{q\downarrow} |\psi_0\rangle, \\
|+1/2,-1/2,-1/2\rangle &= f_\uparrow^\dagger \xi_{p\downarrow}^\dagger \xi_{q\uparrow} |\psi_0\rangle, \\
|-1/2,+1/2,+1/2\rangle &= f_\downarrow^\dagger \xi_{p\uparrow}^\dagger \xi_{q\downarrow} |\psi_0\rangle, \\
|-1/2,+1/2,-1/2\rangle &= f_\downarrow^\dagger \xi_{p\uparrow}^\dagger \xi_{q\uparrow} |\psi_0\rangle, \\
|-1/2,-1/2,+1/2\rangle &= f_\downarrow^\dagger \xi_{p\downarrow}^\dagger \xi_{q\downarrow} |\psi_0\rangle, \\
|-1/2,-1/2,-1/2\rangle &= f_\downarrow^\dagger \xi_{p\downarrow}^\dagger \xi_{q\uparrow} |\psi_0\rangle.
\end{aligned} \tag{A.27}$$

Using the representation of total spin S^{tot}, we can separate the space into two pieces: $S^{tot} = 3/2$ and $S^{tot} = 1/2$. We focus on the subspace for $S^{tot} = 1/2$ and $S_z^{tot} = 1/2$, which is spanned with a basis,

$$\begin{aligned}
|\phi_1\rangle &= \frac{1}{\sqrt{2}} f_\uparrow^\dagger (\xi_{p\uparrow}^\dagger \xi_{q\uparrow} + \xi_{p\downarrow}^\dagger \xi_{q\downarrow}) |\psi_0\rangle \\
|\phi_2\rangle &= \frac{1}{\sqrt{6}} f_\uparrow^\dagger (\xi_{p\uparrow}^\dagger \xi_{q\uparrow} - \xi_{p\downarrow}^\dagger \xi_{q\downarrow}) |\psi_0\rangle + \frac{2}{\sqrt{6}} f_\downarrow^\dagger \xi_{p\uparrow}^\dagger \xi_{q\downarrow} |\psi_0\rangle
\end{aligned} \tag{A.28}$$

Figure A.3 shows a flow diagram of soft-gap Anderson model with $r = 0.35$, $\Delta = 0.4754 \times 10^{-3}$, and $U = -2\varepsilon_f = 10^{-3}$. Data are collected for quantum numbers $Q = 0$ and $S = 1/2$. For $\Delta < \Delta_c$, many-particle levels flow into the local moment fixed point.

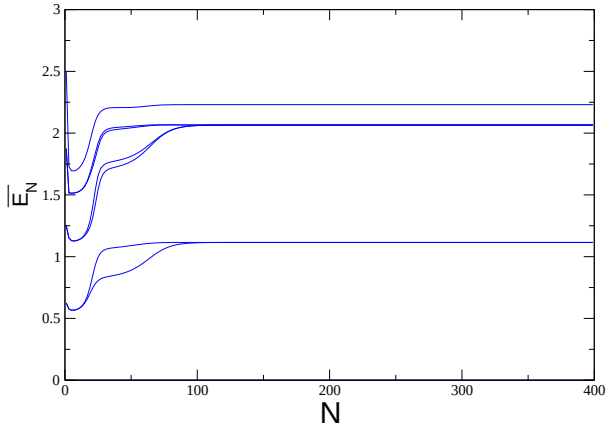

Figure A.3: Flow diagram of the lowest lying excitations for the local moment fixed points of the particle-hole symmetric soft-gap Anderson model ($r = 0.35$, $\Delta = 0.4754 \times 10^{-3}$ and $U = -2\varepsilon_f = 10^{-3}$). $(Q, S) = (0, 1/2)$.

Diagonalizing the single-particle Hamiltonian for the conduction-band [Eq. (A.11)] yields one-particle eigenvalues, $\epsilon_1 = 0.55$ and $\epsilon_3 = 1.50$, which correspond to the level-spacing in Fig. A.3.

$$\begin{aligned} E_1 &= \epsilon_1 - \epsilon_{-1} = 2\epsilon_1 \sim 1.1 \\ E_2 &= \epsilon_3 - \epsilon_{-1} = \epsilon_1 - \epsilon_{-3} = \epsilon_3 + \epsilon_1 \sim 2.05. \end{aligned} \tag{A.29}$$

The first two levels with $E = E_1 \sim 1.1$ are degenerate for the spin degrees of freedom and the eigenstates are

$$\begin{aligned} |\psi_1\rangle &= \frac{1}{\sqrt{2}} f_\uparrow^\dagger (\xi_{1\uparrow}^\dagger \xi_{-1\uparrow} + \xi_{1\downarrow}^\dagger \xi_{-1\downarrow})|\psi_0\rangle, \\ |\psi_2\rangle &= \frac{1}{\sqrt{6}} f_\uparrow^\dagger (\xi_{1\uparrow}^\dagger \xi_{-1\uparrow} - \xi_{1\downarrow}^\dagger \xi_{-1\downarrow})|\psi_0\rangle + \frac{2}{\sqrt{6}} f_\downarrow^\dagger \xi_{1\uparrow}^\dagger \xi_{-1\downarrow}|\psi_0\rangle. \end{aligned} \tag{A.30}$$

The degeneracy is doubled in the case of $E = E_2 \sim 2.05$, where the positions of a particle and a hole creates different states without any energy-cost [$(p, q) = (1, -3) \to (3, -1)$]. The eigenstates are

$$\begin{aligned} |\psi_3\rangle &= \frac{1}{\sqrt{2}} f_\uparrow^\dagger (\xi_{1\uparrow}^\dagger \xi_{-3\uparrow} + \xi_{1\downarrow}^\dagger \xi_{-3\downarrow})|\psi_0\rangle, \\ |\psi_4\rangle &= \frac{1}{\sqrt{6}} f_\uparrow^\dagger (\xi_{1\uparrow}^\dagger \xi_{-3\uparrow} - \xi_{1\downarrow}^\dagger \xi_{-3\downarrow})|\psi_0\rangle + \frac{2}{\sqrt{6}} f_\downarrow^\dagger \xi_{1\uparrow}^\dagger \xi_{-3\downarrow}|\psi_0\rangle, \\ |\psi_5\rangle &= \frac{1}{\sqrt{2}} f_\uparrow^\dagger (\xi_{3\uparrow}^\dagger \xi_{-1\uparrow} + \xi_{3\downarrow}^\dagger \xi_{-1\downarrow})|\psi_0\rangle, \\ |\psi_6\rangle &= \frac{1}{\sqrt{6}} f_\uparrow^\dagger (\xi_{3\uparrow}^\dagger \xi_{-1\uparrow} - \xi_{3\downarrow}^\dagger \xi_{-1\downarrow})|\psi_0\rangle + \frac{2}{\sqrt{6}} f_\downarrow^\dagger \xi_{3\uparrow}^\dagger \xi_{-1\downarrow}|\psi_0\rangle. \end{aligned} \tag{A.31}$$

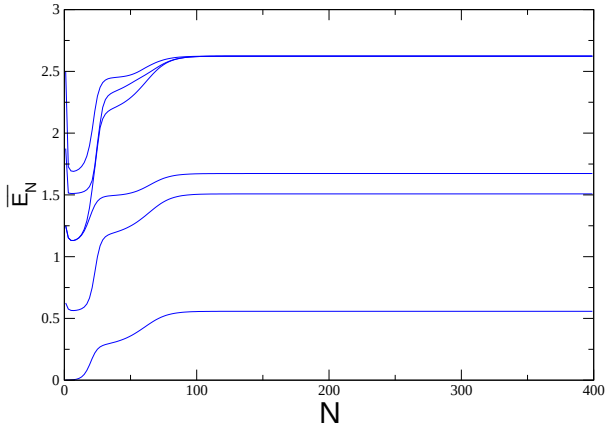

Figure A.4: Flow diagram of the lowest lying excitations for the local moment fixed points of the particle-hole symmetric soft-gap Anderson model: $r = 0.01$, $\Delta << \Delta_c$, $U = -2\varepsilon_f = 10^{-3}$, and $(Q, S) = (-1, 0)$.

Other higher excitations involving only single pair of a particle and a hole can be understood in similar manners. The alternative way to proceed to the higher levels is to create more particle-hole pairs from the ground state.

$$\begin{aligned} |\phi\rangle_{2-ph} &= \xi^\dagger_{p\mu}\xi_{q\nu}\xi^\dagger_{p'\mu}\xi_{q'\nu}|\psi_0\rangle,\ E = \epsilon_p - \epsilon_q + \epsilon_{p'} - \epsilon_{q'} \\ |\phi\rangle_{3-ph} &= \xi^\dagger_{p\mu}\xi_{q\nu}\xi^\dagger_{p'\mu}\xi_{q'\nu}\xi^\dagger_{p''\mu}\xi_{q''\nu}|\psi_0\rangle,\ E = \epsilon_p - \epsilon_q + \epsilon_{p'} - \epsilon_{q'} + \epsilon_{p''} - \epsilon_{q''} \\ &\cdots \end{aligned} \tag{A.32}$$

More number of $p-h$ pairs demand more efforts to obtain the eigenstates, which has the Clebsch-Gordan coefficients for higher spins $S^{tot} = 3/2,\ 2, \cdots$.

A.1.2 $Q = -1$ and $S = 0$

There is no change at the impurity-site, and the negative charge $Q = -1$ is attributed to the conduction-electron part,

$$\begin{aligned} |\phi_1\rangle &= \xi_{p\mu} f^\dagger_\sigma |\psi_0\rangle, \\ |\phi_2\rangle &= \xi_{p\mu}\xi^\dagger_{p'\mu'}\xi_{q'\nu'} f^\dagger_\sigma |\psi_0\rangle, \\ |\phi_3\rangle &= \xi_{p\mu}\xi^\dagger_{p'\mu'}\xi_{q'\nu'}\xi^\dagger_{p''\mu''}\xi_{q''\nu''} f^\dagger_\sigma |\psi_0\rangle, \\ &\cdots \end{aligned} \tag{A.33}$$

with

$$|\psi_0\rangle = |0\rangle_{imp} \otimes \Big[\prod_{p<0} \xi^\dagger_{p\uparrow}\xi^\dagger_{p\downarrow}|0\rangle_{cond}\Big]. \tag{A.34}$$

Concerning the simplest case of $|\phi_1\rangle$, the singlet state is given as:

$$|\psi\rangle = \frac{1}{\sqrt{2}}(\xi_{p\uparrow}f^\dagger_\uparrow + \xi_{p\downarrow}f^\dagger_\downarrow)|\psi_0\rangle, \tag{A.35}$$

with which the lowest two levels in Fig. A.4 are written as:

$$\begin{aligned} |\psi_1\rangle &= \frac{1}{\sqrt{2}}(\xi_{-1\uparrow}f^\dagger_\uparrow + \xi_{-1\downarrow}f^\dagger_\downarrow)|\psi_0\rangle, \\ |\psi_2\rangle &= \frac{1}{\sqrt{2}}(\xi_{-2\uparrow}f^\dagger_\uparrow + \xi_{-2\downarrow}f^\dagger_\downarrow)|\psi_0\rangle. \end{aligned} \tag{A.36}$$

The eigenenergy of the two levels are $E_1 = 1.10$ and $E_2 = 2.05$, which agree with the corresponding single-particle eigenenergy, $|\epsilon_{-1}| = 1.10$ and $|\epsilon_{-2}| = 2.05$, respectively. The third level involves two holes and one electron in the conduction-electrons part and the excitation-energy is $E_3 = \epsilon_1 - 2\epsilon_{-1} = 3\epsilon_1$:

$$|\phi\rangle = f^\dagger_\sigma \xi^\dagger_{1\mu}\xi_{-1\uparrow}\xi_{-1\downarrow}|\psi_0\rangle. \tag{A.37}$$

Since $\langle\psi_0|\xi^\dagger_{-1\downarrow}\xi^\dagger_{-1\uparrow}S^{tot}\xi_{-1\uparrow}\xi_{-1\downarrow}|\psi_0\rangle = 0$, two particles $f^\dagger_\nu$ and $\xi^\dagger_{1\mu}$ form a single state as in Eq. (A.35) to make $S^{tot} = 0$:

$$|\psi_3\rangle = \frac{1}{\sqrt{2}}(\xi^\dagger_{1\uparrow}f^\dagger_\downarrow + \xi^\dagger_{1\downarrow}f^\dagger_\uparrow)\xi_{-1\uparrow}\xi_{-1\downarrow}|\psi_0\rangle. \tag{A.38}$$

The highest three levels in Fig. A.4 are degenerate at $E = 2\epsilon_1 + \epsilon_2$. The degeneracy is resolved with a 4-spins picture, where $f^\dagger_\sigma$, $\xi^\dagger_{p\mu}$, $\xi_{q\nu}$, and $\xi_{r\delta}$ are considered as ordinary particles with spin-1/2. There are two ways of distributing the holes ($\xi_{q\nu}$ and $\xi_{r\delta}$) and the particle ($\xi^\dagger_{p\mu}$) in the single-particle levels:

$$\begin{aligned} |\phi_1\rangle &= f^\dagger_\sigma\xi^\dagger_{3\mu}\xi_{-1\uparrow}\xi_{-1\downarrow}|\psi_0\rangle, \\ |\phi_2\rangle &= f^\dagger_\sigma\xi^\dagger_{1\mu}\xi_{-1\nu}\xi_{-3\delta}|\psi_0\rangle. \end{aligned} \tag{A.39}$$

The first state, $|\phi_1\rangle$, is similar to the case with $E = 3\epsilon_1$ in Eq. (A.37) so that the eigenstate for $S^{tot} = 0$ is

$$|\psi_4\rangle = \frac{1}{\sqrt{2}}(\xi^\dagger_{3\uparrow}f^\dagger_\downarrow + \xi^\dagger_{3\downarrow}f^\dagger_\uparrow)\xi_{-1\uparrow}\xi_{-1\downarrow}|\psi_0\rangle. \tag{A.40}$$

To determine the spins of the the second state ($|\phi_2\rangle$), we calculate the Clebsh-Gordan coefficients $c^{S,S_z}_{\sigma\mu\nu\delta}$, defined as

$$|S,S_z\rangle^{\sigma\mu\nu\delta} = \sum_{\sigma,\mu,\nu,\delta} c^{S,S_z}_{\sigma\mu\nu\delta}|\sigma,\mu,\nu,\delta\rangle. \tag{A.41}$$

Using the expression of a three-spins state:

$$|S,S_z\rangle^{\mu\nu\delta} = \sum_{\mu,\nu,\delta} c^{S,S_z}_{\mu\nu\delta}|\mu,\nu,\delta\rangle, \tag{A.42}$$

a four-spin singlet state $|0,0\rangle^{\sigma\mu\nu\delta}$ is written as

$$|0,0\rangle^{\sigma\mu\nu\delta} = \frac{1}{\sqrt{2}}(f_\uparrow^\dagger|1/2,-1/2\rangle^{\mu\nu\delta} - f_\downarrow^\dagger|1/2,+1/2\rangle^{\mu\nu\delta}). \tag{A.43}$$

The coefficients $c_{\mu\nu\delta}^{1/2,\pm1/2}$ are same as in Eq. (A.28):

$$\begin{aligned}
|1/2,+1/2\rangle_1^{\mu\nu\delta} &= \frac{1}{\sqrt{2}}\xi_{1\uparrow}^\dagger(\xi_{-1\uparrow}^\dagger\xi_{-3\uparrow} + \xi_{-1\downarrow}^\dagger\xi_{-3\downarrow})|\psi_0\rangle,\\
|1/2,-1/2\rangle_1^{\mu\nu\delta} &= \frac{1}{\sqrt{2}}\xi_{1\downarrow}^\dagger(\xi_{-1\uparrow}^\dagger\xi_{-3\uparrow} + \xi_{-1\downarrow}^\dagger\xi_{-3\downarrow})|\psi_0\rangle,\\
|1/2,+1/2\rangle_2^{\mu\nu\delta} &= \frac{1}{\sqrt{6}}\xi_{1\uparrow}^\dagger(\xi_{-1\uparrow}^\dagger\xi_{-3\uparrow} - \xi_{-1\downarrow}^\dagger\xi_{-3\downarrow})|\psi_0\rangle + \frac{2}{\sqrt{6}}\xi_{1\downarrow}^\dagger\xi_{-1\uparrow}^\dagger\xi_{-3\downarrow}|\psi_0\rangle,\\
|1/2,-1/2\rangle_2^{\mu\nu\delta} &= \frac{1}{\sqrt{6}}\xi_{1\downarrow}^\dagger(\xi_{-1\uparrow}^\dagger\xi_{-3\uparrow} - \xi_{-1\downarrow}^\dagger\xi_{-3\downarrow})|\psi_0\rangle + \frac{2}{\sqrt{6}}\xi_{1\uparrow}^\dagger\xi_{-1\downarrow}^\dagger\xi_{-3\uparrow}|\psi_0\rangle.
\end{aligned} \tag{A.44}$$

Inserting Eq. (A.44) into Eq. (A.43), we obtain

$$\begin{aligned}
|0,0\rangle_1^{\sigma\mu\nu\delta} &= \frac{1}{2}(f_\uparrow^\dagger\xi_{1\downarrow}^\dagger - f_\downarrow^\dagger\xi_{1\uparrow}^\dagger)(\xi_{-1\uparrow}^\dagger\xi_{-3\uparrow} + \xi_{-1\downarrow}^\dagger\xi_{-3\downarrow})|\psi_0\rangle\\
|0,0\rangle_2^{\sigma\mu\nu\delta} &= \frac{1}{2\sqrt{3}}(f_\uparrow^\dagger\xi_{1\downarrow}^\dagger - f_\downarrow^\dagger\xi_{1\uparrow}^\dagger)(\xi_{-1\uparrow}^\dagger\xi_{-3\uparrow} - \xi_{-1\downarrow}^\dagger\xi_{-3\downarrow})|\psi_0\rangle\\
&\quad + \frac{1}{\sqrt{3}}(f_\uparrow^\dagger\xi_{1\uparrow}^\dagger\xi_{-1\downarrow}^\dagger\xi_{-3\uparrow} - f_\downarrow^\dagger\xi_{1\downarrow}^\dagger\xi_{-1\uparrow}^\dagger\xi_{-3\downarrow})|\psi_0\rangle.
\end{aligned} \tag{A.45}$$

Three-fold degeneracy at $E = \epsilon_1 + \epsilon_3$ is now explained with Eq. (A.45) and Eq. (A.40):

$$\begin{aligned}
|\psi_4\rangle &= \frac{1}{\sqrt{2}}(\xi_{3\uparrow}^\dagger f_\downarrow^\dagger + \xi_{3\downarrow}^\dagger f_\uparrow^\dagger)\xi_{-1\uparrow}\xi_{-1\downarrow}|\psi_0\rangle,\\
|\psi_5\rangle &= \frac{1}{2}(f_\uparrow^\dagger\xi_{1\downarrow}^\dagger - f_\downarrow^\dagger\xi_{1\uparrow}^\dagger)(\xi_{-1\uparrow}^\dagger\xi_{-3\uparrow} + \xi_{-1\downarrow}^\dagger\xi_{-3\downarrow})|\psi_0\rangle,\\
|\psi_6\rangle &= \frac{1}{2\sqrt{3}}(f_\uparrow^\dagger\xi_{1\downarrow}^\dagger - f_\downarrow^\dagger\xi_{1\uparrow}^\dagger)(\xi_{-1\uparrow}^\dagger\xi_{-3\uparrow} - \xi_{-1\downarrow}^\dagger\xi_{-3\downarrow})|\psi_0\rangle\\
&\quad + \frac{1}{\sqrt{3}}(f_\uparrow^\dagger\xi_{1\uparrow}^\dagger\xi_{-1\downarrow}^\dagger\xi_{-3\uparrow} - f_\downarrow^\dagger\xi_{1\downarrow}^\dagger\xi_{-1\uparrow}^\dagger\xi_{-3\downarrow})|\psi_0\rangle.
\end{aligned} \tag{A.46}$$

A.2 Details of the Perturbative Analysis around the Local Moment Fixed Point

In this Appendix, we want to give more details for the derivation of the matrix W_{ij} in Eq. (4.28) which determines the splitting of the fourfold degeneracy of the subspace ($Q = 0$, $S = 1/2$, $S_z = 1/2$) of the LM fixed point at energy $\epsilon_1 + \epsilon_3$. We focus on the matrix element W_{12}:

$$W_{12} = \langle\psi_1|H_N'|\psi_2\rangle = \alpha(r)f(N)\,\langle\psi_1|\vec{S}_{\rm imp}\cdot\vec{s}_0|\psi_2\rangle\ .$$

The strategy for the calculations can be extended to the other matrix elements and the other subspaces, for which we add the perturbative results at the end of this appendix without derivation. The operator $\vec{S}_{\rm imp} \cdot \vec{s}_0$ is decomposed into four parts:

$$\begin{aligned} \vec{S}_{\rm imp} \cdot \vec{s}_0 &= \frac{1}{2} S^+_{\rm imp} c^\dagger_{0\downarrow} c_{0\uparrow} + \frac{1}{2} S^-_{\rm imp} c^\dagger_{0\uparrow} c_{0\downarrow} \\ &\quad + \frac{1}{2} S^z_{\rm imp} \left(c^\dagger_{0\uparrow} c_{0\uparrow} - c^\dagger_{0\downarrow} c_{0\downarrow} \right) \ , \end{aligned} \tag{A.47}$$

so that W_{12} can be written as

$$W_{12} = \alpha(r) f(N) \, \frac{1}{2} \left[\mathrm{I} + \mathrm{II} + \mathrm{III} - \mathrm{IV} \right] \ ,$$

with

$$\mathrm{I} = \langle \psi_1 | S^+_{\rm imp} c^\dagger_{0\downarrow} c_{0\uparrow} | \psi_2 \rangle \ ,$$

and the other terms accordingly. With the definitions of $|\psi_1\rangle$ and $|\psi_2\rangle$ of Eq. (4.26) we have:

$$\begin{aligned} \mathrm{I} &= \frac{1}{\sqrt{2}} \langle \psi_0 | \left(\xi^\dagger_{-3\uparrow} \xi_{1\uparrow} + \xi^\dagger_{-3\downarrow} \xi_{1\downarrow} \right) f_\uparrow S^+_{\rm imp} c^\dagger_{0\downarrow} c_{0\uparrow} \\ &\quad \times \left[\frac{1}{\sqrt{6}} f^\dagger_\uparrow \left(\xi^\dagger_{1\uparrow} \xi_{-3\uparrow} - \xi^\dagger_{1\downarrow} \xi_{-3\downarrow} \right) + \frac{2}{\sqrt{6}} f^\dagger_\downarrow \xi^\dagger_{1\uparrow} \xi_{-3\downarrow} \right] |\psi_0\rangle \ . \end{aligned} \tag{A.48}$$

With $S^+_{\rm imp} = f^\dagger_\uparrow f_\downarrow$ we immediately see that the terms containing $f_\uparrow S^+_{\rm imp} f^\dagger_\uparrow$ drop out. The remaining impurity operators, $f_\uparrow S^+_{\rm imp} f^\dagger_\downarrow$, give unity when acting on $|\psi_0\rangle$, so one arrives at

$$\mathrm{I} = \frac{1}{\sqrt{3}} \left[\mathrm{Ia} + \mathrm{Ib} \right] \ ,$$

with

$$\begin{aligned} \mathrm{Ia} &= \langle \psi_0 | \xi^\dagger_{-3\uparrow} \xi_{1\uparrow} c^\dagger_{0\downarrow} c_{0\uparrow} \xi^\dagger_{1\uparrow} \xi_{-3\downarrow} | \psi_0 \rangle \\ \mathrm{Ib} &= \langle \psi_0 | \xi^\dagger_{-3\downarrow} \xi_{1\downarrow} c^\dagger_{0\downarrow} c_{0\uparrow} \xi^\dagger_{1\uparrow} \xi_{-3\downarrow} | \psi_0 \rangle \ . \end{aligned} \tag{A.49}$$

To analyze Ia and Ib, the operators $c^{(\dagger)}_{0\sigma}$ have to be expressed in terms of the operators $\xi^{(\dagger)}_{p\sigma}$:

$$c_{0\sigma} = \sum_{p'} \alpha_{0p'} \xi_{p'\sigma} \quad , \quad c^\dagger_{0\sigma} = \sum_p \alpha^*_{0p} \xi^\dagger_{p\sigma} \ , \tag{A.50}$$

with the sums over p and p' defined in Eq. (4.21). This gives

$$\mathrm{Ia} = \sum_{pp'} \alpha^*_{0p} \alpha_{0p'} \langle \psi_0 | \xi^\dagger_{-3\uparrow} \xi_{1\uparrow} \xi^\dagger_{p\downarrow} \xi_{p'\uparrow} \xi^\dagger_{1\uparrow} \xi_{-3\downarrow} | \psi_0 \rangle \ . \tag{A.51}$$

The only non-zero matrix element of Eq. (A.51) is for $p = p' = -3$:

$$\begin{aligned} \text{Ia} &= \alpha^*_{0-3}\alpha_{0-3}\langle\psi_0|\xi^\dagger_{-3\uparrow}\xi_{1\uparrow}\xi^\dagger_{-3\downarrow}\xi_{-3\uparrow}\xi^\dagger_{1\uparrow}\xi_{-3\downarrow}|\psi_0\rangle \\ &= -|\alpha_{0-3}|^2 \ . \end{aligned} \tag{A.52}$$

Similarly, the term Ib gives

$$\begin{aligned} \text{Ib} &= \sum_{pp'}\alpha^*_{0p}\alpha_{0p'}\langle\psi_0|\xi^\dagger_{-3\downarrow}\xi_{1\downarrow}\xi^\dagger_{p\downarrow}\xi_{p'\uparrow}\xi^\dagger_{1\uparrow}\xi_{-3\downarrow}|\psi_0\rangle \\ &= |\alpha_{01}|^2 \ , \end{aligned} \tag{A.53}$$

so that, in total,

$$\text{I} = \frac{1}{\sqrt{3}}\left[-|\alpha_{0-3}|^2 + |\alpha_{01}|^2\right] \ . \tag{A.54}$$

The next term $\text{II} = \langle\psi_1|S^-_{\rm imp}c^\dagger_{0\uparrow}c_{0\downarrow}|\psi_2\rangle$ gives zero due to the combination of impurity operators: $f_\uparrow f^\dagger_\downarrow f_\uparrow \ldots$ with $f_\uparrow$ from $\langle\psi_1|$ and $f^\dagger_\downarrow f_\uparrow = S^-_{\rm imp}$.

The third term $\text{III} = \langle\psi_1|S^z_{\rm imp}c^\dagger_{0\uparrow}c_{0\uparrow}|\psi_2\rangle$ gives

$$\begin{aligned} \text{III} &= \frac{1}{\sqrt{12}}\langle\psi_0|\left(\xi^\dagger_{-3\uparrow}\xi_{1\uparrow} + \xi^\dagger_{-3\downarrow}\xi_{1\downarrow}\right) f_\uparrow S^z_{\rm imp}c^\dagger_{0\uparrow}c_{0\uparrow}f^\dagger_\uparrow \\ &\quad \times\left(\xi^\dagger_{1\uparrow}\xi_{-3\uparrow} - \xi^\dagger_{1\downarrow}\xi_{-3\downarrow}\right)|\psi_0\rangle \ , \end{aligned}$$

where the term with $(2/\sqrt{6})f^\dagger_\downarrow\xi^\dagger_{1\uparrow}\xi_{-3\downarrow}$ from $|\psi_2\rangle$ has already been dropped. So we are left with four terms

$$\text{III} = \frac{1}{\sqrt{12}}\left[\text{IIIa} - \text{IIIb} + \text{IIIc} - \text{IIId}\right] \ , \tag{A.55}$$

with

$$\begin{aligned} \text{IIIa} &= \langle\psi_0|\xi^\dagger_{-3\uparrow}\xi_{1\uparrow}f_\uparrow S^z_{\rm imp}c^\dagger_{0\uparrow}c_{0\uparrow}f^\dagger_\uparrow\xi^\dagger_{1\uparrow}\xi_{-3\uparrow}|\psi_0\rangle \ , \\ \text{IIIb} &= \langle\psi_0|\xi^\dagger_{-3\uparrow}\xi_{1\uparrow}f_\uparrow S^z_{\rm imp}c^\dagger_{0\uparrow}c_{0\uparrow}f^\dagger_\uparrow\xi^\dagger_{1\downarrow}\xi_{-3\downarrow}|\psi_0\rangle \ , \\ \text{IIIc} &= \langle\psi_0|\xi^\dagger_{-3\downarrow}\xi_{1\downarrow}f_\uparrow S^z_{\rm imp}c^\dagger_{0\uparrow}c_{0\uparrow}f^\dagger_\uparrow\xi^\dagger_{1\uparrow}\xi_{-3\uparrow}|\psi_0\rangle \ , \\ \text{IIId} &= \langle\psi_0|\xi^\dagger_{-3\downarrow}\xi_{1\downarrow}f_\uparrow S^z_{\rm imp}c^\dagger_{0\uparrow}c_{0\uparrow}f^\dagger_\uparrow\xi^\dagger_{1\downarrow}\xi_{-3\downarrow}|\psi_0\rangle \ . \end{aligned} \tag{A.56}$$

Following similar arguments as above one obtains

$$\text{IIIa} = \frac{1}{2}{\sum_p}'|\alpha_{0p}|^2 \ , \tag{A.57}$$

where the p in ${\sum_p}'$ takes the values

$$p = 1, -1, -5, -7, \ldots - N.$$

Then we obtain:

$$\mathrm{IIIb} = \mathrm{IIIc} = 0 \ , \tag{A.58}$$

and

$$\mathrm{IIId} = \frac{1}{2}{\sum_p}'' |\alpha_{0p}|^2 \ , \tag{A.59}$$

where the p in ${\sum_p}''$ takes the values

$$p = -1, -3, -5, -7, \ldots - N \ .$$

This gives for the third term

$$\begin{aligned} \mathrm{III} &= \frac{1}{\sqrt{12}} \left[\mathrm{IIIa} - \mathrm{IIId}\right] \\ &= \frac{1}{4\sqrt{3}} \left[{\sum_p}' |\alpha_{0p}|^2 - {\sum_p}'' |\alpha_{0p}|^2 \right] \\ &= \frac{1}{4\sqrt{3}} \left[|\alpha_{01}|^2 - |\alpha_{0-3}|^2 \right] \ . \end{aligned} \tag{A.60}$$

The calculation of IV proceeds very similarly to III and one obtains

$$\mathrm{III} = -\mathrm{IV} \ , \tag{A.61}$$

so that we finally arrive at

$$\begin{aligned} W_{12} &= \alpha(r) f(N) \frac{1}{2} \left(|\alpha_{01}|^2 - |\alpha_{0-3}|^2 \right) \left[\frac{1}{\sqrt{3}} + 0 + 2 \frac{1}{4\sqrt{3}} \right] \\ &= \alpha(r) f(N) \frac{1}{4} \sqrt{3} \left(|\alpha_{01}|^2 - |\alpha_{0-3}|^2 \right) \ . \end{aligned} \tag{A.62}$$

We performed a similar analysis for a couple of other subspaces. Here we list the results from the perturbative analysis for three more subspaces together with the corresponding basis states.

A.2.1 $Q = 0$, $S = 1/2$, $S_z = 1/2$, $E = 2\epsilon_1$

This subspace has the same quantum numbers Q, S, and S_z as the one discussed above, so that the details of the calculation are very similar. The differences originate from the position of particles and holes in the single-particle spectrum, which reduces the dimensionality of the subspace from four to two.

The corresponding basis can be written as

$$\begin{aligned} |\psi_1\rangle &= \frac{1}{\sqrt{2}} f_\uparrow^\dagger (\xi_{1\uparrow}^\dagger \xi_{-1\uparrow} + \xi_{1\downarrow}^\dagger \xi_{-1\downarrow}) |\psi_0\rangle \ , \\ |\psi_2\rangle &= \left[\frac{1}{\sqrt{6}} f_\uparrow^\dagger (\xi_{1\uparrow}^\dagger \xi_{-1\uparrow} - \xi_{1\downarrow}^\dagger \xi_{-1\downarrow}) + \frac{2}{\sqrt{6}} f_\downarrow^\dagger \xi_{1\uparrow}^\dagger \xi_{-1\downarrow} \right] |\psi_0\rangle \ . \end{aligned} \tag{A.63}$$

The first-order corrections are given by the 2×2 matrix

$$\{W_{ij}\} = \alpha(r)f(N)\begin{bmatrix} 0 & \frac{\sqrt{3}}{4}\gamma \\ \frac{\sqrt{3}}{4}\gamma & -\frac{1}{2}\beta \end{bmatrix} , \tag{A.64}$$

with $\gamma = |\alpha_{01}|^2 - |\alpha_{0-1}|^2$ and $\beta = |\alpha_{01}|^2 + |\alpha_{0-1}|^2$. Due to the particle-hole symmetry of the conduction band we have $|\alpha_{01}| = |\alpha_{0-1}|$; therefore, the off-diagonal matrix elements vanish and the effect of the perturbation is simply a negative energy-shift only for the state $|\psi_2\rangle$:

$$\{W_{ij}\} = \alpha(r)f(N)\begin{bmatrix} 0 & 0 \\ 0 & -|\alpha_{01}|^2 \end{bmatrix} . \tag{A.65}$$

This effect can be seen in the energy splitting of the first two low-lying excitations in Fig. 4.7.

A.2.2 $Q = -1$, $S = 0$, $E = -\epsilon_{-1}$

There is only one configuration for this combination of quantum numbers and excitation energy:

$$|\psi\rangle = \frac{1}{\sqrt{2}}(f^\dagger_\uparrow \xi_{-1\uparrow} + f^\dagger_\downarrow \xi_{-1\downarrow})|\psi_0\rangle . \tag{A.66}$$

The first-order perturbation keeps the state in this one-dimensional subspace and the energy correction is given by

$$\Delta E = \langle\psi|H'_N|\psi\rangle = -\frac{3}{4}\alpha(r)f(N)|\alpha_{0-1}|^2 . \tag{A.67}$$

A.2.3 $Q = -1$, $S = 0$, $E = -\epsilon_{-3}$

The difference to the previous case is the position of the hole in the single-particle spectrum. The state is now given by

$$|\psi\rangle = \frac{1}{\sqrt{2}}(f^\dagger_\uparrow \xi_{-3\uparrow} + f^\dagger_\downarrow \xi_{-3\downarrow})|\psi_0\rangle , \tag{A.68}$$

with the energy correction

$$\Delta E = \langle\psi|H'_N|\psi\rangle = -\frac{3}{4}\alpha(r)f(N)|\alpha_{0-3}|^2 . \tag{A.69}$$

A.3 Details of the Perturbative Analysis around the Strong Coupling Fixed Point

The main difference in the calculation of the matrix elements $\{W_{ij}\}$ for this case is due to the structure of the perturbation [see Eq. (A.10)]. Furthermore, the ground state of the SC fixed point is fourfold degenerate and the perturbation partially splits this degeneracy, as discussed in the following.

A.3.1 $Q = 0,\ S = 1/2,\ S_z = 1/2,\ E = 0$

This is one of the four degenerate ground states at the SC fixed point:

$$|\psi_1\rangle = \xi^\dagger_{0\uparrow}|\psi_0\rangle \ , \tag{A.70}$$

with $|\psi_0\rangle$ defined in Eq. (A.25). The perturbative correction is given by

$$\langle\psi_1|H'_N|\psi_1\rangle = \frac{1}{2}\beta(r)\bar{f}(N)(1-|\alpha_{f0}|^4), \tag{A.71}$$

which corresponds to the energy shift of the ground state:

$$\Delta E_1 = \frac{1}{2}\beta(r)\bar{f}(N)(1-|\alpha_{f0}|^4) \ . \tag{A.72}$$

The coefficients α_{fl} are defined by the relation between the operators $f^{(\dagger)}_\sigma$ and $\xi^{(\dagger)}_{l\sigma}$:

$$f_\sigma = \sum_{l'} \alpha_{fl'}\xi_{l'\sigma} \quad , \quad f^\dagger_\sigma = \sum_{l} \alpha^*_{fl}\xi^\dagger_{l\sigma} \ . \tag{A.73}$$

A.3.2 $Q = -1,\ S = 0,\ E = 0$

This state is also a ground state in the $U = 0$ case:

$$|\psi_2\rangle = |\psi_0\rangle \ . \tag{A.74}$$

The calculation of the first-order correction for $|\psi_2\rangle$ gives

$$\langle\psi_2|H'_N|\psi_2\rangle = \frac{1}{2}\beta(r)\bar{f}(N)(1+|\alpha_{f0}|^4) \ . \tag{A.75}$$

This means that the ground state including the effect of the perturbation is given by $|\psi_1\rangle$ in Eq. (A.70) and the state $|\psi_2\rangle$ appears as an excited state. For a comparison with the energy levels shown in the NRG flow diagrams, where the ground state energy is set to zero in each iteration, we subtract the perturbative correction of the ground state (ΔE_1) from the energies of all other excited states. Subtracting this energy shift from Eq. (A.75) gives the net energy correction for the $|\psi_2\rangle$ state:

$$\Delta E_2 = \beta(r)\bar{f}(N)|\alpha_{f0}|^4 \ . \tag{A.76}$$

A.3.3 $Q = -1,\ S = 0,\ E = \epsilon_2$

The state corresponding to this subspace is given by

$$|\psi_3\rangle = \frac{1}{\sqrt{2}}(\xi^\dagger_{0\uparrow}\xi_{-2\uparrow} + \xi^\dagger_{0\downarrow}\xi_{-2\downarrow})|\psi_0\rangle \ . \tag{A.77}$$

The first-order correction reads

$$\langle\psi_3|H'_N|\psi_3\rangle = \beta(r)\bar{f}(N)\left[\frac{1}{2}(1-|\alpha_{f0}|^4) + 3|\alpha_{f0}|^2|\alpha_{f-2}|^2\right] \ . \tag{A.78}$$

Subtracting the energy correction for the ground state results in

$$\Delta E_3 = 3\beta(r)\bar{f}(N)|\alpha_{f0}|^2|\alpha_{f-2}|^2 \ . \tag{A.79}$$

A.3.4 $Q = -1,\ S = 0,\ E = \epsilon_4$

Similarly for the state

$$|\psi_4\rangle = \frac{1}{\sqrt{2}}(\xi^\dagger_{0\uparrow}\xi_{-4\uparrow} + \xi^\dagger_{0\downarrow}\xi_{-4\downarrow})|\psi_0\rangle \ , \tag{A.80}$$

the first-order correction is given by

$$\langle\psi_4|H'_N|\psi_4\rangle = \beta(r)\bar{f}(N)\left[\frac{1}{2}(1-|\alpha_{f0}|^4) + 3|\alpha_{f0}|^2|\alpha_{f-4}|^2\right] \ ,$$

and subtracting the energy correction for the ground state results in

$$\Delta E_4 = 3\beta(r)\bar{f}(N)|\alpha_{f0}|^2|\alpha_{f-4}|^2 \ . \tag{A.81}$$

B. THERMODYNAMICS IN THE OHMIC SPIN-BOSON MODEL

In this section, we describe how thermodynamic quantities can be extracted from the flow of many-particle levels $E_N(r)$, which are calculated with the bosonic NRG. Starting from the $E_N(r)$ there is no difference (from a technical point of view) between the fermionic and the bosonic case [for the fermionic cases see, for example, Refs. (Krishna-murthy, Wilson and Wilkins 1975, Oliveira and Oliveira 1994)]. Nevertheless, for completeness we include a brief discussion of the technical details here. We show results for the impurity contribution to the entropy and the specific heat in the Ohmic case. The Ohmic case has been studied in detail in Refs. (Costi 1998, Costi and Zarand 1999) [for earlier work on thermodynamic properties see Refs. (Leggett et al. 1987, Göhrlich and Weiss 1998, Sassetti and Weiss 1990)]. The agreement with the results from Refs. (Costi 1998, Costi and Zarand 1999) is excellent, which again confirms the reliability of the bosonic NRG for the investigation of quantum impurity models involving a bosonic bath. Consider the spectrum of many-particle energies E_i of a discretized version of the spin-boson model. The grand canonical partition function, $\mathcal{Z} = \mathrm{Tr}\ e^{-\beta(H-\mu N)}$, reduces to

$$\mathcal{Z} = \sum_i e^{-\beta E_i}, \tag{B.1}$$

as the chemical potential μ is set to zero [we are interested in gap-less spectral function $J(\omega)$]. Free energy F and entropy S are then given by

$$F = -T \ln \mathcal{Z} \text{ and } S = -\frac{\partial F}{\partial T}. \tag{B.2}$$

(We set $k_B = 1$.) The impurity contribution to the entropy is

$$S_{imp} = S - S_0 \tag{B.3}$$

where S is the entropy of the full system and S_0 the entropy of the system without impurity.

Before we discuss the full temperature dependence of $S_{imp}(T)$, let us focus on the value of S_{imp} at the localized and delocalized fixed points: $S_{imp,L}$ and $S_{imp,D}$. It is well known that $S_{imp,L} = \ln 2$ and $S_{imp,D} = 0$ (Costi 1998, Costi and Zarand 1999), but it might not be obvious that these values can be directly extracted from the many-particle spectra at the fixed points.

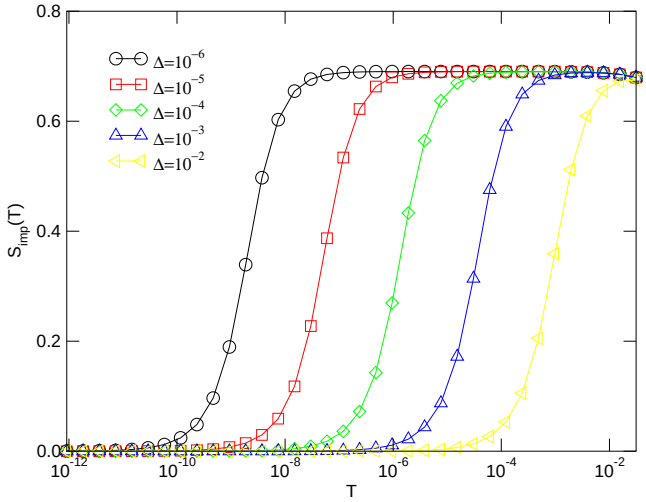

Figure B.1: Temperature dependence of the impurity contribution to the entropy, $S_{imp}(T)$, for α=1/3, $s = 1$ (Ohmic case), and various values of Δ.

In Section 5.2.1, we already showed that the fixed point spectrum of the delocalized fixed point is the same as the one of a free bosonic chain, which is nothing else but the system without impurity. This implies that for the delocalized fixed point

$$E_i = E_{i,0} + \Delta E, \tag{B.4}$$

with E_i ($E_{i,0}$) the many-particle energies of the system with (without) impurity and ΔE a constant shift independent of i. It is clear that this equation does not hold for all levels, it is only valid for energies sufficiently below the crossover scale to the fixed point.

Equation (B.4) directly leads to the proof of $S_{imp,D} = 0$: we have $\mathcal{Z}_D = \exp[\beta\Delta E]\,\mathcal{Z}_0$, and from this $F_L = -T\ln 2 + F_0 + \Delta E$ and $S_L = \ln 2 + S_0$, corresponding to $S_{imp,L} = 2$. From this discussion it follows that $S_{imp,L} = \ln 2$ and $S_{imp,D} = 0$ independent of the exponent s in the spectral function $J(\omega)$.

For any finite Δ and α, the values $S_{imp,L} = \ln 2$ and $S_{imp,D} = 0$ are strictly valid only in the limit $T \to 0$. Note that a proper definition of these zero-point entropies requires the correct order of limits: the thermodynamic limit has to be taken before the limit $T \to 0$. With the order of limits reversed, the zero-point entropy would be equal to $\ln d_g$, with d_g the degeneracy of the ground state. Although this happens to give the same values for $S_{imp,L}$ and $S_{imp,D}$ in the case studied here, this equivalence is not generally valid. This can be seen, for example, in the NRG calculations for the single-impurity Anderson model (Krishna-murthy

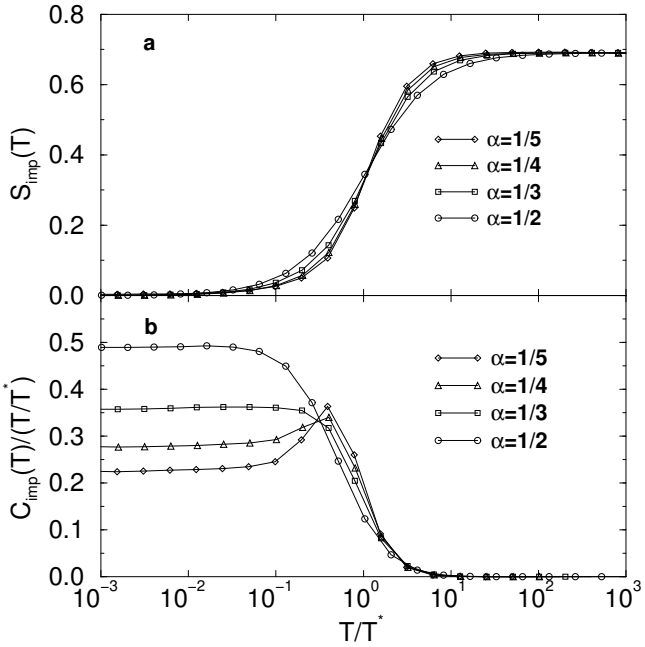

Figure B.2: (a) Scaling curves of the impurity contribution to the entropy, $S_{imp}(T)$, for $s = 1$ (Ohmic case), and various of α; (b) Scaling curves of the impurity contribution to the specific heat $C_{imp}(T)/(T/T^*)$, for the same parameters as in (a).

et al. 1980) where the degeneracy of the ground state oscillates between 1 for even and 4 for odd iterations when the system approaches the fixed point of a screened spin, which has $S_{imp} = 0$. Also, any non-trivial quantum critical fixed point is expected to have a residual entropy which is not $\ln d_g$ with integer d_g.

In the bosonic NRG, we do not have access to the full spectrum of many-particle energies E_i as used in Eq. B.1. Instead, the iterative procedure results in a sequence of many-particle energies $E_N(r)$ with iterative number N and $r = 1, ...N_s$. According to the discussion in Refs. (Wilson 1975, Krishna-murthy et al. 1980), each of the sets of many-particle energies is assumed to be a good description of the system for a certain temperature T_N with

$$T_N = x\omega_c\Lambda^{-N}, \tag{B.5}$$

with x a dimensionless constant of the order of 1, chosen such that T_N lies within the spectrum $E_N(r)$.

For each iteration step N, the partition function is calculated for the temper-

ature T_N:

$$\mathcal{Z}_N = \sum_r e^{-E_N(r)/T_N}. \tag{B.6}$$

In addition, the internal energy at iteration step N for the temperature T_N is calculated as

$$E_N = \frac{1}{\mathcal{Z}_N} \sum_r E_N(r) e^{-E_N(r)/T_N}. \tag{B.7}$$

This is the information we have for the numerical calculation of thermodynamic properties.

One possibility to proceed is to calculate the free energy $F_N = -T_N \ln \mathcal{Z}_N$ for each iteration step, and from this the entropy $S = -\partial F/\partial T$ via a discrete differentiation. This procedure has been shown to give good results in the fermionic case [see, for example, Ref. (Bulla and Hewson 1997)]. It requires, however, a precise calculation of the difference of the ground state energies between subsequent steps; this appears to introduce some errors in the calculations within the bosonic NRG.

Therefore, we use an alternative approach in which the entropy S_N at iteration step N for the temperature T_N is calculated via

$$S_N = \frac{E_N}{T_N} + \ln \mathcal{Z}_N. \tag{B.8}$$

This approach avoids the discrete differentiation, and does not require the knowledge of the ground state energies.

Let us now discuss the results for entropy and specific heat calculated with the bosonic NRG using the method just described. Figure B.1 shows the temperature dependence of the impurity contribution to the entropy, $S_{imp}(T)$, for $\alpha = 1/3$, $s = 1$ (Ohmic case), and various values of Δ. We observe a crossover from the high-temperature value $S_{imp} = \ln 2$ to the low-temperature value $S_{imp} = 0$ at a crossover scale T^*, which is same as the one introduced in Section 5.2.2. The crossover scale decreases with decreasing Δ in agreement with Eq. (5.14). Note the similarity, which is simply due to the relation between $S_{imp}(T)$ and the flow of the many-particle levels.

As briefly mentioned in Section 5.2.1, the vicinity to the localized fixed point for early iterations, which results in the high-temperature value $S_{imp}(T) \approx \ln 2$, does not imply localization. The value of $S_{imp}(T)$ for high temperatures is due to the fact that for temperatures $T \gg \Delta$ both states of the two-state system contribute equally to the thermodynamics. Note also the similarity to $S_{imp}(T)$ in the Kondo model: there the high-temperature phase is that of a local moment with both spin $\uparrow$ and $\downarrow$ configurations contributing to the entropy (a temperature dependence of $S_{imp}(T)$ as Fig. B.1 might therefore appear more natural in the Kondo model but, of course, it is also valid here).

The scaling behavior of S_{imp} for fixed $\alpha = 1/3$ and various Δ is obvious and is shown in Fig. B.2-(a) together with the scaling curves for $\alpha = 1/5, 1/4$, and

1/2. The agreement with the exact results from the Bethe ansatz calculations in Ref. (Costi and Zarand 1999) is very good [see Fig. 7-(a) in Ref. (Costi 1999)], in particular for the α dependence of the scaling curves.

The temperature dependence of the specific heat, $C_{imp}(T)$, is calculated via $C_{imp}(T)/T = \partial S_{imp}(T)/\partial T$. Here we cannot avoid the discrete differentiation of $S_{imp}(T)$. The scaling of $S_{imp(T)}$ implies a scaling of $C_{imp}(T)/T$ as shown in Fig.B.2-(b). This figure is also very similar to previous calculations [see Fig. 2 in Ref. (Costi 1998) from the NRG via mapping to the anisotropic Kondo model and Fig. 7-(b) in Ref. (Costi and Zarand 1999) using the Bethe Ansatz], and we find the same characteristic features here: a linear specific heat $\propto T$ for low temperatures, a peak in C/T at $T \approx T^*$ for small dissipation $\alpha < 0.3$ in contrast to the monotonous decrease of C/T for large dissipation $\alpha > 0.3$, and a characteristic crossing point of all the C/T scaling curves.

Similar to the NRG calculations in Ref. (Costi 1998), the thermodynamic quantities can only be calculated on a discrete mesh of temperatures given by Eq. (B.5). This strongly limits the resolution of the peak in C/T for $\alpha < 0.3$, in contrast to the Bethe Ansatz calculations of Ref. (Costi and Zarand 1999).

C. BEC OF AN IDEAL BOSONIC GAS WITH A ZERO CHEMICAL POTENTIAL

In usual contexts, theoretical description of BEC in a non-interacting bosonic gas is taken account on canonical systems, where the total number of particles N is fixed and the chemical potential μ is determined as a function of N and temperature T using a relation below:

$$N = \sum_i \frac{1}{e^{\beta(\varepsilon_i - \mu)} - 1}. \tag{C.1}$$

The critical temperature T_c, below which BEC occurs, is defined to satisfy condition:

$$\mu(T_c, N) = 0, \tag{C.2}$$

so that, for $T \leq T_c$,

$$\frac{n(\varepsilon_i = 0)}{n(\varepsilon_i > 0)} \to \infty \tag{C.3}$$

with $n(\varepsilon_i) = 1/\{e^{\beta(\varepsilon_i - \mu)} - 1\}$.

In NRG, a non-interacting bosonic bath (gas) is considered as a grand canonical system where the chemical potential μ is zero and the total number of particles N is infinite. In such a case, we cannot use a chemical potential as a criterion of BEC because it is fixed to zero always. Instead, the ratio of the mean occupation in Eq. (C.3) is directly used to distinguish BEC phase from the others.

Let us assume that a set of single particle states,

$$S_{bec} \equiv \{\varepsilon_i | i = 0, 1, ..., m-1\}, \tag{C.4}$$

is used to construct a BEC (many-particles) state. In general, m can be any finite number. Now BEC for a grand canonical system with $\mu = 0$ is defined as[1]:

$$\frac{n(\varepsilon_i \in S_{bec})}{n(\varepsilon_i \notin S_{bec})} \to \infty. \tag{C.5}$$

At $T = 0$, it is obvious that the ground state has all existing particles at the level of $\varepsilon = 0$ and the other states with $\varepsilon > 0$ are empty. Thus Eq. (C.5) is satisfied with a subset S_{bec}:

$$S_{bec} = \{\varepsilon_0 | \varepsilon_0 = 0\}. \tag{C.6}$$

[1] See (Leggett 2001)

For a finite temperature $T \neq 0$, the mean occupation n_i for a single particle level ε_i diverges as ε_i approaches zero:

$$\lim_{\varepsilon_i \to 0} n(\varepsilon_i) = \lim_{\varepsilon_i \to 0} \frac{1}{e^{\beta(\varepsilon_i - \mu)} - 1} = \infty \tag{C.7}$$

with $\mu = 0$. Now we prove that, at $T > 0$, there are infinitely many ε_i that satisfy Eq. (C.7). (In other words, m, the dimension of S_{bec}, is infinite.) Let us take an arbitrary large integer N. For an arbitrarily large number N, there exists a small energy ε^* such that

$$\varepsilon^* = k_B T \ln(1 + 1/N), \tag{C.8}$$

and any single particle state ε_i smaller than ε^* has a mean occupation number $n(\varepsilon_i)$ larger than N; i.e.,

$$n(\varepsilon_i) > n(\varepsilon^*) = \frac{1}{e^{\ln(1+1/N)}} - 1 = N, \tag{C.9}$$

for $0 < \varepsilon_i < \varepsilon^*$. The fact that the dimension of S_{bec}, m, is infinite violates the definition of BEC in Eq. (C.5). Thus BEC of a non-interacting bosonic system is restricted within zero temperature.

D. DETAILS ABOUT THE ITERATIVE DIAGONALIZATION IN THE BOSONIC SINGLE-IMPURITY ANDERSON MODEL

Let $|Q,r\rangle_N$ denote the eigenstates of H_N that have charge Q. One now constructs from each of the states $|Q,r\rangle_N$ the following states:

$$\begin{aligned} |Q,r;0\rangle &= |Q,r\rangle_N \\ |Q,r;1\rangle &= b_N^\dagger |Q,r\rangle_N \\ |Q,r;2\rangle &= \frac{(b_N^\dagger)^2}{\sqrt{2!}}|Q,r\rangle_N \\ |Q,r;3\rangle &= \frac{(b_N^\dagger)^3}{\sqrt{3!}}|Q,r\rangle_N \\ &\ldots \end{aligned} \tag{D.1}$$

Using these states, we can form the following basis states of H_{N+1} that are also eigenstates of $Q_{N+1} = Q_N + b_N^\dagger b_N$.

$$\begin{aligned} |Q,r,0\rangle &= |0,r;Q\rangle \\ |Q,r,1\rangle &= |1,r;Q-1\rangle \\ |Q,r,2\rangle &= |2,r;Q-2\rangle \\ &\ldots \\ |Q,r,Q\rangle &= |Q,r;0\rangle. \end{aligned} \tag{D.2}$$

Now we write the recursive Hamiltonian in the form

$$H_{N+1} = \Lambda H_N + H_{NI}, \tag{D.3}$$

with

$$H_{NI} = \Lambda^{N+1}\varepsilon_{N+1} b_{N+1}^\dagger b_{N+1} + \Lambda^{N+1} t_N (b_N^\dagger b_{N+1} + b_{N+1}^\dagger b_N). \tag{D.4}$$

The states in Eq. (D.2) are eigenstates of H_N.

$$\begin{aligned} H_N|Q,r,0\rangle &= E_N(0,r)|Q,r,0\rangle \\ H_N|Q,r,1\rangle &= E_N(1,r)|Q,r,1\rangle \\ H_N|Q,r,2\rangle &= E_N(2,r)|Q,r,2\rangle \\ &\vdots \\ H_N|Q,r,Q\rangle &= E_N(Q,r)|Q,r,Q\rangle. \end{aligned} \tag{D.5}$$

Now we obtain the matrix elements of H_{NI} between the states in Eq. (D.2). It is straightforward to demonstrate that the only non-vanishing matrix elements of H_{NI} are given by

$$\begin{aligned} \langle Q,r',m|H_{NI}|Q,r,m\rangle &= \varepsilon_N(Q-m)\ \delta_{r'r} \\ \langle Q,r',m+1|H_{NI}|Q,r,m\rangle &= t_N\sqrt{Q-m}\ {}_N\langle m+1,r'||b_N^\dagger||m,r\rangle_N \\ \langle Q,r',m|H_{NI}|Q,r,m+1\rangle &= t_N\sqrt{Q-m}\ {}_N\langle m,r'||b_N^\dagger||m+1,r\rangle_N, \end{aligned} \tag{D.6}$$

where $\langle||b_N^{(\dagger)}||\rangle$ are the invariant matrix elements.

In obtaining Eq. (D.6), we have made use of the following results, which follows from Eq (D.2) and Eq. (D.2):

$$\langle Q+1,r,m||b_{N+1}^\dagger||Q,r,m\rangle = \sqrt{Q-m+1}. \tag{D.7}$$

From Eq. (D.6) and Eq. (D.6), it is clear that, starting with the knowledge of the energy levels $E_N(Q,r)$ and the matrix elements $\langle m+1,r'||b_{N-1}^\dagger||m,r\rangle$, we can set up the matrix of H_{N+1}.

The actual iteration upon entering the stage $(N+1)$ would proceed as follows. We first start with the lowest allowed value of $Q_{N+1}(=0)$, and then increase it in steps of 1. Within a given Q-subspace, we construct the matrix

$$H(rm;r'm') \equiv \langle Q,r,m|H_{N+1}|Q,r',m'\rangle. \tag{D.8}$$

Diagonalization of this matrix gives a set of eigenstates

$$|Q,\omega\rangle_{N+1} = \sum_{m,r} U_Q(\omega;rm)|Q,r,m\rangle \tag{D.9}$$

where U_Q will be an orthogonal matrix. The diagonalization means no more than the knowledge of $E_{N+1}(Q,\omega)$ and $U_Q(\omega;rm)$. After completing the diagonalization for one Q, we proceed up, increasing Q in steps of 1. In order to go to the next iteration we need to calculate ${}_{N+1}\langle Q+1,\omega'||b_{N+1}^\dagger||Q,\omega\rangle_{N+1}$. Using the results in Eq. (D.7), it is easy to verify that

$${}_{N+1}\langle Q+1,\omega'||b_{N+1}^\dagger||Q,\omega\rangle_{N+1} = \sum_{m<Q}\sum_r U_{Q+1}(\omega';rm)U_Q(\omega;rm)\sqrt{Q-m}. \tag{D.10}$$

BIBLIOGRAPHY

Affleck, I.: 2005, Non-Fermi liquid behavior in Kondo models, *J. Phys. Soc. Japan* **74**, 59.

Anderson, P. W.: 1970, Ableitung eines armen Mannes der Skalierunggesetze für das Kondo problem, *J. Phys. C: Solid State Phys.* **3**, 2439.

Anderson, P. W., Yuval, G. and Hamann, D. R.: 1970, Exact results in the Kondo problem. ii. scaling theory, qualitatively correct solution, and some new results on one-dimensional classical statistical models, *Phys. Rev. B* **1**, 4464.

Andrei, N. and Destri, C.: 1984, Solution for the multichannel Kondo problem, *Phys. Rev. Lett.* **52**, 364.

Bolech, C. J. and Andrei, N.: 2002, Solution of the two-channel Anderson impurity model: Implications for the heavy fermion UBe_{13}., *Phys. Rev. Lett.* **88**, 237206.

Bruder, C. and Schön, R. F. G.: 1993, Superconductor-Mott insulator transition in bose systems with finite-range interactions, *Phys. Rev. B* **47**, 342.

Bulla, R.: 1999, Zero temperature metal-insulator transition in the infinite-dimensional Hubbard model, *Phys. Rev. Lett.* **83**, 136.

Bulla, R., Costi, T. A. and Vollhardt, D.: 2001, Finite temperature numerical renormalization group study of the Mott-transition, *Phys. Rev. B* **64**, 045103.

Bulla, R., Glossop, M. T., Logan, D. E. and Pruschke, T.: 2000, The soft-gap Anderson model: comparison of renormalization group and local moment approaches, *J. Phys.: Condens. Matter* **12**, 4899.

Bulla, R. and Hewson, A. C.: 1997, Numerical renormalization group study of the O(3)-symmetric Anderson model, *Z. Phys. B* **104**, 333.

Bulla, R., Hewson, A. C. and Zhang, G.-M.: 1997, Low energy fixed points of the sigma-tau and the O(3) symmetric Anderson models, *Phys. Rev. B* **56**, 11721.

Bulla, R., Lee, H.-J., Tong, N.-H. and Vojta, M.: 2005, Numerical renormalization group for quantum impurities in a bosonic bath, *Phys. Rev. B* **71**, 045122.

Bulla, R., Pruschke, T. and Hewson, A. C.: 1997, Anderson impurity in pseudo-gap fermi systems, *J. Phys.: Condens. Matter* **9**, 10463.

Bulla, R., Tong, N.-H. and Vojta, M.: 2003, Numerical renormalization group for bosonic systems and application to the sub-ohmic spin-boson model, *Phys. Rev. Lett.* **91**, 170601.

Bulla, R. and Vojta, M.: 2003, Quantum phase transitions in models of magnetic impurities, *in* A. C. Hewson and V. Zlatić (eds), *Concepts in Electron Correlations*, Kluwer Academic Publishers, Dordrecht, p. 209.

Cardy, J. L.: 1984, Conformal invariance and universality in finite-size scaling, *J. Phys. A* **17**, L345.

Castro Neto, A. H., Novais, E., Borda, L., Zaránd, G. and Affleck, I.: 2003, Quantum magnetic impurities in magnetically ordered systems, *Phys. Rev. Lett.* **91**, 096401.

Chen, K., Jayaprakash, C. and Krishna-Murthy, H. R.: 1992, Spatially dependent zero-frequency response functions and correlation functions in the Kondo model, *Phys. Rev. B* **45**, 5368.

Costi, T. A.: 1998, Scaling and universality in the anisotropic kondo model and the dissipative two-state system, *Phys. Rev. Lett.* **80**, 1038.

Costi, T. A.: 1999, Wilson's numerical renormalization group, *in* I. Peschel, X. Wang, M. Kaulke and K. Hallberg (eds), *Density-Matrix Renormalization - A New Numerical Method in Physics*, Springer, p. 3.

Costi, T. A. and McKenzie, R. H.: 2003, Entanglement between a qubit and the environment in the spin-boson model, *Phys. Rev. A* **68**, 034301.

Costi, T. A. and Zarand, G.: 1999, Thermodynamics of the dissipative two-state system: A Bethe-ansatz study, *Phys. Rev. B* **59**, 12398.

de Haas, W. J., de Bör, J. H. and van den Berg, G. J.: 1934, The electrical resistance of gold, copper and lead at low temperature, *Physica* **1**, 1115.

Freericks, J. K. and Monien, H.: 1993, Phase diagram of the Bose-Hubbard model, *Europhys. Lett.* **26**, 545.

Garg, A., Onuchic, J. N. and Ambegaokar, V.: 1985, Effect of friction on electron transfer in biomolecules, *J. Chem. Phys.* **83**, 4491.

Georges, A., Kotliar, G., Krauth, W. and Rozenberg, M. J.: 1996, Dynamical mean-field theory of strongly correlated fermion systems and the limit of infinite dimensions, *Rev. Mod. Phys.* **68**, 13.

Göhrlich, R. and Weiss, U.: 1998, Specific heat of the dissipative two-state system, *Phys. Rev. B* **38**, 5245.

Gonzalez-Buxton, C. and Ingersent, K.: 1998, Renormalization-group study of Anderson and Kondo impurities in gapless Fermi systems, *Phys. Rev. B* **57**, 14254.

Hewson, A. C.: 1993, *The Kondo Problem to Heavy Fermions*, Cambridge University Press, Cambridge.

Hewson, A. C. and Meyer, D.: 2002, Numerical renormalization group study of the Anderson-Holstein impurity model, *J. Phys.: Condens. Matter* **14**, 427.

Ingersent, K. and Si, Q. M.: 2002, Critical local-moment fluctuations, anomalous exponents, and ω/T scaling in the Kondo problem with a pseudogap, *Phys. Rev. Lett.* **89**, 076403.

Ising, E.: 1925, Beitrag zur theorie des ferromagnetismus, *Z. Phys.* **31**, 253.

Kampf, A. P. and Zimanyi, G. T.: 1993, Superconductor-insulator phase transition in the boson Hubbard model, *Phys. Rev. B* **47**, 279.

Khveshchenko, D. V.: 2004, Quantum impurity models of noisy qubits, *Phys. Rev. B* **69**, 153311.

Kondo, J.: 1964, Resistance minimum in dilute magnetic alloys, *Prog. Theor. Phys.* **32**, 37.

Krauth, W., Caffarel, M. and Bouchaud, J.-P.: 1992, Gutzwiller wave function for a model of strongly interacting bosons, *Phys. Rev. B* **45**, 3137.

Krishna-murthy, H. R., Wilkins, J. W. and Wilson, K. G.: 1980, Renormalization-group approach to the Anderson model of dilute magnetic alloys. I. Static properties for the symmetric case, *Phys. Rev. B* **21**, 1003.

Krishna-murthy, H. R., Wilson, K. G. and Wilkins, J. W.: 1975, Temperature-dependent susceptibility of the symmetric Anderson model: Connection to the Kondo model, *Phys. Rev. Lett.* **35**, 1101.

Leggett, A. J.: 2001, Bose-Einstein condensation in the alkali gases: Some fundamental concepts, *Rev. Mod. Phys.* **73**, 307.

Leggett, A. J., Chakravarty, S., Dorsey, A. T., Fisher, M. P. A., Garg, A. and Zwerger, W.: 1987, Dynamics of the dissipative two-state system, *Rev. Mod. Phys.* **59**, 1.

Logan, D. E. and Glossop, M. T.: 2000, A local moment approach to magnetic impurities in gapless fermi systems, *J. Phys.: Condens. Matter* **12**, 985.

Metzner, W. and Vollhardt, D.: 1989, Correlated lattice fermions in $d = \infty$ dimensions, *Phys. Rev. Lett.* **62**, 324.

Meyer, D., Hewson, A. C. and Bulla, R.: 2002, Gap formation and soft phonon mode in the Holstein model, *Phys. Rev. Lett.* **89**, 196401.

Mühlbacher, L. and Egger, R.: 2003, Crossover from nonaiabatic to adiabatic electron transfer reactions: Multilevel blocking Monte Carlo simulations, *J. Phys. C: Solid State Phys.* **118**, 179.

Oliveira, W. C. and Oliveira, L. N.: 1994, Generalized numerical renormalization-group method to calculate the thermodynamical properties of impurities in metals, *Phys. Rev. B* **49**, 11986.

Recati, A., Fedichev, P. O., Zwerger, W., von Delft, J. and Zoller, P.: 2005, Atomic quantum dots coupled to a reservoir of a superfluid Bose-Einstein condensate, *Phys. Rev. Lett.* **94**, 040404.

Rokhsar, D. S. and Kotliar, B. G.: 1991, Gutzwiller projection for bosons, *Phys. Rev. B* **44**, 10328.

Sachdev, S.: 1997, Theory of finite-temperature crossovers near quantum critical points close to, or above, their upper-critical dimension, *Phys. Rev. B* **55**, 142.

Sachdev, S.: 1999, *Quantum Phase Transitions*, Cambridge University Press, Cambridge.

Sachdev, S., Buragohain, C. and Vojta, M.: 1999, Quantum phase transitions in mott insulators and d-wave superconductors, *Science* **286**, 2479.

Sassetti, M. and Weiss, U.: 1990, Universality in the dissipative two-state system, *Phys. Rev. Lett.* **65**, 2262.

Thorwart, M. and Hänggi, P.: 2002, Decoherence and dissipation during a quantum XOR gate operation, *Phys. Rev. A* **65**, 012309.

Vojta, M.: 2006, Impurity quantum phase transitions, *Phil. Mag.* **86**, 1807.

Vojta, M. and Fritz, L.: 2004, Upper critical dimension in a quantum impurity model: Critical theory of the asymmetric pseudogap Kondo problem, *Phys. Rev. B* **70**, 094502.

Vojta, M. and Kirćan, M.: 2003, Pseudogap Fermi-Bose Kondo model, *Phys. Rev. Lett.* **90**, 157203.

Weiss, U.: 1999, *Quantum dissipative systems, 2nd ed.*, World Scientific, Singapore.

Wilson, K. G.: 1975, The renormalization group: Critical phenomena and the Kondo problem, *Rev. Mod. Phys.* **47**, 773.

Withoff, D. and Fradkin, E.: 1990, Phase transitions in gapless fermi systems with magnetic impurities, *Phys. Rev. Lett.* **64**, 1835.

CURRICULUM VITAE

Name:	Hyun-Jung Lee
Date of birth:	10. October 1977
Place of birth:	Seoul, Korea
Gender:	Female
Nationality:	Republic of Korea

EDUCATION

3/1984 - 2/1990:	Seok-Am Elementary School, Incheon, Korea
3/1990 - 2/1993:	Kum-Ok Gilrs' Middle School, Seoul, Korea
3/1993 - 2/1996:	Sang-Il Girls' High School, Seoul, Korea
3/1996 - 2/2000:	Division of Natural Sciences, Yonsei University, Seoul, Korea, **Bachelor** of Science
3/2000 - 2/2002:	Dept. of Physics, Seoul National University, Seoul, Korea, **Master** of Science, supervised by Prof. Jaejun Yu Title: *Lattice Strain Effects on the Magnetic and Orbital Orderings in the CMR Manganites*
3/2002 - 2/2003:	Employed as a Researching Assistant at Center for Strongly Correlated Materials Research at Seoul National University, Seoul, Korea
4/2003 - 1/2007:	Institut für Physik, Universität Augsburg, Augsburg, Germany, **Ph.D.** studies supervised by Priv.- Doz. Dr. Ralf Bulla Title: *Numerical Renormalization Group Calculations for Impurity Quantum Phase Transitions*

LIST OF PUBLICATIONS

[1] H.-J. Lee and R. Bulla, *Quantum Critical Points in Quantum Impurity Systems*, Physica B **359-361**, 56-58 (2005).

[2] R. Bulla, H.-J. Lee, N.-H. Tong, and M. Vojta, *Numerical Renormalization Group for Quantum Impurities in a Bosonic Bath*, Phys. Rev. B **71**, 045122 (2005).

[3] H.-J. Lee, R. Bulla, and M. Vojta, *Numerical Renormalization Group for Impurity Quantum Phase Transitions: Structure of Critical Fixed Points*, J. Phys.: Condens. Matter. **17** 6935-6957 (2005).

[4] H.-J. Lee and R. Bulla, *Quantum Phase Transitions in the Bosonic Single-Impurity Anderson Model*, cond-mat/0606325